UNIVERSITY OF OKLAHOMA

GRADUATE COLLEGE

LARGE SCALE AND LOCAL INFLUENCES ON THE OCCURRENCE AND MAINTENANCE OF LIQUID BEARING CLOUDS OVER THE GREENLAND ICE SHEET

A THESIS

SUBMITTED TO THE GRADUATE FACULTY

in partial fulfillment of the requirements for the

Degree of

MASTER OF SCIENCE IN METEOROLOGY

By

JONATHAN EDWARDS-OPPERMAN
Norman, Oklahoma
2016

LARGE SCALE AND LOCAL INFLUENCES ON THE OCCURRENCE AND MAINTENANCE OF LIQUID BEARING CLOUDS OVER THE GREENLAND ICE SHEET

A THESIS APPROVED FOR THE
SCHOOL OF METEOROLOGY

BY

Dr. Steven Cavallo, Chair

Dr. David Turner

Dr. Cameron Homeyer

Acknowledgments

There are far too many people who have helped me get to this point for me to be able to thank everyone individually, so before I start I want to give an all encompassing thank you to everyone who has been part of my life and has helped me become who I am today.

First, and most importantly, I would like to thank my advisors, Dr. David Turner and Dr. Steven Cavallo, for their help and encouragement since I arrived at the University of Oklahoma. Prior to working on this project I had limited knowledge of Arctic meteorology but have since both learned a tremendous amount and developed a strong interest in the subject. You have both helped me grow as a student and scientist and I could not be happier to have worked on this incredible project for the past two years. I could not have asked for a better research experience.

To Dr. Cameron Homeyer, thank you for being on my committee and for the excellent cloud physics course.

To the faculty at the Georgia Institute of Technology in the Department of Earth and Atmospheric Sciences, thank you for an excellent undergraduate education. Also a special thanks to Dr. Robert Black for being an excellent professor and advisor for my initial research experience as an undergraduate and to Dr. James Belanger for both your wonderful teaching and willingness to answer any question.

To the faculty at OU not already mentioned, your instruction has helped further my education and I will be forever grateful.

Thank you to all those involved in the Arctic and Antarctic Atmospheric Research Group (AAARG). Both presenting to AAARG and listening to everyone else present on their work have helped me grow as a scientist. There have been many enlightening discussions and helpful suggestions which have come out of these presentations.

To Mallory Row, thank you for being an amazing friend and for all the discussions about our research. I couldn't ask for a better person to have worked with on ICECAPS research.

To everyone working on ICECAPS research not already mentioned, the work done prior to my start at OU and the presentations between us during teleconferences have both helped me learn a great amount and furthered my interest in Arctic meteorology.

To Trisha Palmer, thank you for your wonderful advice and assistance on my first conference poster presentation. It was an amazing opportunity and your help every step of the way made it possible.

To Ryan Lagerquist, thank you for being a good officemate and always being open to discussions about class and research.

Thank you to Jeffrey Thayer, Robert Stillwell, and Connor Flynn for conversations either directly with me or with Dr. David Turner which assisted with our work with the Summit MPL.

To all my fellow SoM graduate students, you are wonderful classmates and working together with you has been a great experience thus far.

To all my family and friends thank you for all your love and support. I couldn't have done it without you.

Table of Contents

Appendix A

List of Tables

List of Figures

Abstract

Arctic liquid bearing clouds (LBCs) have a large impact on the surface radiation and cryospheric mass budgets. Their effect on the surface radiation budget is a combination of two competing processes. First, they can prevent incoming solar radiation from reaching the ground - a function of cloud optical thickness. Second, they absorb terrestrial infrared radiation - a function of the amount of liquid water in the cloud - and emit in the infrared back to the surface thus preventing effective radiative cooling of the surface. Arctic LBCs are frequently observed and can persist for up to several days at time. Their persistence is due to a combination of local processes, such as cloud top radiative cooling and turbulence, and factors relating to the large-scale atmospheric setup, such as moisture advection and large-scale vertical motion. Given their longevity and influence on the Arctic surface, it is of interest to explore the factors that contribute to their occurrence over Summit, Greenland.

The Integrated Characterization of Energy, Clouds, Atmospheric State and Precipitation at Summit (ICECAPS) project has been collecting data at Greenland's Summit Station (elevation 3200 m above sea level) from a suite of remote sensors designed to measure cloud and tropospheric properties since the summer of 2010. Using these data, 326 liquid bearing cloud events lasting at least 6 hours have been identified over the period June 1, 2010-September 30, 2015. LBCs are observed at Summit more frequently during the negative phase of the North Atlantic Oscillation. They also occur more frequently during summer months (JJA) with decreases in occurrence in each following season with a minimum in spring

(MAM). Moisture transport to the top of the Greenland Ice Sheet from both horizontal advection and orographic lift is found to coincide with LBC events. The flow patterns leading to moisture transport to Summit are highly related to the phase of the NAO. During the positive phase of the NAO, low pressure systems track along the southeastern coast of the ice sheet. Wraparound flow from these cyclones leads to flow at Summit originating from the southeast. During the negative phase, strong ridging over the ice sheet leads to southwesterly flow toward Summit.

Microphysical properties of LBCs occurring at Summit exhibit strong seasonal cycles with maxima in liquid water path, ice water path, and precipitation occurring during the summer and minima occurring during the spring. Both liquid water path and precipitable water vapor observed at Summit are weakly related to the phase of the NAO with higher values observed during the negative phase when strong ridging over the ice sheet leads to southwesterly flow toward Summit. Ice water path and precipitation rate are unrelated to the large scale atmospheric setup.

Chapter 1

Introduction

1.1 Motivation

The Arctic is a particularly important region for meteorological study due to its sensitivity to climate change (Serreze and Barry, 2011), connection with mid-latitudes processes (Jung et al., 2014), and the relative lack of previous meteorological research when compared to lower latitudes. The scarcity of observations from the Arctic is a major contributor to this lack of previous research. Research in high latitudes has expanded in relatively recent times beginning with the onset of the satellite era followed by, more recently, field campaigns (e.g. SHEBA) and placement of permanent measurement stations in the Arctic (e.g. the Atmospheric Radiation Measurement (ARM) Climate Research Facility's north slope of Alaska site in Barrow) which have provided much needed observations from this historically data sparse region.

Research into both the local meteorological and the large-scale climatic processes involved in the Arctic provides benefit not only to atmospheric sciences but to other scientific domains as well (Jeffries et al., 2015). For example, both seasonal variability and changing mean climate conditions have a large impact on research into the local marine (Fossheim et al., 2015; Frey et al., 2015) and terrestrial (Epstein et al., 2015; Kovacs et al., 2015) ecosystems of the Arctic.

Improved knowledge of Arctic climate is necessary for research regarding changes in species and ecosystem distributions, especially given the Arctic's response to climate change.

As atmospheric greenhouse gas (GHG) concentrations increase globally, there has been a corresponding increase in globally averaged surface temperatures. However, the Arctic has an enhanced sensitivity to these GHG increases relative to the rest of the globe. This is known as Arctic amplification. Surface temperature anomalies over the past decade show a clear poleward increase in magnitude in the Northern Hemisphere (Figure 1.1). In addition to the direct influence on the Arctic climate (i.e. enhanced surface warming), the effects of Arctic amplification can be realized worldwide. For example, melting of continental ice sheets causes an increase in sea level, which affects coastal regions across the entire globe. The poleward increase in the magnitude of temperature anomalies also decreases the latitudinal temperature gradient which could influence weather in the mid-latitudes via a weakening of the polar jet stream. Initial research on Arctic amplification primarily featured modeling studies (e.g., Robock, 1983) due to the aforementioned lack of observations in the Arctic. The advent of satellites has helped to provide observational confirmation of Arctic amplification (e.g., Boisvert and Stroeve, 2015). Arctic processes need to become better understood in order to predict how the many feedbacks between cloud fraction, cloud phase, land surface, ocean, water vapor, etc. will change and influence Arctic amplification.

The Arctic influence on mid-latitude weather was shown by Jung et al. (2014) where it was shown that extended range global forecast error derives primarily from the Arctic. Because of the implications that Arctic processes have on mid-latitude prediction, there is motivation to better understand Arctic processes through observations in order to improve model representation of those processes.

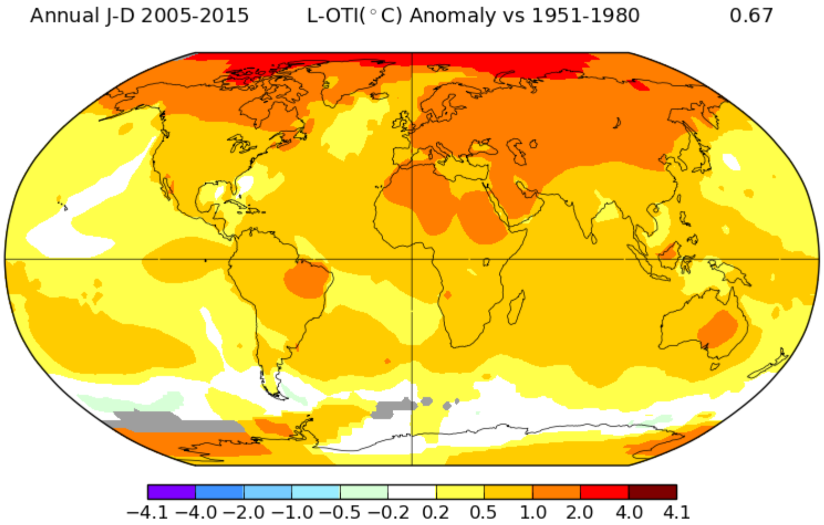

Figure 1.1: Temperature anomalies for the period 2005-2015 (relative to the 1951-1980 climatology). Surface temperature data is from NASA's GISS Surface Temperature Analysis (GISTEMP) and sea surface temperature data is from NOAA's Extended Reconstructed Sea Surface Temperature (ERSST) dataset.

Arctic clouds in particular constitute an important area of research due to their effect on the surface radiative (Shupe and Intrieri, 2004; Curry et al., 1996) and cryospheric mass (Bennartz et al., 2013; Van Tricht et al., 2016) budgets. Clouds are central to many of the feedback processes in the Arctic due to their influence on both the amount of shortwave (SW) and longwave (LW) radiation reaching the surface. Liquid bearing clouds (this includes both liquid only and mixed-phase clouds, which have both liquid and ice in the same volume) have an especially large impact on the Arctic's surface energy balance since liquid is an effective absorber of longwave radiation. The effect of these clouds is magnified due to their longevity and frequency of occurrence across many unique regions of the Arctic (e.g., the north slope of Alaska (Verlinde et al., 2007), the Beaufort Sea (Shupe et al., 2006), Eureka (northern Canada; de Boer et al. (2009)) and central Greenland (Miller et al., 2015)). These clouds consist of thin stratiform layers topped with liquid water and are often associated with ice precipitation. These clouds have been the focus of recent studies due to their occurrence across the Arctic throughout the entire year as well as their long lifetimes. They can persist for several days at a time, which is not theoretically expected (Morrison et al., 2012). This longevity is likely do to the combination of local cloud processes (e.g. radiative cooling and cloud microphysical properties) and characteristics of the large scale atmospheric setup (e.g. moisture advection and large scale vertical motion) outlined by Morrison et al. (2012). The exact nature of the balance between the many processes is still largely unknown. Even the relative importance of the large scale forcing versus local processes is not resolved and may be different depending on which region of the Arctic is considered.

Liquid bearing clouds are especially important over Greenland due to their effect on the melt of the Greenland Ice Sheet (GIS; Bennartz et al. (2013); Van Tricht et al. (2016)). Given this influence it is important to identify what factors can influence the occurrence of these clouds in order to determine how the Greenland surface energy balance and GIS mass balance might change in the future. In addition to the occurrence of these clouds over the GIS, it is of interest to determine what factors contribute to the longer lifetime of some of these clouds.

The following work is conducted in conjunction with the Integrated Characterization of Energy, Clouds, Atmospheric state, and Precipitation at Summit (ICECAPS) project (Shupe et al., 2013), a field campaign beginning in May 2010 providing a suite of meteorological instruments at Summit Station, Greenland designed to obtain measurements of both cloud and tropospheric properties. Summit Station is 3200 meters above sea level, melting of the surface here is very rare; the ice sheet generally remains frozen year round (Bennartz et al., 2013). Strong surface temperature inversions are also common (Miller et al., 2013). These factors create an environment different from other Arctic locations at which liquid bearing clouds have been studied.

1.2 Research Question and Thesis Structure

Given the importance of liquid bearing clouds on the Arctic, and specifically those over Greenland, it is of interest to better understand both why these clouds occur so frequently and why they can persist for so long. This thesis focuses on understanding the relative importance of the large scale atmospheric setup and the local processes to both the occurrence and lifetime of liquid bearing clouds over Summit Station, Greenland. A literature review will be presented in Chapter 2. Datasets and methodology used are discussed in Chapter 3. Specific questions about the large scale environment will be addressed in Chapter 4 including: a) what large scale climate patterns are associated with the occurrence of liquid bearing clouds over Summit Station Greenland?, and b) what specific meteorological conditions occur with these patterns that favor cloud occurrence and/or lifetime? Chapter 5 will characterize the microphysical properties of these clouds and assess the local processes which affect the variability of these properties. Finally conclusions and comparisons to results in the current literature will be addressed in Chapter 6.

Chapter 2

Background

The following sections further expand on the motivation behind studying Arctic meteorology outlined in Chapter 1. This will begin with a broad overview of some important Arctic processes before focusing on the role which clouds, and in particular liquid bearing clouds, play in the Arctic environment. This will be followed by a discussion of the previous points in the context of Greenland in particular.

2.1 Importance of Arctic Meteorology

2.1.1 Arctic Amplification

Arctic amplification is defined as the larger surface temperature change poleward in the Northern Hemisphere in response to a positive change in the Earth's net radiation balance at the surface (Serreze and Barry, 2011). In the context of climate research, this positive change in net radiation is caused by increases in atmospheric greenhouse gas concentrations, which trap longwave radiation emitted by the Earth. Arctic amplification has constituted a large component of polar atmospheric research over the past several decades. However, the hypothesis that polar near surface temperatures have a larger sensitivity (compared with the rest of the planet) to increases in global atmospheric greenhouse gas concentrations has been around for much longer. Arrehnius (1896) predicted that increases in atmospheric carbon would create larger temperature increases poleward from the equator and that the Northern Hemisphere would experience larger temperature increases when compared to the Southern Hemisphere. Arrehnius (1896) obtained this result by latitudinally varying his calculations based on estimates of mean cloud occurrence and, more importantly for his results, surface type. This work essentially identified what is now called the ice albedo feedback (Curry et al., 1996). This feedback occurs when surface warming causes snow and ice to melt, thus decreasing the surface albedo. A decreased surface albedo then allows more radiation to be absorbed by the surface which further exacerbates the initial warming.

Interest about the potential effect of anthropogenic greenhouse gas emissions combined with improvements in computational power led to the study of Arctic amplification using numerical models. Manabe and Stouffer (1980) used a coupled ocean-atmosphere global climate model to study the effect of a quadrupling of atmospheric carbon dioxide. They too found that the largest near-surface temperature response occurs in the Northern Hemisphere high latitudes. In addition, they found significant seasonal dependence of the results, especially in the Arctic, with a maximum warming during the winter and minimum warming during the summer. This seasonal dependence is attributed to changing sea ice coverage. Reduced sea ice areal coverage or a decrease in thickness of sea ice in the summer leads to a greater amount of solar radiation being absorbed at the surface. However, this increase in energy is used to further melt sea ice and to warm the mixed layer of the ocean, not to warm the lower atmosphere. The increased heat content in the ocean then either delays the onset or reduces the thickness of sea ice in early winter leading to a reduction of thermal insulation of the warmer ocean water by sea ice in winter thus allowing heat to transfer from the ocean

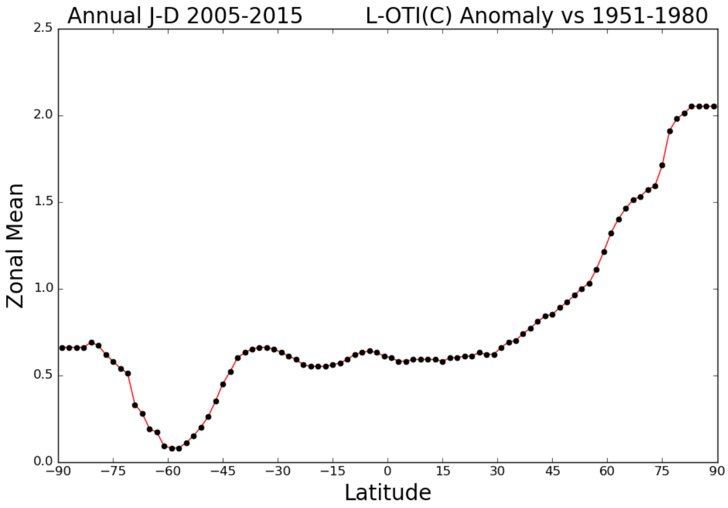

Figure 2.1: Zonally averaged temperature anomalies (°C) for the period 2005-2015 (relative to the 1951-1980 climatology). Data source same as Figure 1.1.

to the lower atmosphere. Similar patterns were found by Robock (1983) using a climate model with updated land surface parameterization schemes of snow and ice based on (then) new satellite observations. In addition, Robock (1983) found the ice albedo feedback to be a dominant driver of enhanced Arctic sensitivity to climate change by comparing simulations where the albedo feedback was manually turned off, thereby keeping snow and ice albedo constant, to simulations where the albedo was allowed to change. With this method, Robock (1983) showed that the ice portion of the snow/ice albedo feedback was dominant. This was likely due to the fact that when snow melts, the underlying surface can be ice (which also has a high albedo), but when ice melts the underlying surface is ocean or ice free land, both of which have a lower albedo. The increase in observations in the high latitudes has led to observational verification of these modeling results; the 2005-2015 average surface temperature anomaly exhibits a strong dependence on latitude in the Northern Hemisphere (Figure 2.1).

However, modeling studies with albedo fixed at a constant value have still reproduced Arctic amplification indicating the presence of other feedbacks (Graversen and Wang, 2009; Hall, 2004). After the early focus on the ice albedo feedback, more recent research has indicated that several other feedback processes are likely important (Curry et al., 1996; Serreze and Barry, 2011). For example, when the atmosphere warms there is an enhancement of evaporation and thus an increase in water vapor content, especially in the lower atmosphere, which leads to a positive feedback on temperature due to enhanced trapping of longwave radiation (Curry et al., 1996; Graversen and Wang, 2009). In the Arctic, this feedback is highly related to sea ice cover (Serreze and Barry, 2011). If sea ice coverage decreases, more ocean area is exposed thereby changing the vertical fluxes between the ocean and atmosphere. Curry et al. (1995) found that this feedback was positive over the Arctic Ocean in all months but was most important during the autumn and spring. The improvement of satellite observations has led to the observational verification of many of these processes. Using the spaceborne Atmospheric Infrared Sounder (AIRS), Boisvert et al. (2015) found an increase in the amount of evaporation occurring in the Arctic. Similarly, Boisvert and Stroeve (2015) found that the Arctic has experienced increases in both tropospheric moisture content and temperature over the past decade at least in part driven by decreases in sea ice cover during the summer, which allowed for more evaporation. This increase in water vapor content of the atmosphere contributes to a stronger greenhouse effect if it remains in the Arctic and in the gas phase.

Another important feedback process which contributes to Arctic amplification is the temperature feedback (Manabe and Wetherald, 1975; Pithan and Mauritsen, 2014). This term collectively describes two processes which lead to a greater increase in energy radiated back out of the tropics relative to the Arctic. First, if there is a uniform initial warming on a warm and cool surface; the warm surface will experience a greater increase in emitted radiation due to the T^4 dependence of emission. Second, Manabe and Wetherald (1975) found that a non-uniform vertical warming structure that differs in the tropics and Arctic also leads to greater latitudinal differences in near surface warming. This is due to the relatively shallow layer in which warming in the Arctic is located (Manabe and Wetherald, 1975). The common occurrence of temperature inversions in the Arctic inhibits the effective vertical mixing of surface temperature anomalies (Bintanja et al., 2012). Pithan and Mauritsen (2014) noted the importance of this feedback in a modeling sensitivity study aimed at identifying the most important feedback processes in the Arctic. While the ice albedo feedback caused the greatest magnitude of warming in the Arctic, the temperature feedback was found to increase the latitudinal difference in warming by a greater amount.

2.1.2 Global and Interdisciplinary Connections

The Arctic is an important region for meteorological study due to its potential impact on the rest of the globe. Warming of the troposphere associated with climate change has led to increased melting of Arctic ice sheets, thus leading to an increase in sea level (Shepherd et al., 2012). Of particular importance is the GIS due to its large volume. Satellite data shows that the GIS has been losing mass at an accelerating rate since the early 1990s (Shepherd et al., 2012). Figure 2.2 shows the total cumulative change in the ice mass of the GIS and the corresponding increase in sea level. This mass loss has increased in spatial extent in recent times with portions of the northern GIS, which were in mass balance during the 1990s, now experiencing mass loss at an accelerating rate (Mouginot et al., 2015).

The atmospheric processes in the Arctic also have impacts on weather prediction in the midlatitudes (Jung et al., 2014). Figure 2.3 shows the relative impact of relaxing a numerical weather prediction model toward reanalysis over different regions of the globe for medium range weather prediction in the midlatitudes. Jung

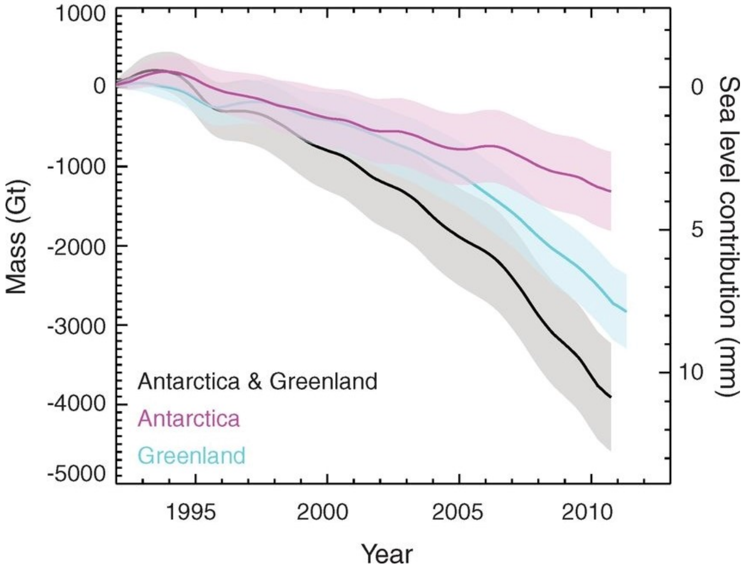

Figure 2.2: Cumulative changes in the mass (left axis) and contribution to sea level change (right axis) of the Greenland Ice Sheet, Antarctic Ice Sheet, and the sum of the two using a combination of observations and numerical simulations. From Shepherd et al. (2012), Figure 5.

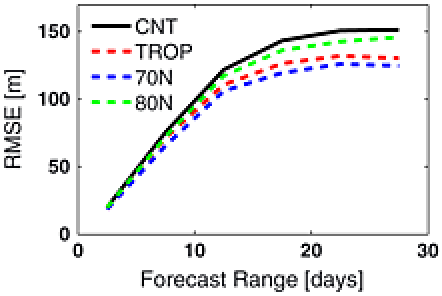

Figure 2.3: Root-mean-square error for forecasts of 500hPa geopotential height during winter for the Northern Hemisphere midlatitudes. Results are for a control forecast (black), relaxation of the model toward reanalysis north of 70°N (blue), north of 80°N (green), and the tropics within 20°N and S (red). From Jung et al. (2014), Figure 2.

et al. (2014) showed that the Arctic (defined as poleward of 70°N) had more of an influence on midlatitude prediction than the tropics for all forecasts with lead times beyond one week. Given that Arctic processes contribute significantly to midlatitude weather prediction errors, a more complete understanding of Arctic meteorology is needed. In order to reduce model error deriving from the Arctic, modeling of high-latitude processes must be improved. Model representation of Arctic clouds is a particular challenge due to the difficulties associated with correctly modeling cloud microphysics and the relative lack of observations of Arctic clouds relative to the rest of the globe (Curry et al., 1996; Klein et al., 2009; Fridlind et al., 2012).

Understanding the variability and change of the Arctic climate is key for other scientific disciplines as well. Epstein et al. (2015) note that the expected and previously observed trend of increasing vegetation biomass in Northern Hemisphere tundra has reversed. This could be due to a variety of factors including differing regional sensitivities to climate change in the Arctic. The uncertainties in both biome response and the exact nature of Arctic climate variability and change make accurate predictions of changing ecosystem distributions difficult. Changes in oceanic ecosystems have also been noted (Frey et al., 2015). The population distributions of certain marine species have been shifting, mostly poleward, as a result of warming (Fossheim et al., 2015) while other species have been losing habitat (Kovacs et al., 2015). It should be noted that all of the research cited here has been diagnostic in nature. For more predictive research to be done, better knowledge of Arctic climate is necessary.

2.2 Arctic Cloud Occurrence and Properties

Clouds are an important component of the Arctic climate system due to their high frequency of occurrence and impact on the surface radiation and cryospheric mass budgets (Curry et al., 1996; Warren et al., 1988; Curry and Ebert, 1992). Arctic clouds are observed to occur for a significant fraction of time across all seasons (Figure 2.4). It should be noted that early satellite climatologies (for example the climatology denoted with the solid line in Figure 2.4) tend to underestimate cloud occurrence since low level clouds are common in the Arctic and satellite remote sensors have trouble differentiating them from the ground due to similar cloud top and surface temperatures. The common occurrence of Arctic clouds is one reason why they have such a large effect on the surface radiation budget. Clouds can trap longwave radiation emitted from the surface by absorbing and re-emitting that radiation back to the surface. The emission is strongly dependent on the amount of liquid in the cloud (Curry and Herman, 1985b). Curry et al. (1997) found that longwave emission from clouds was likely responsible for rapid surface temperature changes over the Beaufort Sea in a case study. In addition, the optical depth of clouds affects how much solar (shortwave) radiation reaches the surface. Cloud effects on surface radiation are further amplified in the Arctic because of the 24 hours of solar radiation received daily during Northern Hemisphere summer and due to the high albedo of the land surfaces (much of the solar radiation which impinges on snow and ice is reflected).

Of particular importance are low-level clouds containing liquid due to their frequency of occurrence and, as previously stated, their impact on the surface radiation budget; liquid is a very effective emitter of IR radiation. However, these clouds are not theoretically expected in the Arctic environment (Wexler, 1936) due to the strong radiative cooling of the surface which is expected to lead to large-scale anticylonic circulation (Wexler, 1937). Any condensation occurring due to the aforementioned cooling is theoretically expected to rapidly fall out to the surface due to the absence of upward motion. Curry (1983) extended this research noting that the earlier assumption that all condensate immediately falls out is

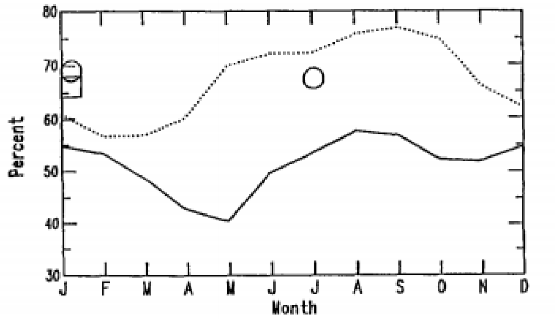

Figure 2.4: Mean cycle of cloud occurrence over 60-90°N. Solid line is from satellite data and dashed line is from surface observations. Open circles represent improved estimates from a (then) new satellite retrieval and the open square indicates improved surface based estimates for wintertime observations. From Curry et al. (1996), Figure 1.

unrealistic. In one experiment, Curry (1983) assumes the condensate is entirely in the liquid phase and only gradually falls out. Given the effectiveness of IR emission from liquid water, this led to a reduction in the surface cooling. The location of maximum cooling was at the top of the condensed layer. However, it was noted that the thick liquid fog which was produced in this experiment was not found in any observations and likely unrealistic. In a another experiment, Curry (1983) assumed condensation of an upper level liquid water layer and lower level composed of ice crystals. This experiment allowed the liquid layer to persist for several days. Curry (1983) notes that a theoretical mechanism for the maintenance of liquid clouds under anticyclonic conditions exists if large scale moisture advection occurs at upper levels allowing replenishment of moisture in these clouds from above.

Following the work by Curry (1983), the occurrence and maintenance of liquid bearing clouds has been documented at multiple Arctic locations. Curry and Ebert (1992) found that low level clouds are particularly common in the Arctic, especially during summer, while Shupe and Intrieri (2004) found that radiative forcing from relatively warm (>-15°C) clouds containing liquid was particularly large. In the

Arctic, these clouds generally consist of one or more thin layers of supercooled liquid at cloud top with ice below (Morrison et al., 2012). These clouds often produce ice phase precipitation as well. Mixed phase clouds over the Arctic Ocean have been found to induce a net surface warming for most of the year with a small period of surface cooling during midsummer when the amount of incoming solar radiation is at a peak and the albedo effect is dominant (Curry and Ebert, 1992; Shupe and Intrieri, 2004). Conversely, ice clouds and diamond dust (clear sky ice precipitation) were found to be much less important for the surface energy budget (Shupe and Intrieri, 2004; Intrieri and Shupe, 2004).

LBCs have been found in a variety of locations in the Arctic. de Boer et al. (2009) found liquid water in clouds during all seasons in Eureka, Nunavut, Canada and Barrow, Alaska with maximum in occurrence during the fall. Tjernström et al. (2012) observed clouds during 90 percent of the Arctic Summer Cloud Ocean Study (ASCOS). This included observations of cloud cover in the boundary layer for 80 percent of the field study with most observed clouds containing liquid water. Several field experiments (e.g. the Beaufort and Arctic Storms Experiment (BASE) and Surface Heat Budget of the Arctic Ocean (SHEBA)) have observed liquid bearing clouds over the Beaufort Sea (Shupe et al., 2006; Jiang et al., 2000). During SHEBA, mixed phase clouds were observed for 41 percent of the annual cycle (Shupe et al., 2006). Liquid was found to occur in clouds about 40 percent of the time at Barrow based on a microphysical retrieval, although during spring the occurrence of liquid was much less frequent (Shupe et al., 2015). Qiu et al. (2015) also obtained similar results in their analysis at Barrow. More recently, studies have shown these clouds over the GIS as well (Miller et al., 2015; Bennartz et al., 2013) (see Section 2.4.4 below). Figure 2.5 shows a climatology of Arctic clouds observed at Barrow, SHEBA, and Eureka.

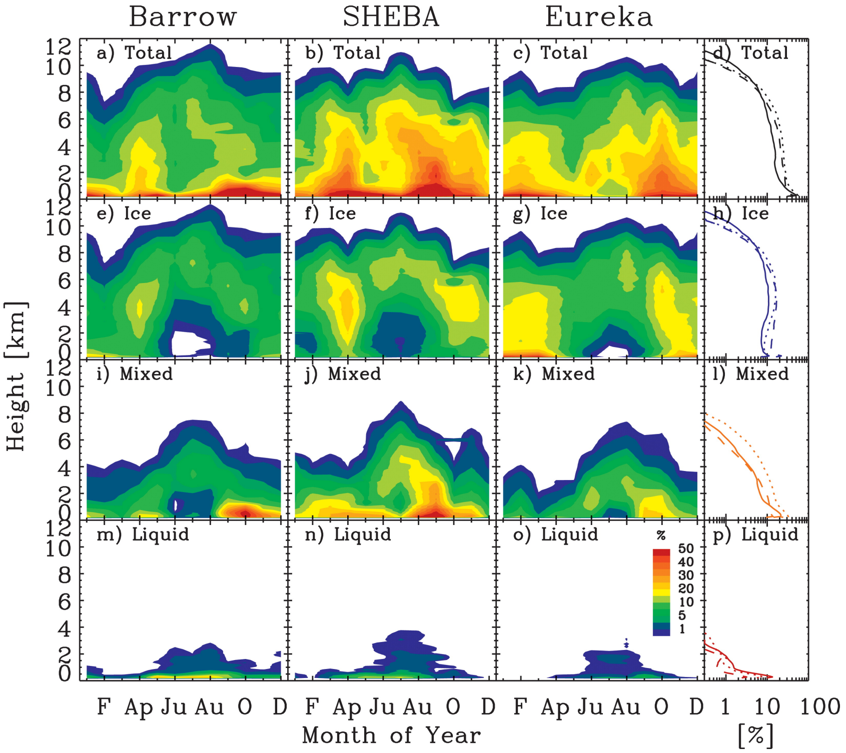

Figure 2.5: Climatology of cloud occurrence as a function of month and height for all cloud types (a-c), ice clouds (e-g), mixed phase clouds (i-k), and liquid clouds (m-o) at Barrow, Alaska (first column), SHEBA (second column), and Eureka, Canada (third column). The fourth column shows the annual average cloud cover for Barrow (solid line), SHEBA (dotted line), and Eureka (dashed line). From Shupe (2011), Figure 3.

Arctic mixed phase clouds are consistently observed at relatively low altitudes where the temperature is warm enough to allow for supercooled liquid water (supercooled liquid water can occur in temperatures as low as approximately -40°C). The warmest temperatures are often found just above the surface in the Arctic due to the presence of surface based temperature inversions created by strong radiative cooling of the surface (Wexler, 1936). de Boer et al. (2009) found that the majority of stratiform clouds over Barrow and Eureka occurred within about 2 km of the surface (Shupe et al. (2015) found similar results for Barrow). During SHEBA, the average cloud base height was just under 1 km (Shupe et al., 2006).

Stramler et al. (2011) found two preferred atmospheric states during SHEBA (Figure 2.6). One was defined as radiatively clear which meant there was little or no difference in between the observed net radiative state and the radiative state which would be expected in clear sky conditions (i.e. net longwave cooling of the surface was observed and an inversion is developed/strengthened). However, it should be noted that clouds were often still observed in the radiatively clear state, but these clouds were optically thin and likely entirely composed of ice. The second state found by Stramler et al. (2011) occurred when the net longwave radiative flux at the surface was approximately 0 $W\ m^{-2}$. Clouds were observed 100% of the time during this state. These clouds occurred at or near the top of the temperature inversion. Transitions between the two states were found to be abrupt and driven by synoptic circulation patterns; specifically, the second, cloudy state corresponded to advection over the SHEBA location related to cyclonic weather systems. These systems allow moisture to intrude into the Arctic from lower latitudes (Woods et al., 2013). Pithan et al. (2014) found that this cloudy state was initiated by cooling of a warm, moist air mass advected into the Arctic from the midlatitudes. The clouds associated with this state were found to be either liquid only or mixed-phased (Pithan et al., 2014).

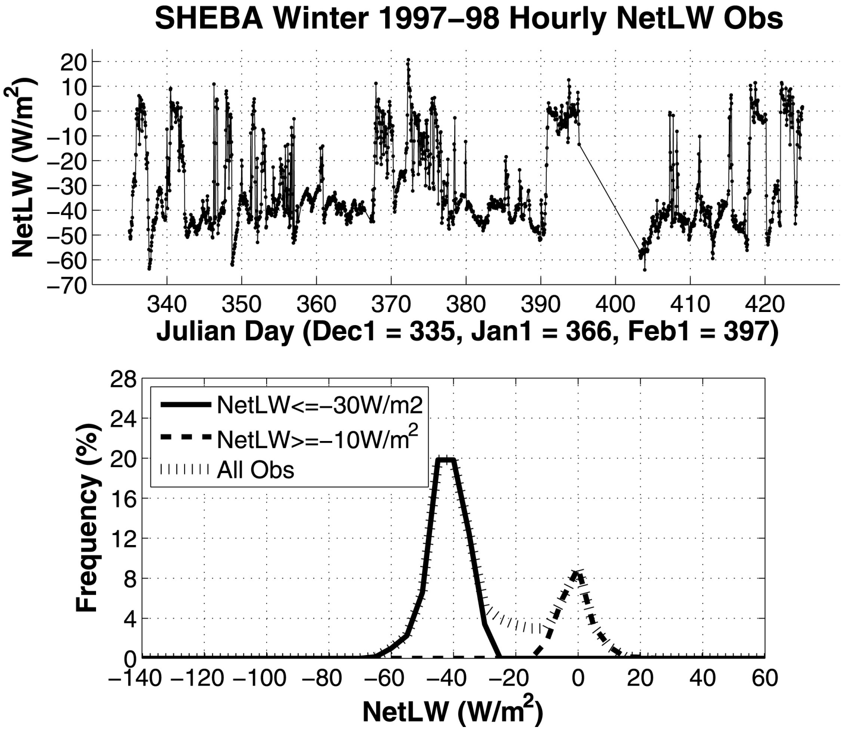

Figure 2.6: Times series of net longwave radiation observations from SHEBA (top) and histograms (bottom) of the same observations (dotted lines) along with highlighted modes for the two predominate states (dashed and solid lines) From Stramler et al. (2011), Figure 2.

One particularly interesting macrophysical aspect of Arctic mixed phase clouds is their long lifetime; they can persist for days at a time, which is theoretically unexpected (Morrison et al., 2012). In theory, if an air parcel containing both ice crystals and liquid drops is lifted (and therefore cooled) in an environment which is supersaturated with respect to both ice and water, then particles of both phases should experience growth by vapor diffusion. However, since environmental supersaturations with respect to ice are greater than with respect to water, after a period of time the supersaturation with respect to water will decrease to zero as water vapor content of the atmosphere decreases to the point where liquid drops will no longer grow; the ice particles will continue to grow by diffusion. This further decreases the environmental supersaturations to where the ice particles will grow while the liquid drops evaporate since the relative humidity with respect to water will drop below 100 percent. This is known as the Wegener-Bergeron-Findeisen (WBF) process. Despite this, Arctic mixed phase clouds have been observed to persist in many locations. For example, during SHEBA mixed phase clouds persisted for an average of about 12 hours but the longest lasted for nearly six and a half days, or 10 days if breaks of a couple hours were allowed in the analysis (Shupe et al., 2006).

There has been quite a large spread in microphysical observations of mixed phase clouds. For example, Curry and Herman (1985b) note that observations of liquid water path (LWP) are often less than 20 $g\ m^{-2}$ in Arctic stratus clouds. However values of over 100 $g\ m^{-2}$ have been observed during field campaigns (Shupe et al., 2006; Curry and Ebert, 1992). de Boer et al. (2009) found values as high as 310 $g\ m^{-2}$ during the Mixed-Phase Arctic Cloud Experiment (MPACE) using observations from Barrow and Eureka. In fact, the average value of LWP during MPACE (167 $g\ m^{-2}$) was nearly the same as the maximum value of LWP found during SHEBA (180 $g\ m^{-2}$) (Shupe et al., 2006). This spread is likely due to a combination of the short period of time many of the field experiments cover (often less than a year) and the varying local effects of different locations (e.g. topography and whether the clouds were observed over ice-covered ocean, open ocean, or land). To-date, there are currently few inter-comparisons between different Arctic observing sites.

2.3 Local and Large Scale Influences on Arctic Mixed-phase Clouds

One of the biggest questions in relation to mixed phase cloud occurrence is the relative importance of local processes, such as moisture entrainment and turbulence driven by cloud top radiative cooling, and large scale processes, such as moisture advection and large scale vertical motion (Morrison et al., 2012). Figure 2.7 shows a conceptual model of some of these processes. Focusing first on the large scale, previous studies indicate there is a broad range of results based on location and season. For example, de Boer et al. (2009) found that in Eureka the predominate wind direction at cloud level when mixed phase clouds were present varied significantly with season and was not as strong as the relationship between wind direction and cloud occurrence found during their one season of anaylsis at Barrow. Verlinde et al. (2007) found a similar result at Barrow with the large-scale setup and prevailing atmospheric flow controlling cloud conditions. Curry and Herman (1985a) found that large scale advection of heat and moisture related to synoptic patterns influenced variations in cloudiness over the Beaufort Sea in a case study although Curry et al. (1988) found a variety of synoptic states during which stratus clouds were observed in the boundary layer over the Beaufort Sea. There is also strong seasonality noted in most of the literature. Mixed-phase clouds over the Beaufort Sea were found to have a maximum occurrence in September (70

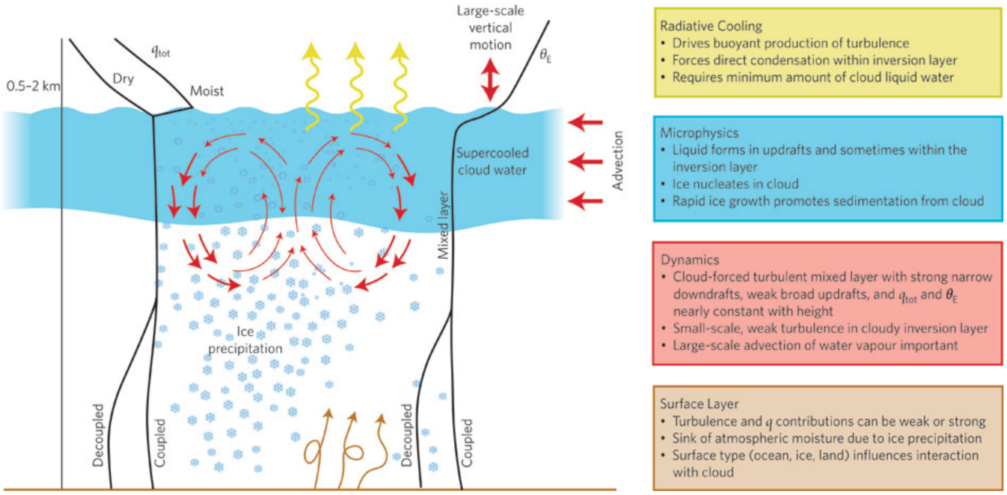

Radiative Cooling
- Drives buoyant production of turbulence
- Forces direct condensation within inversion layer
- Requires minimum amount of cloud liquid water

Microphysics
- Liquid forms in updrafts and sometimes within the inversion layer
- Ice nucleates in cloud
- Rapid ice growth promotes sedimentation from cloud

Dynamics
- Cloud-forced turbulent mixed layer with strong narrow downdrafts, weak broad updrafts, and q_{tot} and θ_E nearly constant with height
- Small-scale, weak turbulence in cloudy inversion layer
- Large-scale advection of water vapour important

Surface Layer
- Turbulence and q contributions can be weak or strong
- Sink of atmospheric moisture due to ice precipitation
- Surface type (ocean, ice, land) influences interaction with cloud

Figure 2.7: Conceptual model of processes important for mixed-phase cloud persistence. From Morrison et al. (2012), Figure 2.

percent) and a minimum in December (10 percent) (Shupe et al., 2006). Qiu et al. (2015) found strong seasonality in mixed phase cloud occurrence at Barrow with a minimum from late winter through spring (especially in March) and maximum in October. Earlier studies focused only on total cloud cover generally found similar results, in that low clouds were highly seasonal while mid-level and upper level clouds were not (Curry et al., 1996; Curry and Ebert, 1992).

There are a multitude of local processes which can help to maintain mixed-phase clouds (Morrison et al., 2012). Cloud top longwave emission by liquid causes a significant amount of cooling which has been shown to be a necessary component of cloud maintenance (e.g. Solomon et al., 2011). This cooling at the cloud top creates local instability and drives turbulence within the cloud which allows for additional condensation thus creating a positive feedback. Korolev (2007) noted that vertical velocities associated with turbulent motions create enough condensation so that both liquid and ice can grow together. Turbulence generated by cloud top radiative cooling also allows entrainment of air into the cloud (Curry, 1986). Solomon et al. (2011) found that moisture inversions, which are frequent in the Arctic (e.g. Curry et al., 1988), supply moisture to the cloud via this entrainment process. However, this moisture source above the cloud does not appear to be a necessary component of the system. Solomon et al. (2014) showed in model simulations that if the above cloud moisture source is cut off but there is a moisture source at the surface, turbulence acted to draw moisture from the surface into the cloud. As long as one of the moisture sources was intact, the cloud continued to persist. Qiu et al. (2015) found that specific humidity inversion intensities were related to the occurrence of mixed phase clouds in all seasons except summer. Furthermore, the strength of the temperature inversion did not appear to have a relationship with the occurrence of mixed phase clouds.

Another potential reason for maintenance of liquid layers in Arctic clouds could be the lack of ice nuclei (IN) (Morrison et al., 2012). An environment with a very small number of IN could dampen the effects of the WBF process since there would be less ice particles experiencing growth. Jiang et al. (2000) found that decreasing the amount of IN from estimated mid-latitude values allowed for a more accurate simulation of a mixed phase cloud. Fridlind et al. (2012) showed there is a significant model sensitivity to assumed ice crystal properties and Xie et al. (2013) found that the Arctic was the most sensitive region of the globe to changes in ice nuclei parameterizations.

2.4 The Greenland Ice Sheet

2.4.1 Recent Observations

Consistent, relatively long term in-situ meteorological observations of the GIS began in the 1990s and initially consisted of data collected by automatic weather stations (e.g. Shuman et al., 2001; Steffen and Box, 2001; Box and Steffen, 2001). Variability in climate conditions across the ice sheet are shown to be primarily

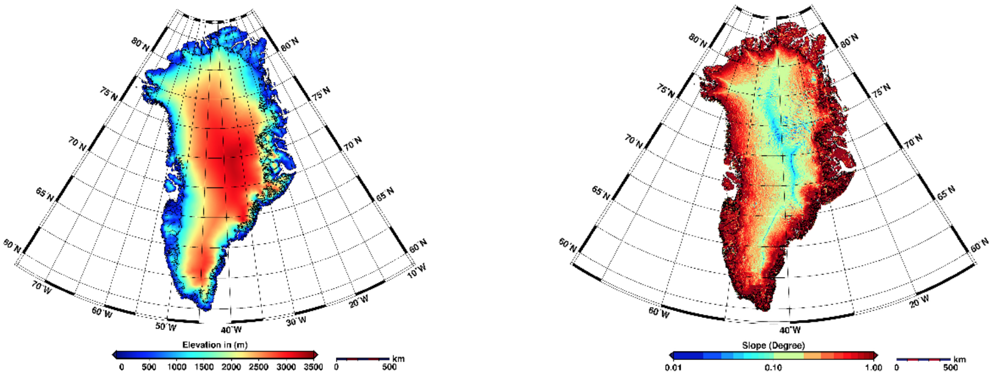

(a) (b)

Figure 2.8: Greenland (a) topography and (b) surface slope estimated from CryoSat-2. From Helm et al. (2014), Figures 7-8.

due to latitude (Steffen and Box, 2001) and topography (Steffen and Box, 2001; Ohmura and Reeh, 1991). Greenland's topography consists of a steeply sloped border followed by a slower rise in elevation over the interior of the ice sheet (Figure 2.8). Ohmura and Reeh (1991) found that spatial variability in precipitation patterns over the GIS are related to the interaction between the climatological wind pattern and the topography of the subcontinent. The analysis of mean wind patterns and precipitation by Ohmura and Reeh (1991) also indicated that Summit, Greenland must be regularly influenced by airmasses originating from the Atlantic Ocean. Observations from automatic weather stations indicate prevailing wind patterns ranging from southwesterly to southeasterly at Summit lending evidence to this theory (Steffen and Box, 2001).

Recent research on the GIS has focused on the summer melt of the ice sheet (e.g. Doyle et al., 2015; McLeod and Mote, 2015). This research has linked several different atmospheric phenomena to ice loss including large scale atmospheric circulation patterns (see Section 2.4.2, below), rainfall along the periphery of the ice sheet (Doyle et al., 2015), advection of warm, moist air over the ice sheet (Neff et al., 2014), and clouds (see Section 2.4.4, below). This research has intensified recently due to the observed trend of increasing melt extent during the summer (Fettweis et al., 2013; Mouginot et al., 2015) and the understanding that this increase is playing a significant role in sea level rise (Jacob et al., 2012; Shepherd et al., 2012). In addition to this consistent increasing trend in recent times, the GIS experienced record melt in the summer of 2012 (Tedesco et al., 2013) which has been linked to low level liquid clouds (Bennartz et al., 2013) and advection of warm, moist air over the ice sheet (Neff et al., 2014; Bennartz et al., 2013).

2.4.2 Large Scale Atmospheric Patterns

The North Atlanic Oscillation (NAO) describes the daily variability of 500 hPa geopotential height anomalies over the North Atlantic (Barnston and Livezey, 1987; Hurrell et al., 2001). The NAO pattern consists of two phases: a) the positive phase where the pattern of relatively high heights near the Azores and lower heights near Greenland and Iceland is enhanced (i.e. the pressure gradient between these regions is increased) and b) the negative phase where these are weakened (the pressure gradient decreases; see Figure 2.9 for a schematic representation of the NAO pattern). The Greenland Blocking Index (GBI) emphasizes the northern half of this dipole and is computed as the mean geopotential height at 500 hPa over the Greenland area (60-80°N, 20-80°W, Figure 2.10) (Hanna et al., 2013). These two climate indicies are highly negatively correlated. Weather patterns/variability associated with both the NAO and GBI have been shown to have a significant effect on the GIS. Moisture over the GIS is sourced predominately from southwesterly winds (Mosley-Thompson et al., 2005; Bromwich et al., 1999). During the postive NAO, stronger westerlies south of Greenland reduce this flow while during the negative NAO the southwesterly flow over the ice sheet is enhanced. Enhanced southerly flow during the negative NAO is also responsible for

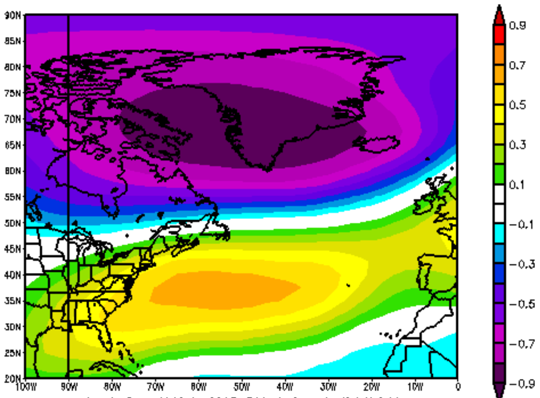

Jan to Dec: 1948 to 2013: 500mb Geopotential Height
Seasonal Correlation w/ Jan to Dec NAO
NCEP/NCAR Reanalysis

Figure 2.9: Correlation between NAO and 500 mb geopotential heights for the period 1948-2013.

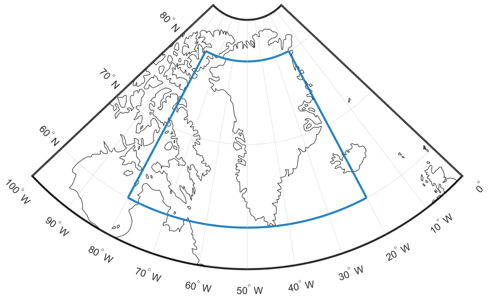

Figure 2.10: Domain of the GBI calculation.

the warm temperature anomalies over the ice sheet (Bromwich et al., 1999; Rogers and Van Loon, 1979).

Hanna et al. (2013) showed that the during the negative phase of the NAO (higher values of the GBI), when high pressure anomalies exist over Greenland, warmer summer temperatures and enhanced meltwater runoff from the GIS are prevalent. This relationship was found to be stronger with the GBI. Seo et al. (2015) found that the NAO was also related to a decrease in recent summer precipitation, further exacerbating the negative summertime mass balance over the

GIS seen more often during the negative NAO. In order for mass balance of the GIS to be achieved, net loss of ice along the periphery of the ice sheet should be balanced by ice precipitation over the interior. It should be noted there are some regional differences in the correlation between precipitation and the NAO and that Arctic warming could be influencing this relationship (Calder et al., 2008; Mosley-Thompson et al., 2005). The NAO and precipitation are more highly related in western Greenland (Mosley-Thompson et al., 2005). This is the region where the SW winds associated with the negative NAO come onshore.

Most of the recent research on the NAO and Greenland thus far is focused on GIS mass balance. There is presently a lack of knowledge about cloud occurrence, specifically if the large-scale patterns outlined above have any relation to cloud occurrence in general or the occurrence of particular cloud types over the GIS. Since both the large-scale atmospheric setup (Hanna et al., 2013; Seo et al., 2015) and the presence of low level mixed phase clouds (Bennartz et al., 2013; Van Tricht et al., 2016) have separately been shown to influence GIS melt, it is of interest to explore potential links between the large scale and the presence of mixed phase clouds over the GIS. Understanding the natural variability of the Greenland climate is likely key to understanding how Greenland's climate may change in the future. Several studies have found that the NAO has been in a more persistent negative phase over the past decade (Hanna et al., 2015; Belleflamme et al., 2015) although it is unclear if this is related to climate change or the internal variability of the NAO itself. If the NAO is indeed related to cloud occurrence, then this will have a large impact on predictions of the future climate of Greenland given the large impact clouds have on the Arctic radiation budget.

2.4.3 Precipitation over the GIS

Most of Greenland's precipitation occurs over approximately the southern third of the ice sheet, especially along the southern and southeastern coast (Schuenemann et al., 2009; Schuenemann and Cassano, 2009). Annual average precipitation is lowest over the interior and northern portions of the ice sheet. Precipitation over the Greenland Ice Sheet is strongly related to the interplay between cyclones and the terrain of the ice sheet (Schuenemann et al., 2009). Greenland is located just north of the Atlantic storm track so it is regularly affected by cyclones to the south. Analysis from Schuenemann et al. (2009) also indicates that cyclones can approach Greenland from Baffin Bay to the west or from the Arctic Ocean to the north, however, these are less frequent. The interplay between the different flow patterns set up by the varying location of cyclonic weather systems which can affect the GIS and the steep slope of the ice sheet leads to orographic lift which is an important factor for precipitation especially along the ice sheet's edge (Schuenemann et al., 2009; Schuenemann and Cassano, 2009). Cyclones approaching the ice sheet from Baffin Bay have been found to contribute the most to Greenland precipitation since they both lead to precipitation over the western portion of the ice sheet as they first approach and the southern/southeastern coasts as flow wraps around the cyclone and lifts along the steep slope of the ice sheet. Precipitation over the GIS is predicted to increase everywhere in the future due to climate change (Schuenemann and Cassano, 2010). This is attributed to both a northward shift of the Atlantic storm track coupled with increasing temperatures which allows for a greater capacity of water vapor to be held by the atmosphere. Snowfall at Summit exhibits a pronounced seasonal cycle with a maximum in the summer and minimum in the spring (Castellani et al., 2015). Snowfall was also found to occur most frequently when the near surface wind at Summit had a southerly component.

2.4.4 Clouds and the GIS

Summit, Greenland is a particularly unique environment in the Arctic. Summit lies at the top of the GIS at about 3.2 km above sea level and 72°N. This high elevation polar setting leads to surface temperatures which remain below freezing virtually year round. Mean surface temperatures range from approximately -10°C to -45°C over the course of the year (Steffen and Box, 2001). This has implications for cloud radiative forcing (CRF) over the GIS. CRF is defined as the difference in surface radiation between cloudy and clear sky conditions. Other locations generally experience a negative CRF during the summer (Curry and Ebert, 1992; Shupe and Intrieri, 2004), at least in part due to diminished albedo. However, Summit maintains a high albedo year round. Miller et al. (2015) found that clouds have a net warming effect throughout the annual cycle at Summit. This high summertime albedo means that, without clouds, a significant portion of the impinging solar radiation would reflect off the surface and the surface would cool through longwave emission. The presence of clouds acts to trap longwave radiation, thus the clouds have a net warming effect. In areas where the surface albedo decreases due to snow/ice melting in the summer, a cloud free atmosphere would allow solar radiation to reach the surface and be absorbed whereas a cloudy atmosphere would prevent much of this solar radiation from reaching the surface.

Meteorological research at Summit has increased in recent times in part due to new observations as part of the ICECAPS program (Shupe et al., 2013). ICECAPS was initiated due to the growing recognition of the importance of clouds in relation to Arctic climate and the need for improved observations of these aforementioned clouds especially over Greenland's interior. ICECAPS was also driven by the need to better understand Greenland's climate given the effects that climate change is having on the ice sheet.

ICECAPS deployed a suite of ground based remote sensors designed to obtain both cloud and tropospheric properties. These instruments have been in place at Summit since the summer of 2010 and will continue data collection through the summer of 2018. These sensors include radar and lidar observations which can determine cloud and precipitation occurrence as well as cloud phase. Measurements from passive microwave and infrared remote sensors can be used to derive temperature and moisture profiles as well as column integrated LWP and precipitable water vapor (PWV). Some initial ICECAPS research is outlined below.

Surface based inversions are common on the GIS due to strong radiative cooling of the surface through longwave emission (Miller et al., 2013). However, Miller et al. (2013) showed that the presence of cloud liquid can decrease the inversion strength quickly due to trapping of this radiation, again emphasizing the importance of liquid bearing clouds on the surface radiation budget. Liquid bearing clouds also have an impact on snowfall at Summit. Castellani et al. (2015) found that clouds with relatively low LWP values have high precipitation rates possibly indicating that the WBF process was enhanced thus depleting liquid water from the cloud.

Mixed phase clouds over the GIS are particularly important for study due to their effect on the mass balance of the GIS. Bennartz et al. (2013) found that warm advection over the ice sheet coupled with cloud LWP values between 10 and 40 $g\ m^{-2}$ were both necessary components of the historic July 2012 melt event of the GIS where nearly the entire ice sheet experienced melt (Figure 2.11). In this range of LWP, the cloud is emitting LW radiation close to its maximum value (i.e., the cloud is nearly opaque in the infrared), yet a large fraction of the downwelling solar radiation is able to transmit through the cloud and reach the surface. The large-scale melting over the ice included the region around Summit, where the ice surface had not melted since 1889 (and only experiences melt about once every 150 years) according to ice core data (Buis and Cole, 2012). This cloud radiative effect was aided by the advection of warm air from the North American continent to the western coast of Greenland (Neff et al., 2014).

Further analysis of cloud effects on the GIS was performed by Van Tricht et al. (2016) who found that both ice only and liquid bearing clouds have a negative impact on the mass balance of the GIS through two supporting mechanisms. Enhanced sublimation of the GIS and a reduction in refreezing of meltwater (the dominant feedback between the two studied) enhance runoff from the ice sheet when clouds are present. Given that climate simulations predict an increasing rate of mass loss from the GIS (Vizcaino et al., 2015), it is vital to understand what potential role clouds have for the future of the ice sheet. This includes a better understanding of the occurrence (e.g. frequency of occurrence, seasonality, interannual variability) and maintenance of liquid bearing clouds.

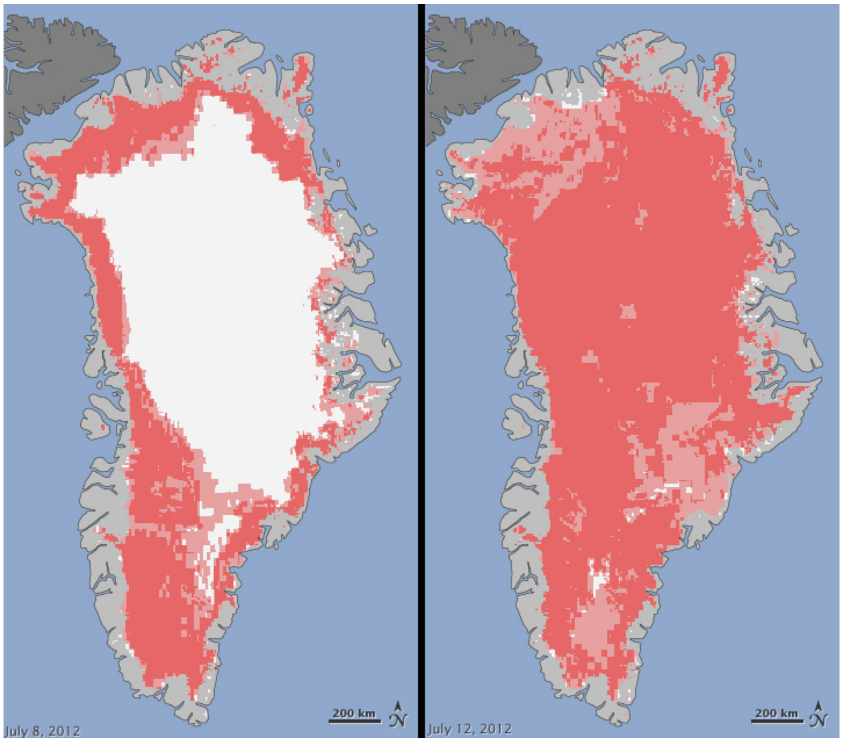

Figure 2.11: Greenland Ice Sheet melt on July 8, 2012 (left) and July 12, 2012 (right). Light red shading indicates "probable melt" (one satellite detected melt) and dark red shading indicates "melt" (more than one satellite detected melt). From Buis and Cole (2012)

Chapter 3

Data and Methodology

3.1 Observations at Summit

As part of the ICECAPS project, a suite of ground based instruments designed to measure cloud and tropospheric properties has been in place at Summit since the spring of 2010. This includes radiosondes which are launched twice daily at Summit (0 and 12 UTC) providing measurements of the vertical structure of pressure, temperature, and relative humidity (for the entire ICECAPS period) and horizontal wind speed and direction (beginning in the summer of 2011). One minute averages of surface pressure, temperature, relative humidity, and horizontal wind are also available for the entire ICECAPS period from a surface meteorology station. A large number of ground based remote sensors are also available. A description of the remote sensors most pertinent to this thesis is contained below and summarized in Table 3.1. For a complete summary of the ICECAPS instrumentation at Summit see Shupe et al. (2013). Subsequently, other data sources used in this analysis, which are not specifically part of the ICECAPS program, will be discussed as well.

3.1.1 Microwave Radiometer

Two microwave radiometers (MWRs) are in operation at Summit. The Humidity and Temperature Profiler (HATPRO) measures downwelling radiance at fourteen frequencies from 22 to 58 GHz while the high frequency microwave radiometer (HFMWR) measures downwelling radiance at 90 and 150 GHz (Rose et al., 2005; Turner et al., 2007). The two instruments are configured together so that observations are made simultaneously at a 2 second resolution. Observations are made horizon to horizon in a single azimuthal plane every ten minutes with multiple zenith observations in between. For the work presented in this thesis only the zenith observations are used.

The MWRs contain a single blackbody target used for calibration. The instruments observe the blackbody at ambient temperature and again with energy added to the system via a noise diode (ND). The difference between the two measurements in referred to as the gain. The ND adds a fixed amount of energy to the system, so the measured gain can be compared to the expected gain. However, this calibration is dependent on knowing the temperature of the ND, so the diode itself must be calibrated in order to obtain accurate measurements (Han and Westwater, 2000; Brown et al., 2007). The temperature of the ND is determined by the tipping-curve calibration (Han and Westwater, 2000; Maschwitz et al., 2013). If viewing the atmosphere at multiple elevation angles, the difference between MWR measurements is primarily due to changes in optical depth of the atmosphere. This difference is theoretically known providing that the atmosphere is plane-parallel (i.e. no horizontal variations in atmospheric constituents or temperature). The tipping calibration is performed during clear sky periods at Summit since the atmosphere can be approximated as plane parallel at these times.

Column integrated precipitable water vapor (PWV) and liquid water path (LWP) are retrieved from measurements taken by the MWRs using an updated

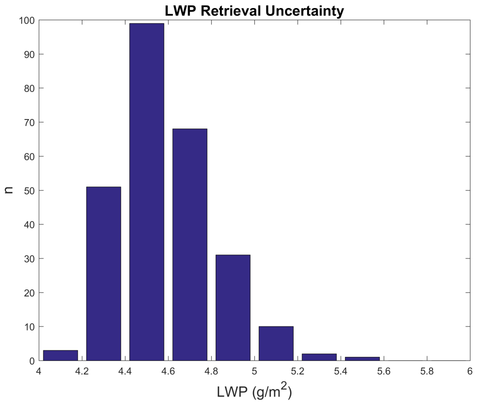

Figure 3.1: Histogram of average uncertainties in LWP during each LBC cloud case at Summit.

version of the algorithm described by Turner et al. (2007). The LWP of Arctic clouds can often be lower than 20 $g\ m^{-2}$ (recall Section 2.2). At Summit, a typical range of LWP during cloudy conditions is 5 to 50 $g\ m^{-2}$ (see Section 5.3 below). The original retrieval algorithm used measurements from 23 and 34 GHz to obtain LWP, but a retrieval using only these two frequencies leads to errors between 20 and 30 $g\ m^{-2}$ of LWP. This leads to not only uncertainty in the magnitude of the LWP in a cloud, but makes it difficult to unambiguously determine whether there is any liquid in a cloud using a MWR if the cloud has a relatively small amount of liquid. However, the retrieval's uncertainty can be significantly decreased by the use of data from higher frequencies in addition to the two standard frequencies (Cadeddu et al., 2013). At Summit, measurements from 23, 34, 90, and 150 GHz are used in the retrievals of LWP. In addition, a model with an improved treatment of liquid water absorption (especially at temperatures less than 0°C) is used (Turner et al., 2016). These improvements lead to an average uncertainty of less than 5 $g\ m^{-2}$ in the retrievals of LWP at Summit when liquid bearing clouds are detected (Figure 3.1); this algorithm will be described below in Section 3.2.

3.1.2 Precipitation Occurrence Sensor System

The Precipitation Occurrence Sensor System (POSS) is a horizontally polarized X-band radar designed to measure near surface backscatter (Sheppard, 2007). This backscatter is measured in a single sample volume near the surface at a temporal resolution of one minute allowing for surface precipitation properties to be derived. Specifically for the work herein, the POSS data are used to obtain high temporal frequency measurements of snowfall rate. Although initially used primarily to investigate liquid phase precipitation, more recent work has made use of (and validated) the POSS for solid state precipitation (Sheppard and Joe, 2008).

3.1.3 Micropulse Lidar

The Micropulse Lidar (MPL) is polarization sensitive lidar which can sense clouds and aerosols up to 20 km above ground level (Campbell et al., 2002; Flynn et al., 2007). At Summit, the MPL has a 3 s temporal resolution and 15 m vertical resolution. In order to discriminate between liquid and ice particles, the MPL sends out alternating pulses of linear and circular polarization. The linear depolarization ratio (δ_{linear}) can then be calculated using the following equation:

$$\delta_{linear} = \frac{P_{\perp}(0)}{P_{\perp}(\frac{\pi}{2}) + P_{\perp}(0)} \tag{3.1}$$

where $P_{\perp}(\frac{\pi}{2})$ is the return from the circularly polarized channel and $P_{\perp}(0)$ is the return from the linearly polarized channel (Flynn et al., 2007). $\perp$ indicates that the receiver of the MPL only detects radiation which is orthogonal to the outgoing pulse. δ_{linear} provides an indication of particle phase. Small liquid particles, such as cloud drops, are spherical and generate little to no depolarization of incident radiation while ice crystals have more complex geometry which often leads to incident radiation scattering off of multiple internal surfaces of the crystal and emerging in a different polarization state (Sassen, 1991; Weitkamp, 2006). An example of MPL data, including δ_{linear}, is included in Figure 3.3. A liquid bearing cloud is present from approximately 9-18 UTC and is characterized by low values of δ_{linear}. Higher values of δ_{linear} are observed around 1 UTC, 6 UTC, and from approximately 18-24 UTC indicating the presence of ice crystals.

Several standard corrections need to be applied to the MPL data before it is used for any analysis. When a photon is detected, the receiver is temporarily unable to detect another photon (this is referred to as deadtime), so if too many photons impinge on the receiver in a short amount of time the receiver will miss some of the photons and underestimate the true strength of the signal. A correction algorithm is applied to offset this effect (Connor Flynn, personal correspondence). Next, background radiation is removed from the lidar signal. The MPL's receiver takes in data just before every laser pulse so that only ambient radiation is sensed initially (essentially the lidar is acting as a passive remote sensor during this time). This can then simply be subtracted out of the backscattered signal. Lidar signal falls off as $\frac{1}{r^2}$ so the measured signal is then multiplied by range squared. The next correction is needed due to the fact that the effective field of view of the lidar receiver only partially overlaps the effective area of the transmitted laser beam at low levels. This problem is illustrated schematically in Figure 3.2. A correction was applied from 0 to 2.5 km for the MPL at Summit (Dave Turner, personal communication). The last correction normalizes the received power using the output power of the MPL's laser. This accounts for potential differences in the strength of the outgoing laser pulse.

The MPL at Summit has also suffered from poor polarization measurements likely due to a malfunction in the MPL's liquid crystal retarder (the component of the MPL which controls polarization state). A correction algorithm using the methodology of Hayman and Thayer (2009) was used to correct the data (see Appendix A for a description of the correction algorithm).

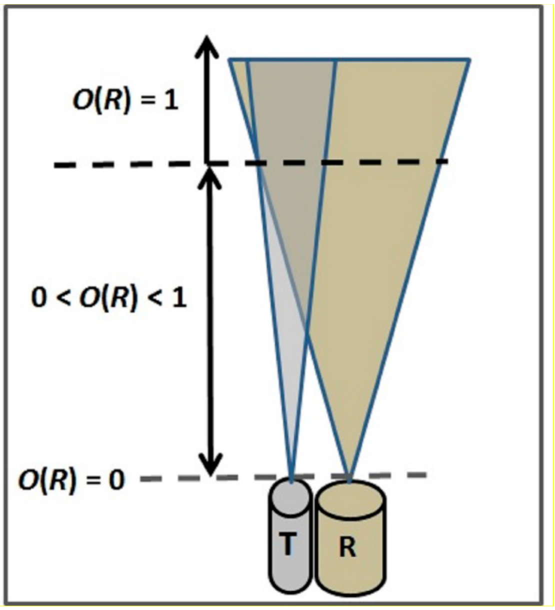

Figure 3.2: Schematic illustrating the overlap between the receiver (R) and transmitter (T) of a simple lidar system. The upper black dashed line indicates where the overlap correction is no longer needed. From (Pal, 2014)

In addition to δ_{linear}, two other quantities of interest are computed from the measured MPL signal. First the total backscatter (BST) is computed using the following equation from Flynn et al. (2007):

$$BST = P_{\perp}(0) + P_{\parallel}(0) = P_{\perp}(\frac{\pi}{2}) + 2P_{\perp}(0) \tag{3.2}$$

where $P_{\parallel}(0)$ is a derived quantity representing the power returned to the MPL in the linear channel with the same polarization as the outgoing laser pulse. This must be derived since the MPL only receives power in the orthogonal polarization state of the transmitted laser pulse (i.e. perpendicular linear polarization relative to the outgoing laser for the linear channel and circular polarization of the opposite rotational sense for the circular channel). The liquid layer from the MPL example referenced earlier is characterized by higher backscatter than the ice clouds (Figure 3.3). Second, the signal to noise ratio (SNR) was computed by dividing the lidar signal by the background radiation which was computed and subtracted out of

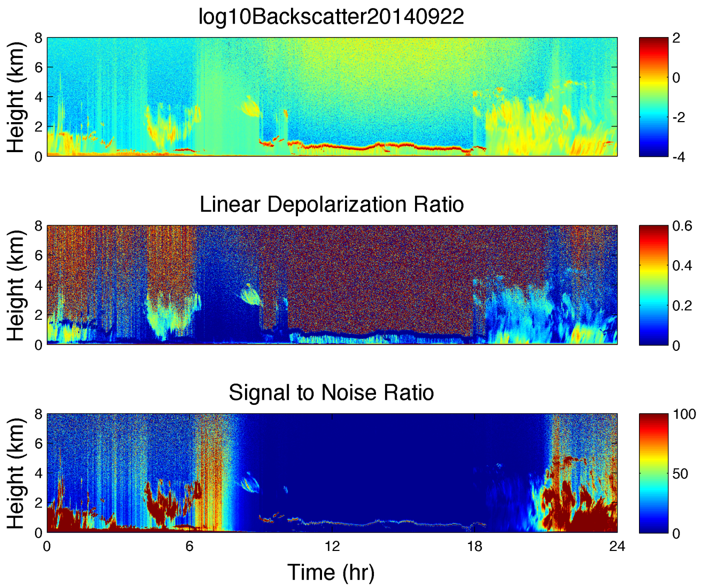

Figure 3.3: Example MPL data from September 22, 2014. Top panel is BST, the middle panel is δ_{linear}, and the bottom panel is SNR.

the lidar backscatter as part of the standard corrections described earlier. All clouds present in the MPL example are characterized by high SNR indicating the scattering of the laser pulse by the clouds is significantly larger than the background radiation and molecular scattering present during clear periods (Figure 3.3).

3.2 Cloud Detection Using MPL Data

For this thesis, the MPL was used for the detection of liquid layer(s) in clouds over Summit. The goal is to determine what influence both the large scale atmospheric circulation and local processes at Summit might be having on liquid bearing clouds which have been shown to significantly influence the surface energy and mass budgets (as discussed in Chapter 2). In order to isolate cases where liquid bearing clouds are both present and are potentially having a significant impact on the GIS, the presence of liquid layers over Summit with a minimum length of six hours were identified using MPL and radiosonde data. This is performed in a three step process described below.

First, a time by height cloud mask using MPL data is produced. Three variables from the MPL are used: BST, δ_{linear}, and SNR. Two-minute running means of these variables are used in making the cloud mask due to the noisiness of some of the data. Initially, cloud presence (phase is not yet considered) is determined by the returned power and whether it is significant enough to indicate the presence of a cloud. This is based off the SNR and BST. If the BST or SNR are above arbitrary thresholds (based on manual analysis of MPL data) then the point is defined as a cloud. In order to define a liquid cloud, δ_{linear} below 0.07 is needed in addition to the BST being higher than a more stringent threshold than the initial BST threshold (since lidar signal is proportional to number concentration, a stronger backscatter signal is expected for liquid particles despite their small size relative to ice crystals in clouds). Once the lidar mask is complete it is augmented by temperature data from interpolated radiosondes at Summit. If the temperature is >0°C, then any point which is defined as ice is redefined as liquid. If the temperature is <-40°C, then any point defined as liquid is redefined as ice.

The second step in determining the presence of liquid cloud layers is to convert the cloud mask into a timeseries of liquid layer presence, height of the lowest liquid layer (if a layer is detected), and the number of layers detected. Since the MPL attenuates quickly when the optical depth of a cloud is high, this last field does not always capture the true number of layers. In order to identify a liquid layer at a particular time, there needs to be at least 45 m depth (three MPL sample height bins) in the cloud mask column at that time which is defined as liquid (similarly in order to define another separate layer there needs to be a gap in liquid of the same depth). This condition is needed in order to prevent misidentification of liquid layers due to noise in the data. While the data used for the cloud mask is averaged temporally with a two minute running mean, there is no averaging applied in the vertical. Averaging was applied to the time dimension only due to the high temporal resolution of the MPL dataset. In order to average over the same amount of data points in the vertical, averaging would need to span 600 m.

Once this timeseries is complete, individual cloud events are then identified. As stated earlier, a minimum length of six hours of liquid detected by the MPL is needed to define an event. In order to declare one event complete and begin another, a gap of at least three hours is needed between times where liquid is detected. This gap length is chosen in order to strike a balance between ensuring cases where the cloud liquid is intermittent, yet consistently present over a significant time period, are considered single events while allowing events with enough temporal separation to be counted separately. However, allowing events to be defined when there is intermittent liquid detected and allowing the gaps in this liquid detection to be up to three hours can, if not corrected, lead to the detection of spurious cases where liquid layers are present only during a tiny portion of the case lifetime. In order to correct for this, once a case is initially defined it is only counted if the percentage of time liquid is present is greater than 80%. Figure 3.4 shows an example of the output of the liquid detection algorithm. This is for the same time period as Figure 3.3. A case was identified from approximately 9-18 UTC on this day.

Figure 3.4 is also a good example of a potential problem with MPL data. There is a liquid layer identified that is essentially adjacent to the ground early in the period. However, this is likely either blowing snow, snow buildup on the glass cover of the MPL, reflection off the glass cover itself, or possibly a liquid fog. This likely misidentified liquid layer adjacent to the ground is seen several times throughout the dataset. In order to prevent these spurious cases from being identified, the algorithm only considers data from 125 m or higher which eliminates

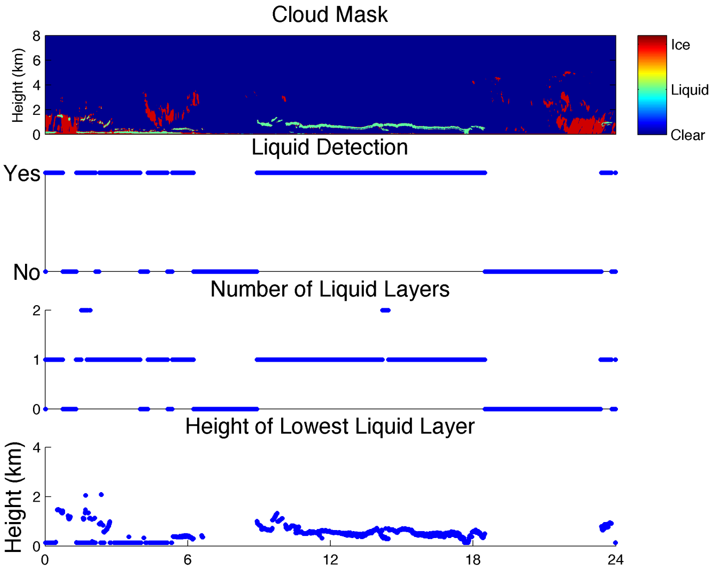

Figure 3.4: Example cloud mask (top panel) and output from the liquid detection algorithm (bottom three panels) for September 22, 2014 (same date as MPL data in 3.3)

these situations and has a negligible effect on events for which there was high confidence in the algorithms results (based off manual analysis of the data).

3.3 Climate Indices and Reanalysis Data

In order assess the large scale environment while liquid bearing clouds are present, potentially pertinent climate indicies, such as the NAO and GBI, are analyzed in relation to the occurrence of liquid bearing clouds detected by the algorithm described in Section 3.2. The daily GBI is obtained from NOAA's Earth System Research Laboratory website (`http://www.esrl.noaa.gov/psd/data/timeseries/daily/GBI/`). The GBI is calculated using data from the NCEP/NCAR 40-year reanalysis project (Kalnay et al., 1996). All other climate indices are obtained from NOAA's Climate Prediction Center website (`http://www.cpc.ncep.noaa.gov/`

`products/precip/CWlink/daily_ao_index/teleconnections.shtml`). Reanalysis data from the European Centre for Medium-Range Weather Forecasts (ECMWF) ERA-Interim reanalysis dataset (Dee et al., 2011) is used to further diagnose the three dimensional large scale atmospheric setup over Greenland in relation to liquid occurrence in clouds. Variables from this dataset which are used in the following analysis include temperature, horizontal winds, specific humidity, relative humidity, and geopotential. Parcel back trajectories are computed using NOAA Air Resources Laboratory's (ARL) Hybrid Single-Particle Lagrangian Integrated Trajectory (HYSPLIT) model (Stein et al., 2015; Draxler and Hess, 1998). Data for HYPSLIT trajectories is from the Global Data Assimilation System (GDAS) at 1°horizontal resolution and three hourly temporal resolution (Kanamitsu, 1989).

Instrument	Measurement(s)	Derived Parameter(s)
MWRs	Downwelling brightness temperatures from 22 to 58 GHz, 90, and 150 GHz	LWP, PWV
MPL	Backscatter and depolarization	Cloud boundaries, cloud phase
POSS	Reflectivity	Precipitation rate
Radiosondes	Temperature, pressure, RH, and winds	Cloud temperature
Surface Met. Station	2 and 10m air temperature, pressure, RH, and winds	

Table 3.1: ICECAPS instruments, measurements, and derived quantities used in this thesis.

Chapter 4

Relationship to Large Scale Atmospheric Circulation

This chapter focuses on the relationship between the occurrence of liquid bearing clouds identified with the algorithm described in Section 3.2 and the large scale atmospheric circulation surrounding Greenland. The primary goal of this analysis is to determine how the large-scale atmospheric setup differs from climatology during the occurrence of LBCs and why these differences favor their occurrence. In addition, the relationship between the LBCs and modes of climate variability will be assessed. A brief discussion of the results of the algorithm will precede this in order to provide context for the later sections.

4.1 Basic Macrophysical Cloud Properties

The liquid detection algorithm was applied from 1 June 2010 (the beginning of the MPL's operational period at Summit) until 30 September 2015 excluding periods where the polarization measurements of the MPL were not robust (see Appendix A). This yielded 326 liquid bearing cloud (LBC) events with a minimum duration of liquid occurrence of 6 hours. Most events are relatively short lived with the majority near the prescribed six hour minimum (Figure 4.1 (a)). However, there is a tail in the distribution with the longest event lasting just over 166 hours. In order to assess the particularly long-lived events in the following analyses, events from the upper quartile of case length will sometimes be discussed separately. This upper 25% of events contains all cases which last for longer than 24.6 hours and will be referred to as the LL subset subsequently for brevity.

There is strong seasonality in cloud occurrence (Figure 4.1 (b)). Over half of the LBC events (51%) occur in the summer (JJA) with fewer cases in each following season (SON - 28%, DJF - 12%, and MAM - 9%). This seasonality is amplified when only considering the LL cases with 71% occurring in JJA, 19% in SON and 5% in both DJF and MAM. This seasonality is similar to that observed at Barrow and during SHEBA for liquid only clouds (Shupe, 2011). However, mixed phase clouds at Barrow, Eureka, and SHEBA and liquid only clouds at Eureka all experienced a maximum in occurrence during the fall (Shupe, 2011). For most cases, the average height of the liquid layer is relatively close to the surface (Figure 4.1 (c)). This is consistent with observations of LBCs from most Arctic locations (e.g. de Boer et al., 2009; Shupe, 2011). Data from the MPL needs to be interpreted with some caution. The MPL attenuates quickly in liquid layers due to the high number of hydrometeors present (lidar signal is proportional to number concentration), so if the optical depth of a layer is greater than approximately 3 the lidar cannot sense anything above the layer as the laser beam will be fully extinguished (Dave Turner, personal communication). Optical depth can be related to LWP using Equation 4.1, where τ is optical depth, ρ_l is the density of liquid water, and r_e is the effective radius of cloud drops (Stephens, 1994). Assuming the effective radius is 10 μm, an optical depth of 3 corresponds to a LWP of 20 $g\ m^{-2}$ which is commonly exceeded in LBCs occurring over Summit (see Chapter 5). This can be considered an upper bound (Dave Turner, personal communication). With this in consideration, the average number of layers during each event should be interpreted

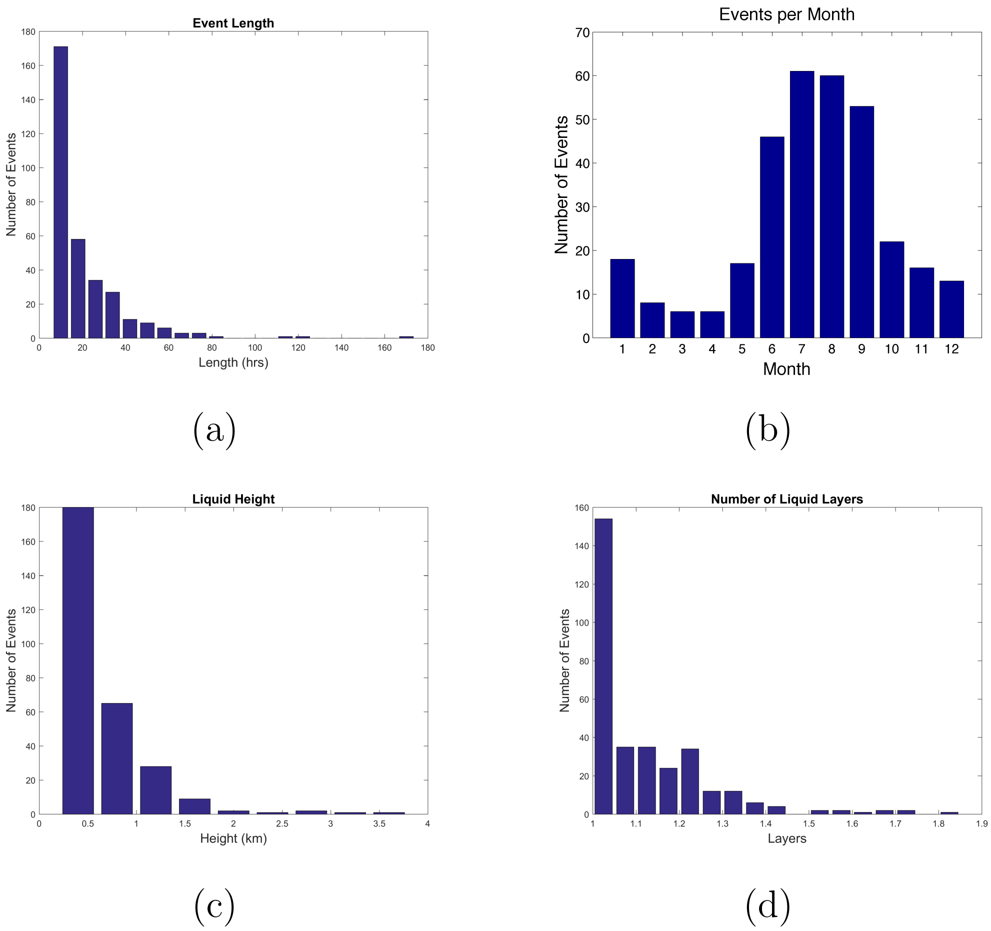

Figure 4.1: Histograms of (a) case lengths, (b) month, (c) average height of the liquid layer (the lowest layer if more than one are detected), and (d) the average number of layers during each event.

as a measure of whether there is a single liquid layer (average number of detected layers is approximately 1) or multiple liquid layers (Figure 4.1 (d)). When there are multiple layers identified, the true number of layers likely cannot be identified from MPL data alone. Figure 4.1 (d) indicates that the majority of cases contain a single layer of liquid.

$$LWP = \frac{2}{3}\rho_l \tau r_e \tag{4.1}$$

Due to the strongly seasonal nature of cloud occurrence outlined above, when calculating anomalies of atmospheric variables using the ERA-Interim reanalysis in the following sections, an anomaly is calculated for each case by subtracting the monthly climatology (1979-2014) from the total field. These individual anomalies are then composited. This is done so that the anomaly plots are relative to cloud occurrence and not the mean differences between seasons.

4.2 Relationship with the NAO

The occurrence of liquid bearing clouds over Summit has a statistically significant relationship to the NAO (Figure 4.2). Specifically, the distribution of the NAO index on days when LBC events begin is shifted towards more negative values of the NAO. The difference between this distribution and climatology is statistically significant using a Kolmogorov-Smirnov (KS) test. The KS test compares two continuous distributions against the null hypothesis that they are from the same distribution. Furthermore, a statistically significant difference is found for each season (Figure 4.3). For the LL subset, the NAO is also more negative and this distribution is significantly different from climatology. However, the distributions of the LL subset and all LBC events were not statistically significantly different from each other.

Other climate patterns analyzed in relation to the cases (Figure 4.4) include the GBI, the Arctic Oscillation (AO), and the Pacific North America Pattern (PNA). As expected given its high anti-correlation with the NAO, the GBI also exhibits a statistically significant relationship with these cloud cases. This index is not included in the following analysis given that it does not provide additional understanding of the occurrence of liquid bearing clouds - it largely contains the same atmospheric pattern as the NAO. The AO exhibits a significant relationship (statistical significance being determined by the arbitrary threshold of 5% using a KS test) to cloud occurrence, but the magnitude of the difference between AO index at case onset and AO climatology is very small. The PNA does not exhibit a

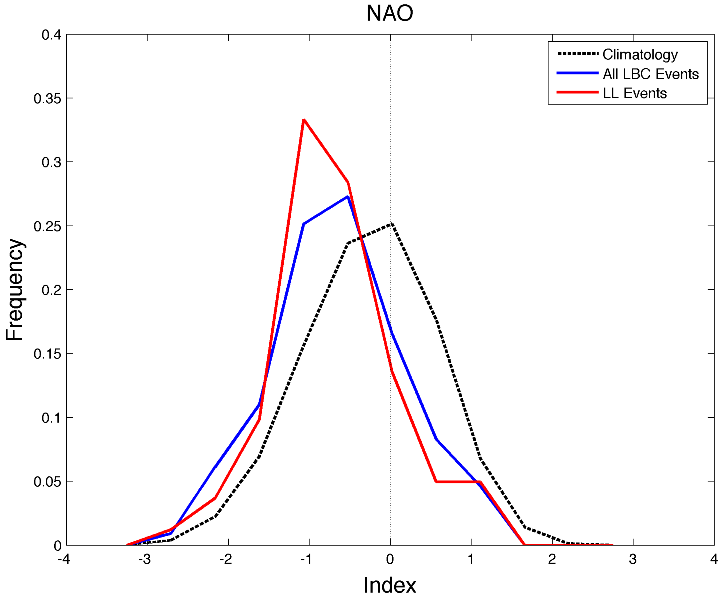

Figure 4.2: Probability density function of NAO index at LBC onset. Black dashed curve indicates 1979-2014 climatology of the daily NAO index, blue curve is the NAO index at cloud onset for all LBC events, and the red curve is the NAO index at cloud onset for the LL subset.

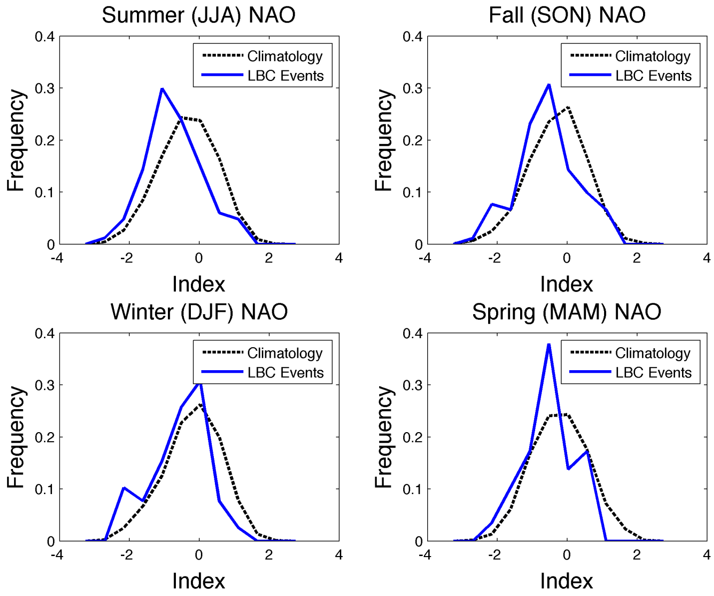

Figure 4.3: Probability density functions of NAO index comparing the seasonal climatologies (black dashed curves) to the NAO index at cloud onset for all LBC events in each season (blue curves)

statistically significant relationship to the occurrence of liquid bearing clouds over the GIS.

Given the NAO correlates to the occurrence of liquid bearing clouds detected over the GIS, the reason behind this relationship is now investigated. Specifically, the question of how the large-scale atmospheric pattern differs from climatology when liquid bearing clouds are observed is explored. As was discussed in Section 2.4.2, the southerly winds during the negative NAO have been shown to bring warm, moist air over the ice sheet leading to positive temperature anomalies (Bromwich et al., 1999) and enhanced precipitation, especially over western Greenland (Mosley-Thompson et al., 2005). The near surface winds during the ICECAPS period range predominately from southwesterly to southeasterly exhibiting a very similar distribution to that found by Steffen and Box (2001). Data from the surface meteorology station at Summit also indicates that southwesterly flow is more

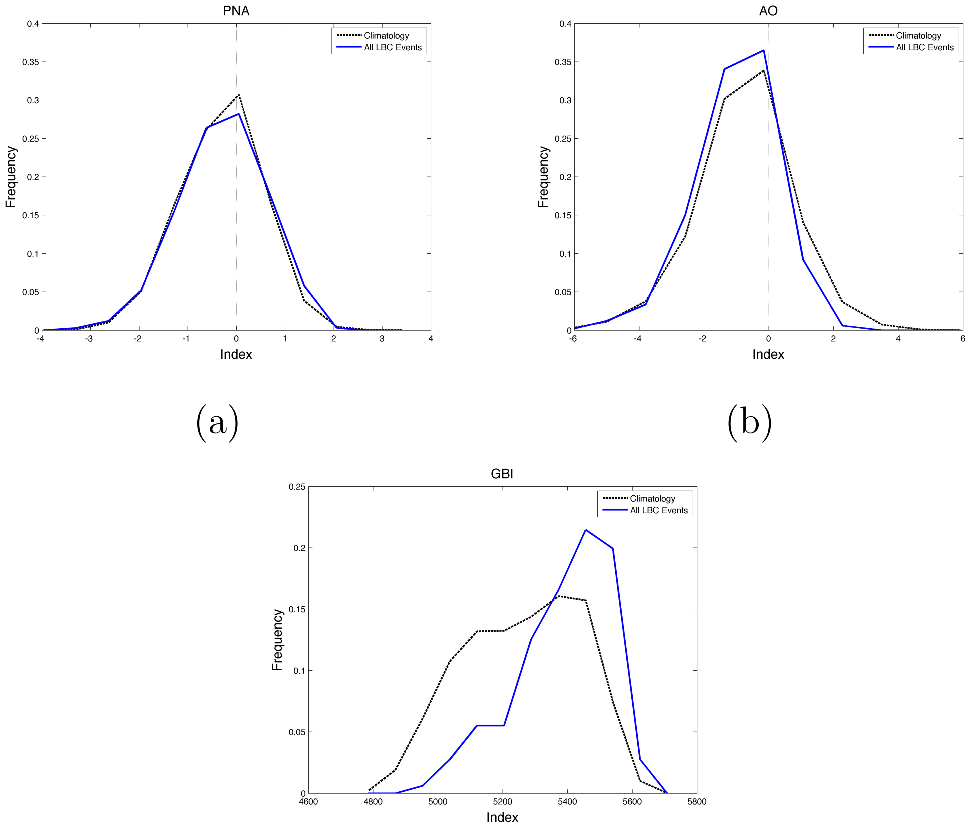

(a) (b)

(c)

Figure 4.4: Probability density functions at LBC onset of the (a) PNA index, (b) AO index, and (c) GBI index. Black dashed curves indicate 1979-2014 climatology of the daily indices and blue curves are the indices at cloud onset for all LBC events.

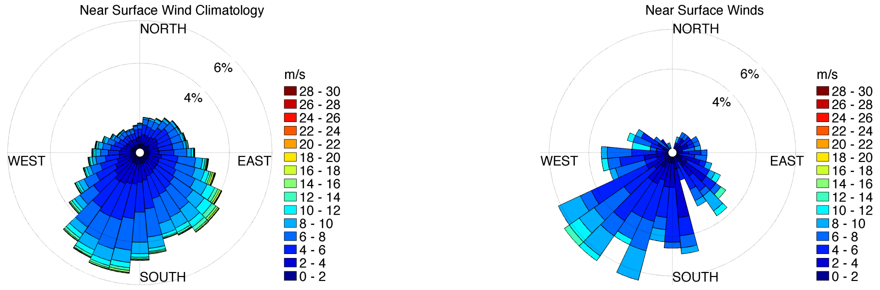

(a) (b)

Figure 4.5: Wind rose from the surface meteorology station data for (a) the climatology of the ICECAPS period and (b) average winds during each LBC event.

predominate over Summit Station during the occurrence of liquid bearing clouds although there is second smaller maxima in wind occurrence from the southeast (Figure 4.5). This indicates that the expected southwesterly flow during the NAO is observed over the center of the ice sheet, at least near the surface. This wind pattern does not change significantly over the lifetime of the clouds - the near surface south-westerlies dominate throughout (not shown).

This southwesterly wind pattern over the ice sheet is also found in ERA-Interim data, where a south-southwesterly (SSW) wind pattern at 650 hPa is evident at the time closest to the onset of liquid bearing clouds (Figure 4.6 (a)). Data from 650 hPa is shown here because most of the liquid bearing clouds identified are at low altitudes and 650 hPa is the lowest level in the ERA dataset consistently above the surface at Summit. The SSW winds extend up through 500 hPa (not shown). At this same time, Greenland is characterized by broad positive temperature and specific humidity anomalies (Figure 4.6 (b-c)). This pattern is consistent with previous research on the NAO noting that the negative phase is correlated with warm, moist conditions across Greenland due to southwesterly winds (e.g. Mosley-Thompson et al., 2005; Rogers and Van Loon, 1979). It should also be noted that simultaneous temperature and specific humidity increases act in opposition when determining the relative humidity (RH) of the environment, which is key for cloud occurrence. At higher temperatures, more moisture is required for an air parcel to reach saturation, a key condition for condensation of cloud drops. The RH anomalies indicate that the air is closer to saturation during LBC events (Figure 4.6 (d)). The positive RH anomalies are not as spatially broad as the specific humidity anomalies indicating that the air is closer to saturation only over the ice sheet itself at 650 hPa, not broadly over the entire analysis region. This is likely due to the relative spatial expanses of the largest temperature and specific humidity anomalies; the specific humidity anomalies are strongest over a smaller area focused over central Greenland while the temperature anomalies are more expansive over the entire plotting domain.

There does not appear to be major differences between the large scale atmospheric setup in the LL cases (Figure 4.7). Comparing to Figure 4.6, very similar spatial patterns are evident in both the specific and relative humidity fields, and although the anomalies are somewhat larger for the LL cases, the atmosphere is anomalously moist over and around the ice sheet in both situations. Similar patterns in both mean wind and temperature anomalies are also evident between the two.

Analysis of 650 hPa RH over the GIS relative to the occurrence of LBCs indicates that the positive anomalies persist during LBC events only - prior to the start of cloud occurrence relative humidity anomalies are negative or near zero in the vicinity of Summit before becoming positive by the onset of cloud occurrence (Figure 4.8). At the end of the liquid bearing cloud events, broad positive relative humidity (Figure 4.9) anomalies are still noted. However, these positive anomalies have decreased in areal extent by this time and continue to do so over the next twelve hours, eventually becoming negligible at Summit (Figure 4.9). This is due

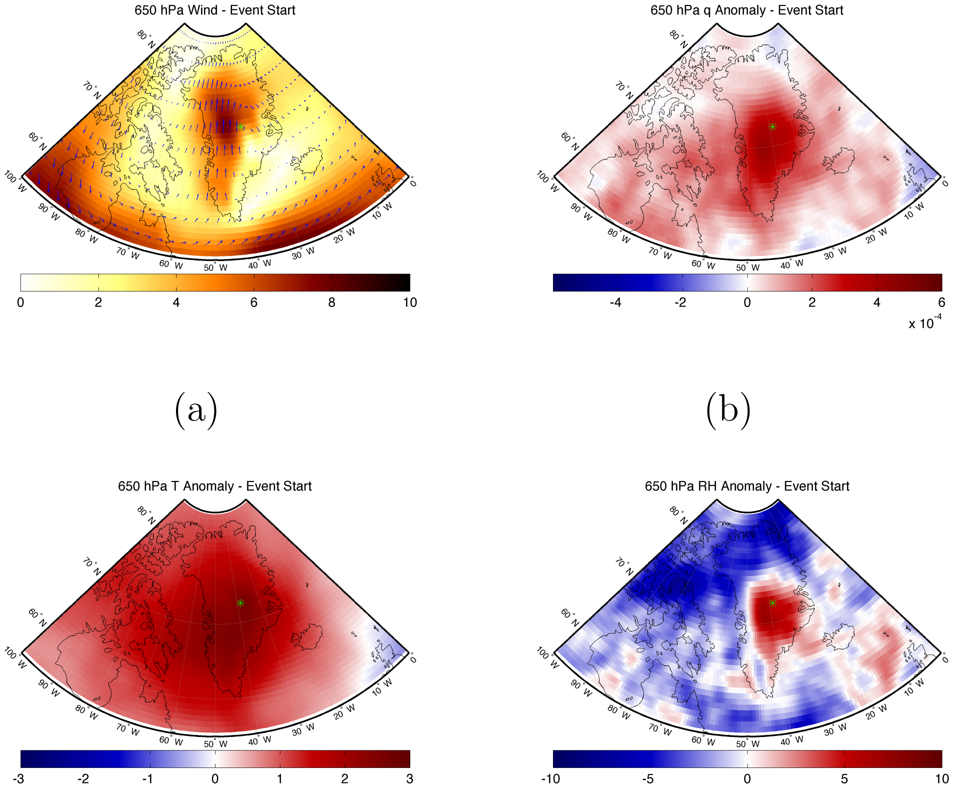

(a) (b)

(c) (d)

Figure 4.6: 650 hPa (a) mean winds ($\frac{m}{s}$), (b) specific humidity anomalies ($\frac{kg}{kg}$), (c) temperature anomalies (K), and (d) relative humidity anomalies (%) at the onset of LBC occurrence for all events. The green asterisk indicates the location of Summit Station.

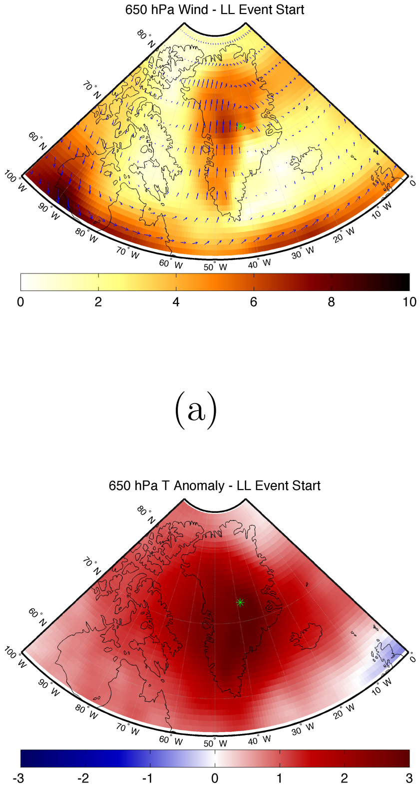
650 hPa Wind - LL Event Start

650 hPa q Anomaly - LL Event Start

650 hPa T Anomaly - LL Event Start

650 hPa RH Anomaly - LL Event Start

(a)

(b)

(c)

(d)

Figure 4.7: Same as Figure 4.6 except for LL cases.

to reduction in the magnitude of the specific humidity anomalies so, despite the fact they are still positive, the moisture anomalies are now no longer significant enough to counteract the positive temperatures over Greenland. As in the previous analysis, very similar patterns exist when only analyzing the LL subset (Figures 4.8 and 4.9).

In order to further investigate characteristics of the anomalous large-scale circulation and its influence on atmospheric moisture content, anomalous horizontal moisture flux ($\overrightarrow{F}$) was computed as follows:

$$\overrightarrow{F} = q'\overrightarrow{U'} \tag{4.2}$$

where q' is the specific humidity anomaly and $\overrightarrow{U'}$ is the horizontal wind anomaly. Twelve hours prior to the beginning of cloud occurrence, the largest magnitudes of $\overrightarrow{F}$ are observed from southwest of the ice sheet to just south of Summit (Figure 4.10). This pattern is set up by anomalously high moisture over the southern portion of the ice sheet and anomalous anticyclonic circulation centered near the southeastern coast of Greenland (Figure 4.10 (b,d)). The anomalous SSW flow on the western side of this anticyclone acts to strengthen the climatological onshore winds over the GIS (Figure 4.10 (d)). This circulation is consistent with a negative NAO pattern, defined by an increase in geopotential height over Greenland. By the time of cloud case start, both the strongest values of $\overrightarrow{F}$ and largest positive specific humidity values have shifted northward toward Summit (Figure 4.11 (a-b)). The anomalous circulation is still centered on the southeastern coast of Greenland continuing to strengthen the southerly component of the mean wind over western and southern Greenland. The flow then curves toward the east over Summit (Figure 4.11 (c-d)). As time continues toward the end of cloud occurrence (and after), this circulation begins to weaken and become disorganized (Figures 4.12 and 4.13). During these times, the specific humidity anomalies over the ice sheet begin to weaken in magnitude likely due to the reduction in transport from

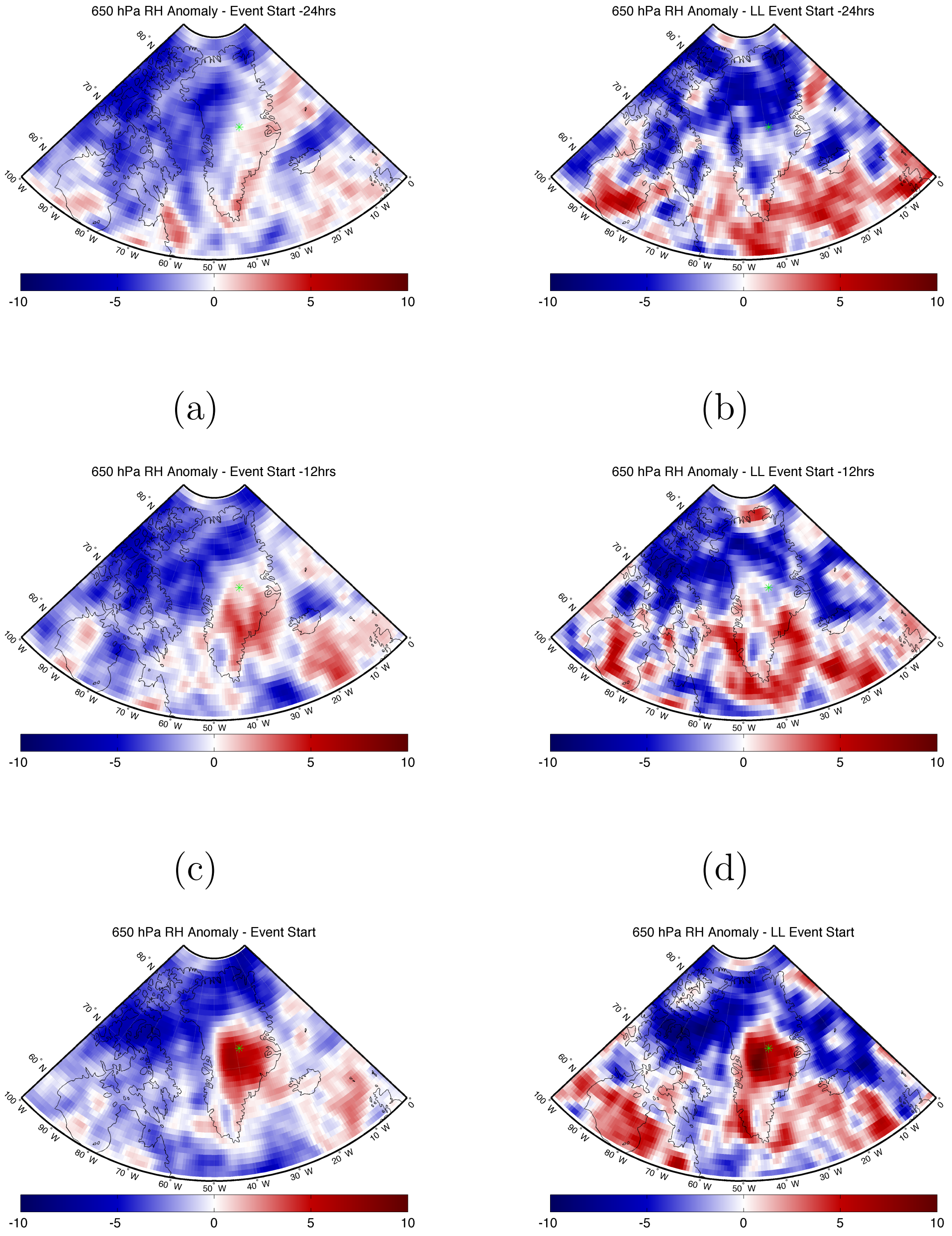

(a) (b)

(c) (d)

(e) (f)

Figure 4.8: 650 hPa RH anomalies for 24 hrs prior to event start (a-b), 12 hrs prior to event start (c-d), and event start (e-f). Compostites of all LBC (LL subset) events are shown on the left (right).

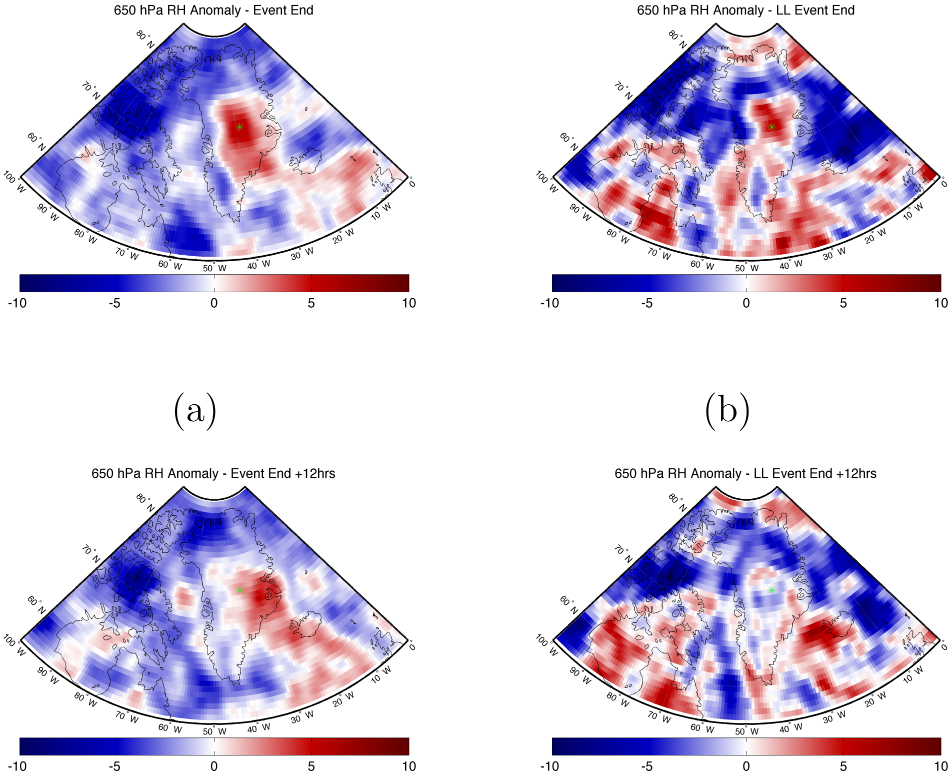

(a)

(b)

(c)

(d)

Figure 4.9: Same as Figure 4.8 except for event end (a-b) and 12 hrs after event end (c-d).

the south. Thus, the magnitude of $\overrightarrow{F}$ decreases toward zero across the domain at these times due to the combination of a weakening of the anomalous anticyclone coupled with the decrease in specific humidity due to this weakened circulation.

The LL subset of cases are qualitatively the same although the magnitudes of the humidity anomalies (and therefore $\overrightarrow{F}$) are increased (not shown). The main difference between all LBC events and the LL subset is the length of time that large values of $\overrightarrow{F}$ are observed both to the south of and in the vicinity of Summit. Values of $\overrightarrow{F}$ 12 hours after the start of cloud occurrence are much larger for the LL cases (Figure 4.14). Since the LL subset of events are all at least 24 hours in length the composite in Figure 4.14 (b) is capturing the environment during the occurrence of liquid bearing clouds while the composite in Figure 4.14 (a) includes many cases where cloud occurrence has already ended since the minimum length is six hours.

In summary, $\overrightarrow{F}$ is illustrating the influence of the anomalous atmospheric circulation set up by the negative NAO on the specific humidity field. Since the circulation is centered on the southeastern coast of Greenland, southerly anomalies are located over the ice sheet itself thus increasing the magnitude of the climatological SSW winds located to the south of Summit. These winds then shift and become more westerly approximately at the latitude of Summit. This flow originates from the south over the Atlantic Ocean, a more moist environment than that over the ice sheet, leading to positive specific humidity anomalies over the ice sheet. These anomalies are initially strongest to the south of Summit before moving north and then gradually weakening. Large values of $\overrightarrow{F}$ persist for longer in the vicinity of Summit when only considering LL cases, indicating the anomalous circulation pattern is in place for longer.

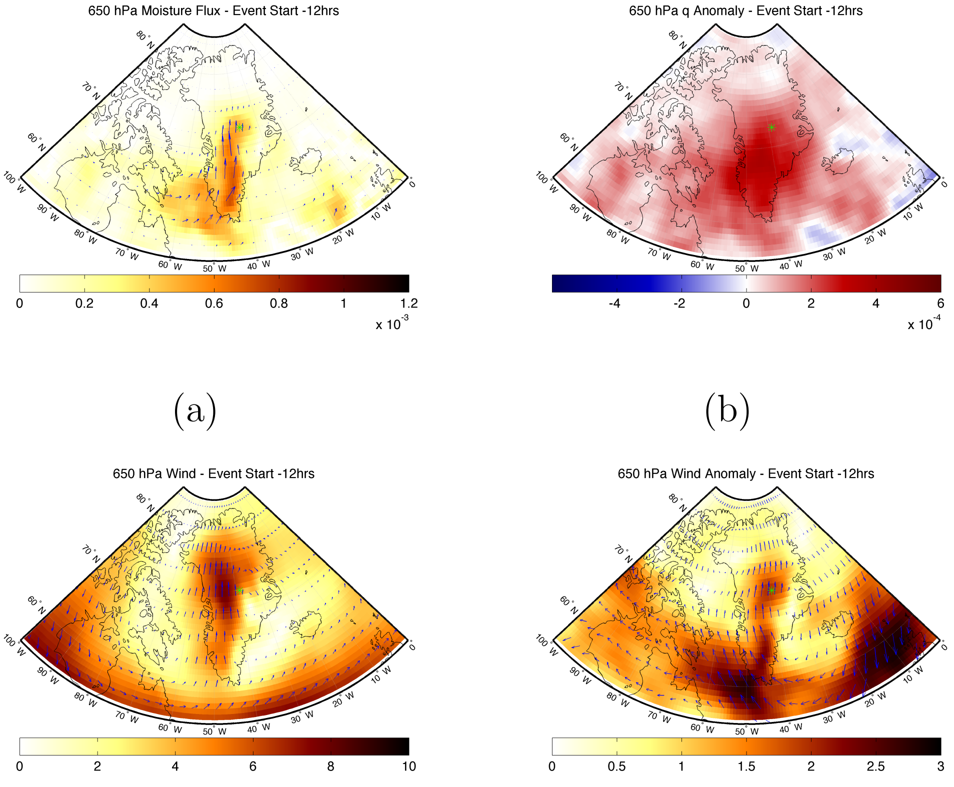

(a) (b)

(c) (d)

Figure 4.10: 650 hPa (a) anomalous horizontal moisture flux vector and magnitude (Equation 4.2) $(\frac{kg}{kg}\frac{m}{s})$, (b) specific humidity anomalies $(\frac{kg}{kg})$, (c) mean winds $(\frac{m}{s})$, and (d) wind anomalies $(\frac{m}{s})$ 12 hours prior to LBC event start. The green asterisk indicates the location of Summit Station.

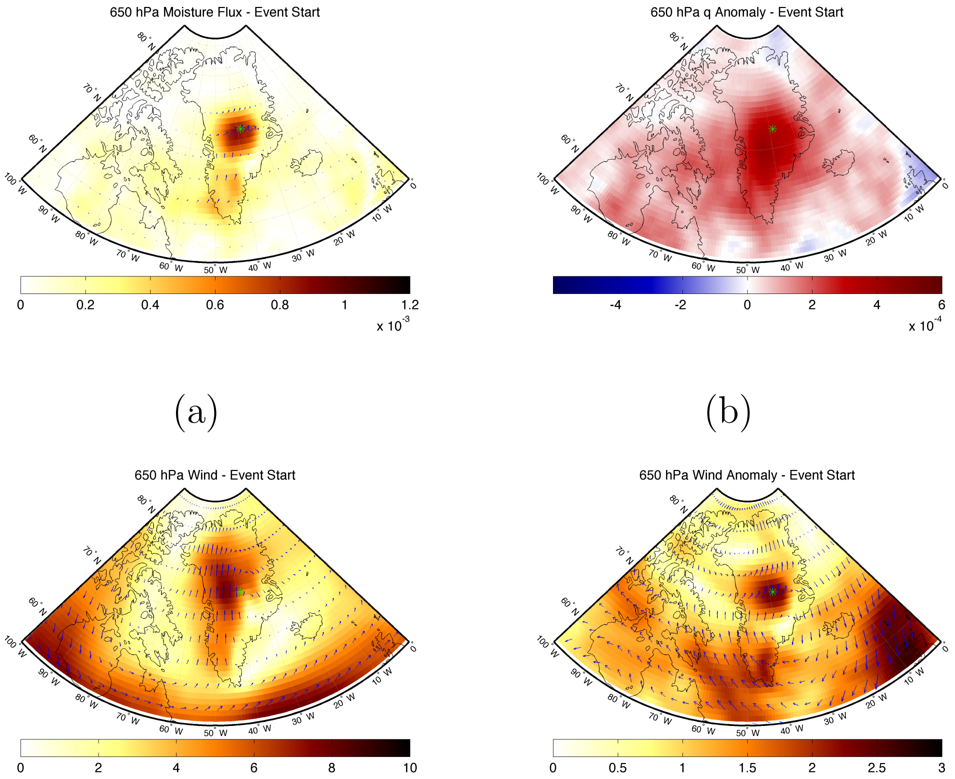

(a) (b)

(c) (d)

Figure 4.11: Same as Figure 4.10 except for event start.

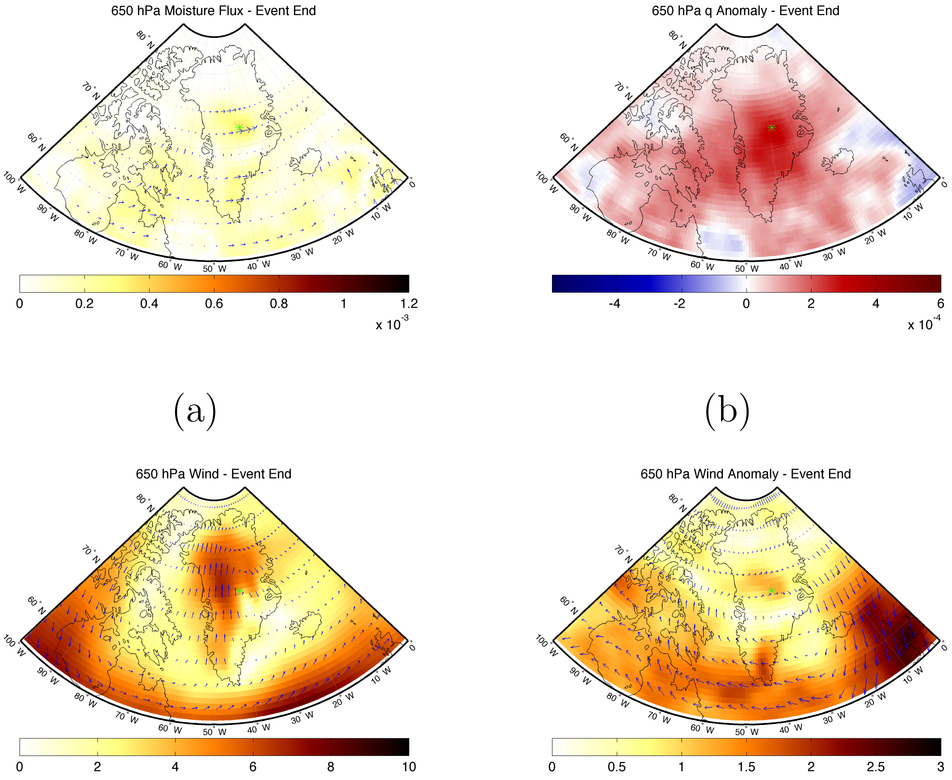

(a) (b)

(c) (d)

Figure 4.12: Same as Figure 4.10 except for event end.

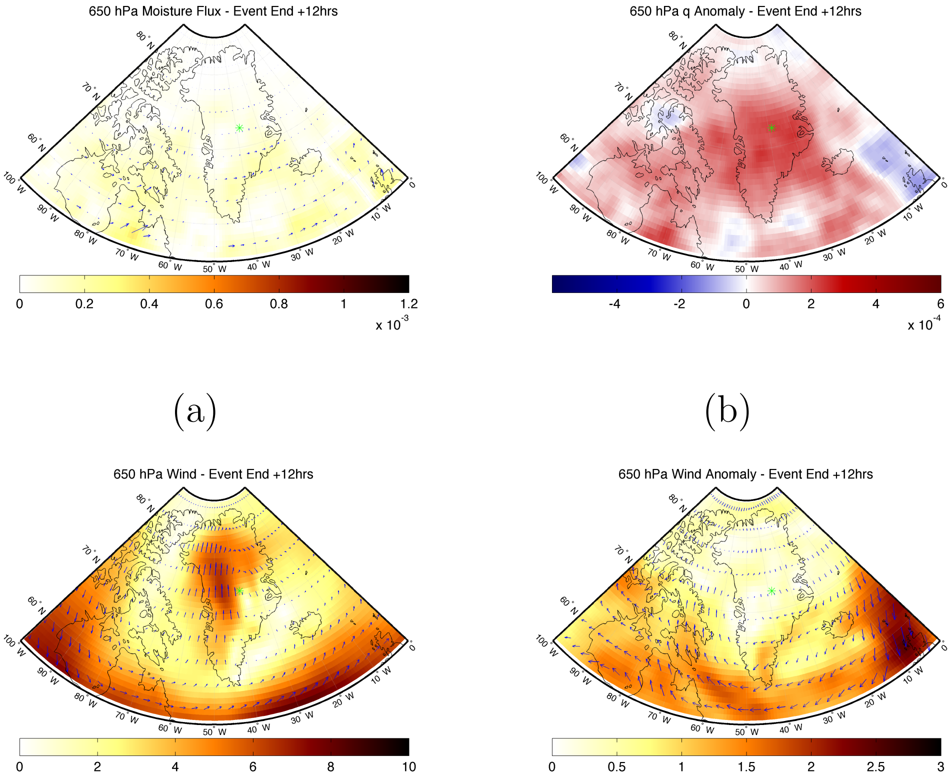

(a) (b)

(c) (d)

Figure 4.13: Same as Figure 4.10 except for 12 hours after event end.

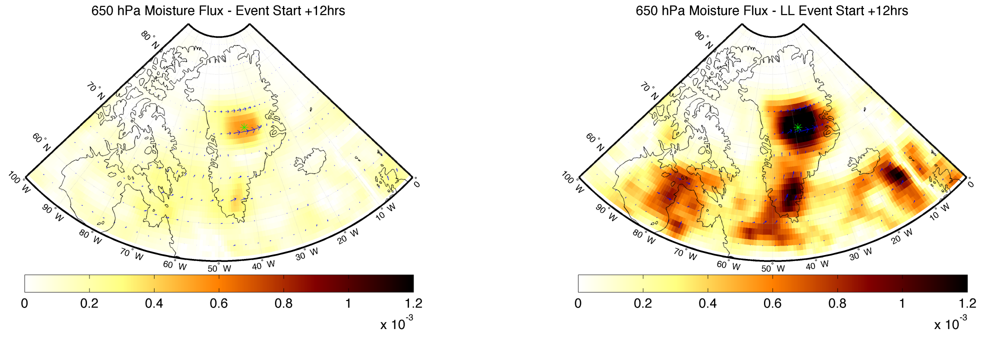

(a) (b)

Figure 4.14: 650 hPa horizontal moisture flux vector and magnitude (Equation 4.2) ($\frac{kg}{kg}\frac{m}{s}$) 12 hours after cloud case start for (a) all LBC events and (b) the LL subset.

4.2.1 Atmospheric Patterns Corresponding to LBCs during the + and - NAO

The negative phase of the NAO corresponds to an increased frequency of LBC events, but the distribution of the NAO index at cloud onset indicates that LBCs occur during both phases of the NAO (Figure 4.2). If there is a lack of a local moisture source, moisture transport to the top of the ice sheet is needed for the occurrence of LBCs. To investigate, atmospheric patterns corresponding to the two phases of the NAO are now analyzed in relation to LBC events in order to determine if the two phases have potentially different mechanisms leading to transport to the top of the GIS. Herein, LBC events beginning when the NAO ≥ 0.5 (≤ -0.5) will be referred to as +NAO (-NAO) events. This threshold yields 46 +NAO events and 145 -NAO events.

Analysis of the geopotential height field during all LBC events and each subset of events discussed in this thesis yields a number of differences in atmospheric setup. The composite for all LBC events indicates there is a ridge over Greenland itself and a trough to the west extending from the southern edge of the Nares Straight through Northern Canada (Figure 4.15). During the LL subset the pattern is almost identical, although the values of geopotential height increase across the entire domain shown. This is likely due to the increase in frequency of LL events during the summer months. The similar pattern in geopotential height is not unexpected given that the distributions of the NAO at the start of LBC events and the LL subset are alike as both contain a disproportionate amount of -NAO events (recall Figure 4.2). During +NAO events the trough to the west of Greenland is located much closer to the ice sheet. In addition, there is a closed low in the height field located along the southeast coast of Greenland. This setup yields two potential flow patterns which could bring moisture over the ice sheet: 1) southwesterly flow on the east side of the trough axis and 2) easterly flow wrapping around lows off the coast of Greenland. During -NAO events, there is a ridge located over central Greenland and southwesterly flow west of the ridge axis is the only evident pattern which could lead to advection of moisture over the ice sheet (as discussed in Section 4.2).

Since composite means can mask the variability of any given field, it is of interest to characterize the spatial variability of the patterns described above. To assess this variability, the number of events for which any value of geopotential height in the plotting domain was above or below one standard deviation of the latitudinal, seasonal mean was computed for the +NAO (Figure 4.16) and -NAO events (Figure 4.17). During the +NAO events, the location of the trough to the west of Greenland is quite variable with low heights relatively common from the western coast of Greenland to the west of Baffin Bay. The closed low noted in the composite (Figure 4.15) appears to vary in location along the southeastern coast of Greenland. High heights only occur toward the border of the plotting domain, away from the ice sheet. During the -NAO events, the highest heights

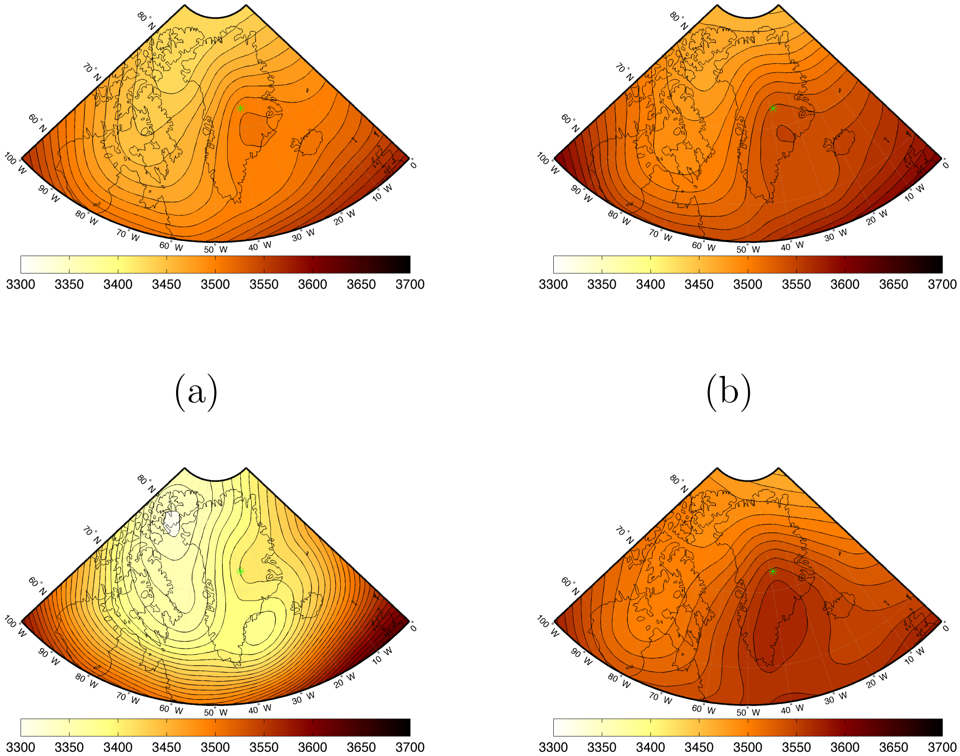

(a)

(b)

(c)

(d)

Figure 4.15: Composite geopotential height (m) for (a) all LBC events, (b) the LL subset, (c) +NAO events, and (d) -NAO events.

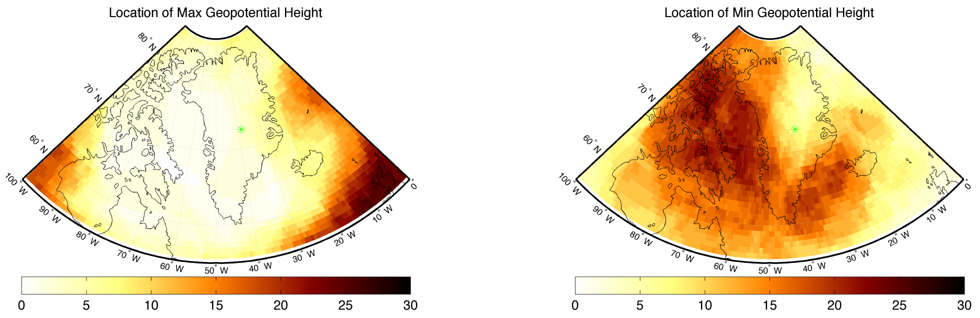

(a) (b)

Figure 4.16: Number of events where the 650 hPa geopotential height is (a) greater than one standard deviation above the latitudinal mean or (b) less than one standard deviation below the latitudinal, seasonal mean at the onset of cloud occurrence for +NAO events.

are generally located over the ice sheet itself, although can occur anywhere in the plotting domain. The trough is pushed further westward and the storm track is located far south of the ice sheet. Low heights occur much less frequently across the plotting domain than high heights during the -NAO.

To verify the inferred source of air parcels during LBC events from the flow patterns outlined above, 72 hour backward trajectories were completed using HYSPLIT (Stein et al., 2015; Draxler and Hess, 1998). Trajectories are initialized at the mean cloud base height at event start. Parcel source is defined herein as the parcel location at 72 hours prior unless one of the following conditions is met: 1) the terrain height is 0 (i.e. the parcel has left the GIS and is over the ocean) or 2) the parcel reaches the ground (since HYSPLIT can continue these parcels along the ground this was considered unphysical and the trajectory was ended at this time). During the -NAO, parcels are sourced most often from the western coast of Greenland as expected given the predominate southwesterly flow during this time (Figure 4.18 (a)). It should be noted that some parcel's are still sourced from the

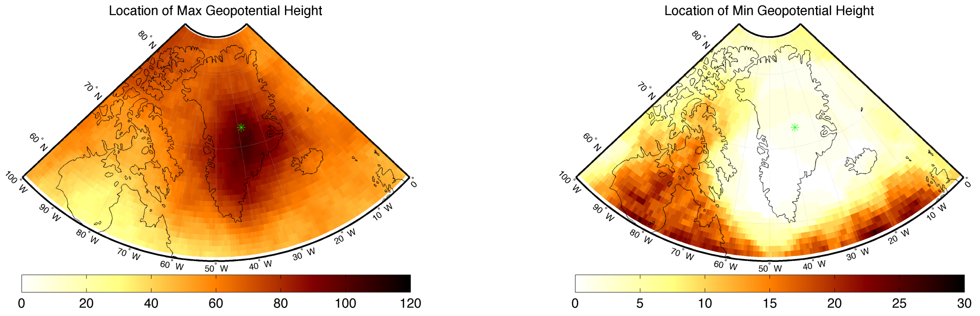

(a)

(b)

Figure 4.17: Same as Figure 4.16 except for -NAO events.

eastern side of the ice sheet during the -NAO. This is likely due to the occurrence of a closed anticyclonic circulation causing parcels to circulate around the center of the ice sheet. Parcel source locations for +NAO cases are also consistent with results discussed earlier in this section. Most parcels are sourced from eastern coast of the ice sheet where low pressure systems are more likely to track during the +NAO. This indicates that of the two possible mechanisms for transport over the ice sheet during the +NAO identified from the geopotential height composite, the low pressure along the southeastern coast is more commonly related to the occurrence of LBCs.

4.3 Orographic Effects

The analyses in Section 4.2 were all at 650 hPa (above the ice sheet) and focused on the horizontal transport of moisture and air parcels. Given that flow at this level was found to be related to moisture intrusion over the ice sheet, it is of interest to further investigate this flow throughout the depth of the troposphere in order to analyze whether orographic lift aids in getting moisture from lower levels, where the water vapor content of the atmosphere is higher, over the ice sheet.

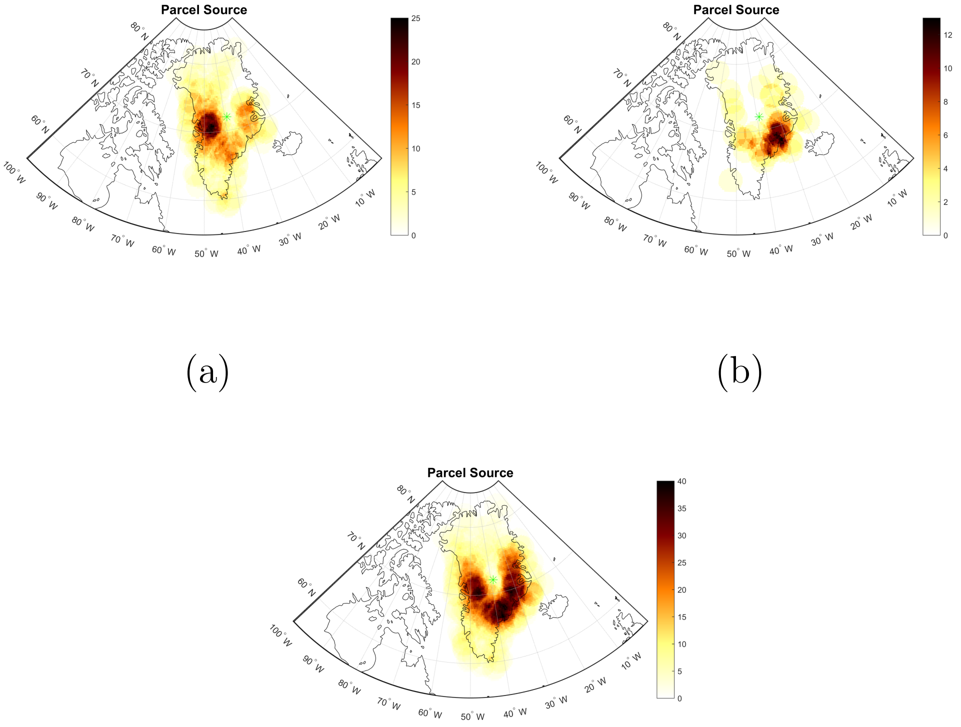

(a)

(b)

(c)

Figure 4.18: Source location of HYSPLIT parcels for (a) -NAO events, (b) +NAO events, and (c) all LBC events. Colors are the frequency of which HYSPLIT parcels are sourced from within 200 km of a point.

Orographic lift has previously been shown to relate to precipitation over the GIS, although much of this work focuses on the edge of the ice sheet where precipitation totals are highest (Schuenemann et al., 2009). There is currently a lack of research exploring the relationship between orographic lift and meteorological processes over the interior of the ice sheet.

Southerly winds are prevalent throughout much of the depth of the troposphere and are anomalously strong over and to the south of the ice sheet both prior to and during the occurrence of liquid bearing clouds (Figure 4.19). However, the largest anomalies in meridional wind occur prior to cloud occurrence. It should be noted that the cross-sections in Figure 4.19 are located to the west of Summit in order to capture the primarily southerly flow which was strongest to the west of Summit (Section 4.2). This flow became more westerly at approximately the latitude of Summit.

Similar to the analyses at 650 hPa, the southerly wind anomalies occur in conjunction with positive specific humidity anomalies. This correspondence extends through the troposphere (Figures 4.19 and 4.20). The strongest anomalies of specific humidity are initially located along the southern base of the ice sheet. They then move northward over the ice sheet as the analysis time moves closer to case start. After event start, these anomalies begin to slowly weaken. These cross-sections appear to indicate that the moisture over the ice sheet itself analyzed during the occurrence of liquid bearing clouds is sourced from the south not only at levels which are above the ice sheet (as investigated in Section 4.2) but also potentially from lower levels as the southerly atmospheric flow encounters the steep terrain on the edge of the ice sheet.

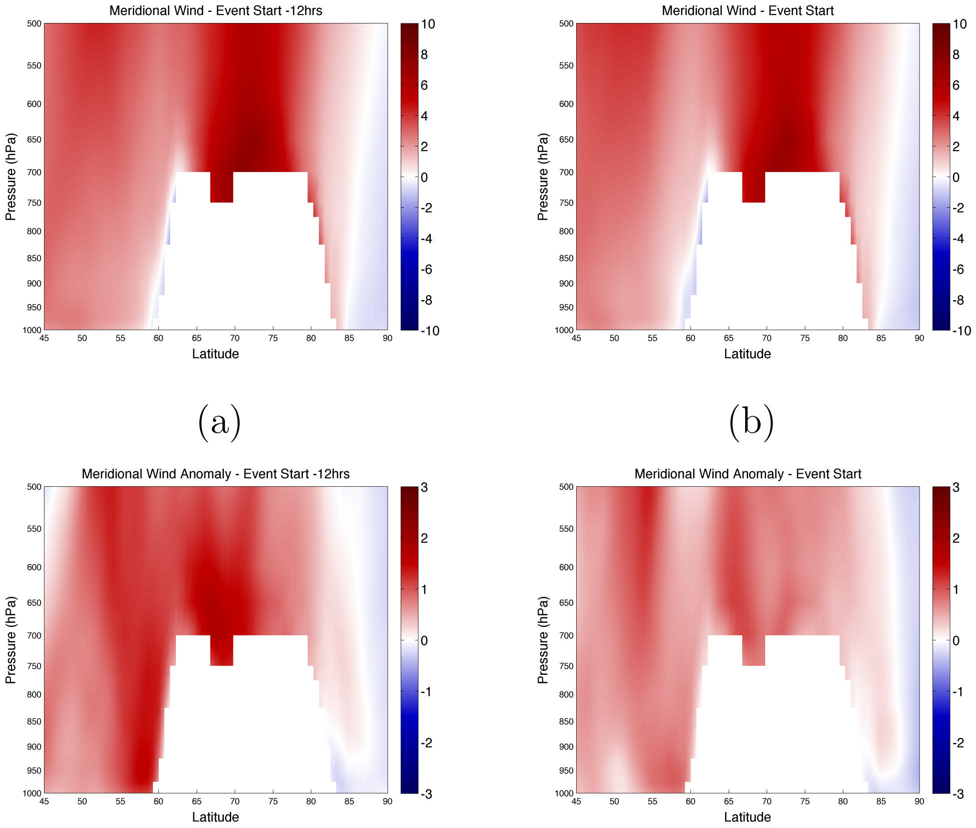
Meridional Wind - Event Start -12hrs

Meridional Wind - Event Start

(a)

(b)

Meridional Wind Anomaly - Event Start -12hrs

Meridional Wind Anomaly - Event Start

(c)

(d)

Figure 4.19: Longitudinal cross-sections of (a,b) meridional mean wind ($\frac{m}{s}$) and (c,d) meridional wind anomalies ($\frac{m}{s}$), at (a,c) 12 hours prior to case start and (b,d) case start. Cross sections centered at 315°E (averaged from 314.25°E to 315.75°E).

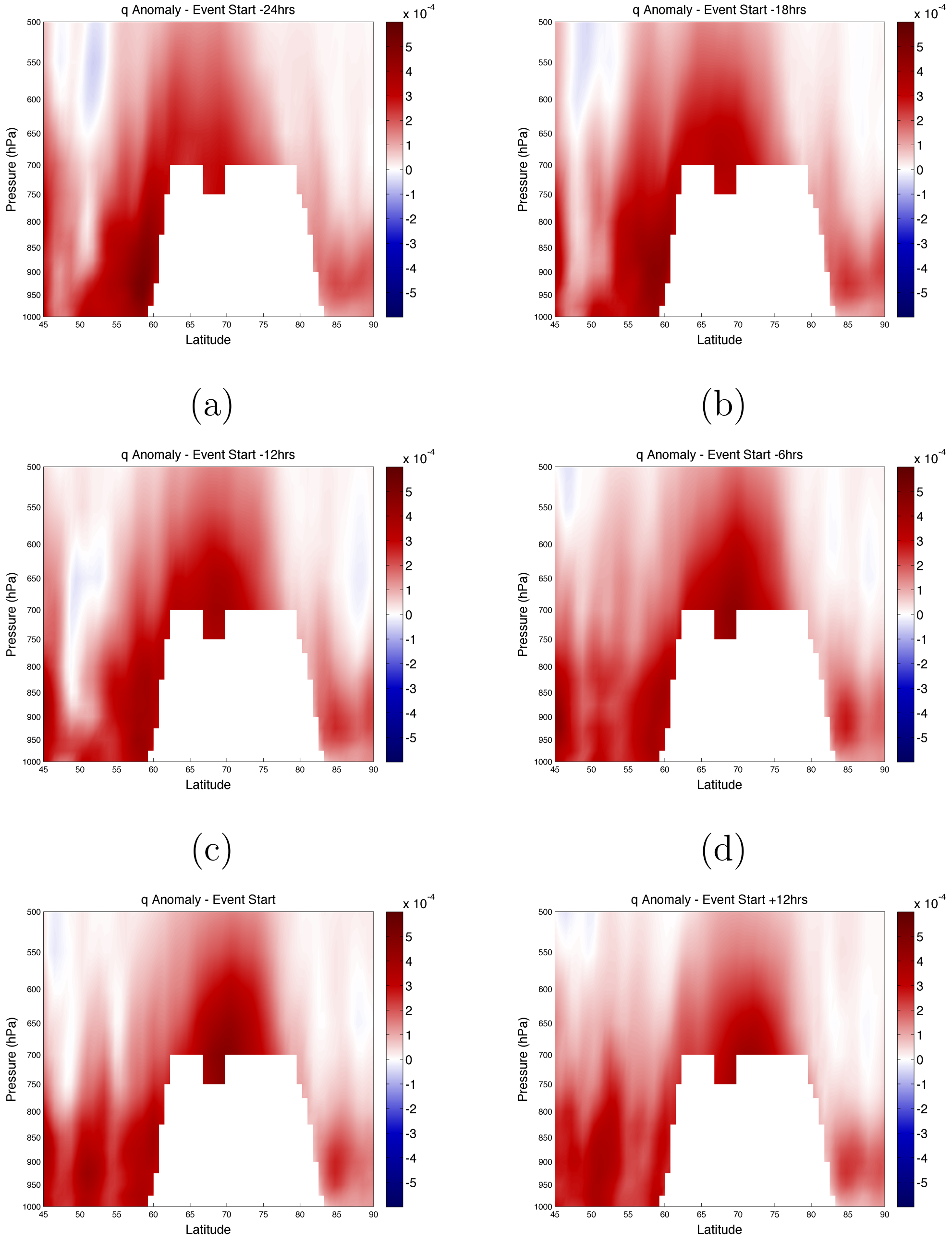

(a) (b)

(c) (d)

(e) (f)

Figure 4.20: Longitudinal cross-sections of specific humidity anomalies ($\frac{kg}{kg}$) (a) 24 hours, (b) 18 hours, (c) 12 hours, and (d) 6 hours prior to case start, (e) case start and (f) 12 hours after case start. Cross sections centered at 315°E (averaged from 314.25°E to 315.75°E).

In order to further investigate this in a quantitative manner, the Froude number (Fr) was calculated at atmospheric levels below the surface of the ice sheet as follows:

$$Fr = \frac{U}{NH} \tag{4.3}$$

where U is the magnitude of the wind at the analysis level, H is the height from the analysis level (i.e. the level of U) to Summit, and N is the Brunt-Vaisala frequency. N is calculated as follows:

$$N = \left(\frac{g}{\overline{\theta}} \frac{\partial \theta}{\partial z} \right)^{\frac{1}{2}} \tag{4.4}$$

where g is the acceleration due to gravity, $\overline{\theta}$ is the average potential temperature in the layer from the analysis level to Summit, and $\frac{\partial \theta}{\partial z}$ is the change in potential temperature with height in the layer. Fr is used to determine whether the kinetic energy is large enough to overcome the potential energy of a parcel to rise over a barrier (in the case of the work herein the barrier is the height of the ice sheet from the analysis level to Summit). IF $Fr > 1$ the flow will rise over the barrier unimpeded, while in cases where $Fr < 1$ the flow will be blocked by the barrier (Markowski and Richardson, 2011).

In order to evaluate Fr in the context of this thesis, Fr will only be calculated if the wind direction is within +/- 45°in the direction of Summit. It should be noted that this is an estimate of Fr, ideally, the wind used in the calculation would be the component of the wind in the direction of the terrain gradient. However, due to the presence of several local maxima in terrain height, the terrain gradient does not always point toward Summit despite its location at the highest point of the ice sheet. Additionally, in order to compare the effects of changes in wind speed and static stability, ERA data is interpolated to a constant height grid. This allows H to remain constant in the calculations thus U can be compared directly to NH with changes in the latter only due to variations in stability. Comparing U to NH allows for the comparison of the kinetic energy (kinetic energy is proportional to U) of parcels approaching the ice sheet to the stability of the atmosphere that parcels need to overcome in order to be lifted over the ice sheet. Changes in Fr can thus be attributed to either changes in dynamics, variations in atmospheric stability, or a combination of the two.

To provide a baseline for analysis of Fr in relation to LBC occurrence, an ICECAPS climatology of Fr was computed at 2750 m (Figure 4.21). This climatology covers the same time period as the liquid detection algorithm. The southwestern coast of Greenland experiences horizontal flow towards Summit the most often (Figure 4.21 (a)). This is expected given the climatological flow discussed in Section 4.2. The mean Fr over this area is close to 1 indicating that the flow may at times be capable of rising to the level of Summit. Along the rest of the coast, flow toward Summit is less frequent and Fr is under 1. Fr was also decomposed into the numerator and denominator for this climatology (Figure 4.21). The greatest magnitudes of U are found off the coast of the ice sheet. The smaller values of U closer to the ice sheet are likely due to increasing friction as the flow moves over the ice sheet itself. Conversely, the largest values of NH, indicating more stable atmospheric layers, are found over the ice sheet especially toward the north. This is likely due to enhanced radiative cooling of the ice surface relative to the ocean (N is inversely proportional to the mean potential temperature of the layer). There is a sharp gradient in Fr to the east of the ice sheet with larger values further offshore and relatively low values over the edge of the ice sheet itself. This is likely due to a combination of a cooler temperature profile (larger N) and a decrease in wind speed as it encounters the edge of the ice sheet.

At the start of LBC events, winds are more frequently in the direction of Summit along the entire edge of the terrain at 2750 m (Figure 4.22). Winds toward Summit are still most common along the southwestern coast of Greenland. This is consistent with the increased SW winds associated with the -NAO. In addition, Fr

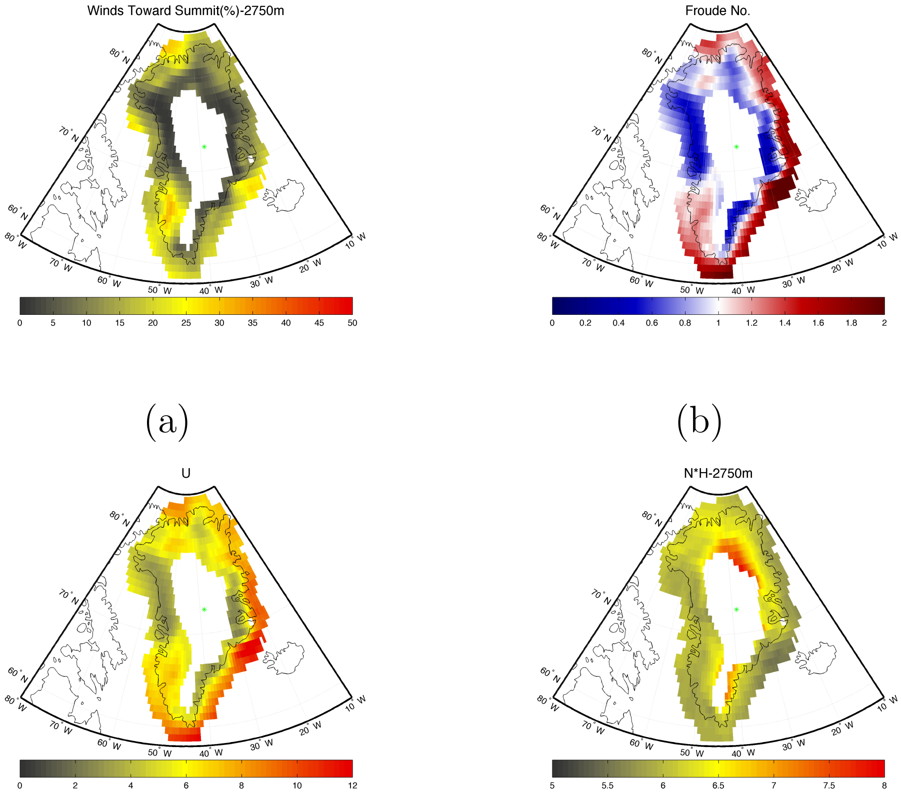

(a) (b)

(c) (d)

Figure 4.21: (a) Fraction of the ICECAPS period where the horizontal wind direction is within +/- 45°of Summit and the mean (b) Fr (unitless), (c) U ($\frac{m}{s}$), and (d) NH ($\frac{m}{s}$) at these times.

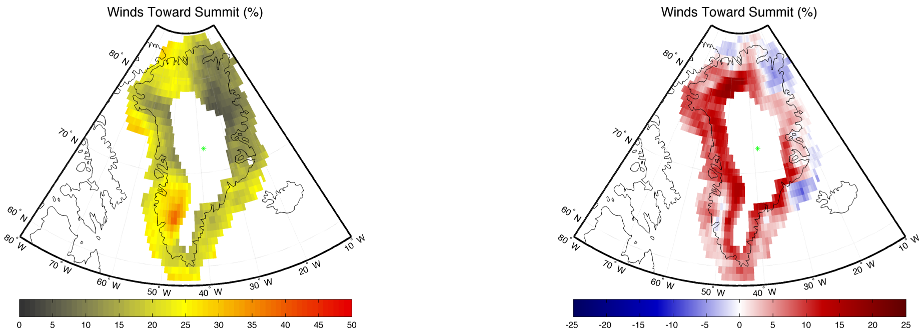

(a) (b)

Figure 4.22: (a) The fraction of LBC events where the horizontal wind direction is within +/- 45°of Summit at event start and (b) the difference between this and the climatology in Figure 4.21.

is increased along most of Greenland's terrain including across the southern portion of the ice sheet where flow toward Summit is most common (Figure 4.23 (a)). The statistical significance of these anomalies was tested using a two-tailed z-test. The increases in Fr along the ice sheet were nearly all found to be statistically significant at the 95 percent confidence level (Figure 4.23 (b)). Fr was also decomposed into U and NH in order to determine if either term was driving the changes noted. The horizontal wind magnitude along the southern portion of the ice sheet experienced statistically significant increases in a similar pattern to the full Froude number (Figure 4.23 (c-d)). In contrast, NH experienced very small magnitude changes across the domain, most of which were not statistically significant (Figure 4.23 (e-f)). This indicates that increases in the horizontal wind magnitude coupled with static stability values remaining close to climatology are responsible for the increases in Fr during LBC events. This indicates that air parcels approaching the ice sheet have more kinetic energy to rise through an atmosphere with close to climatological stability. Thus, it is more favorable for a parcel to reach the top of the ice sheet.

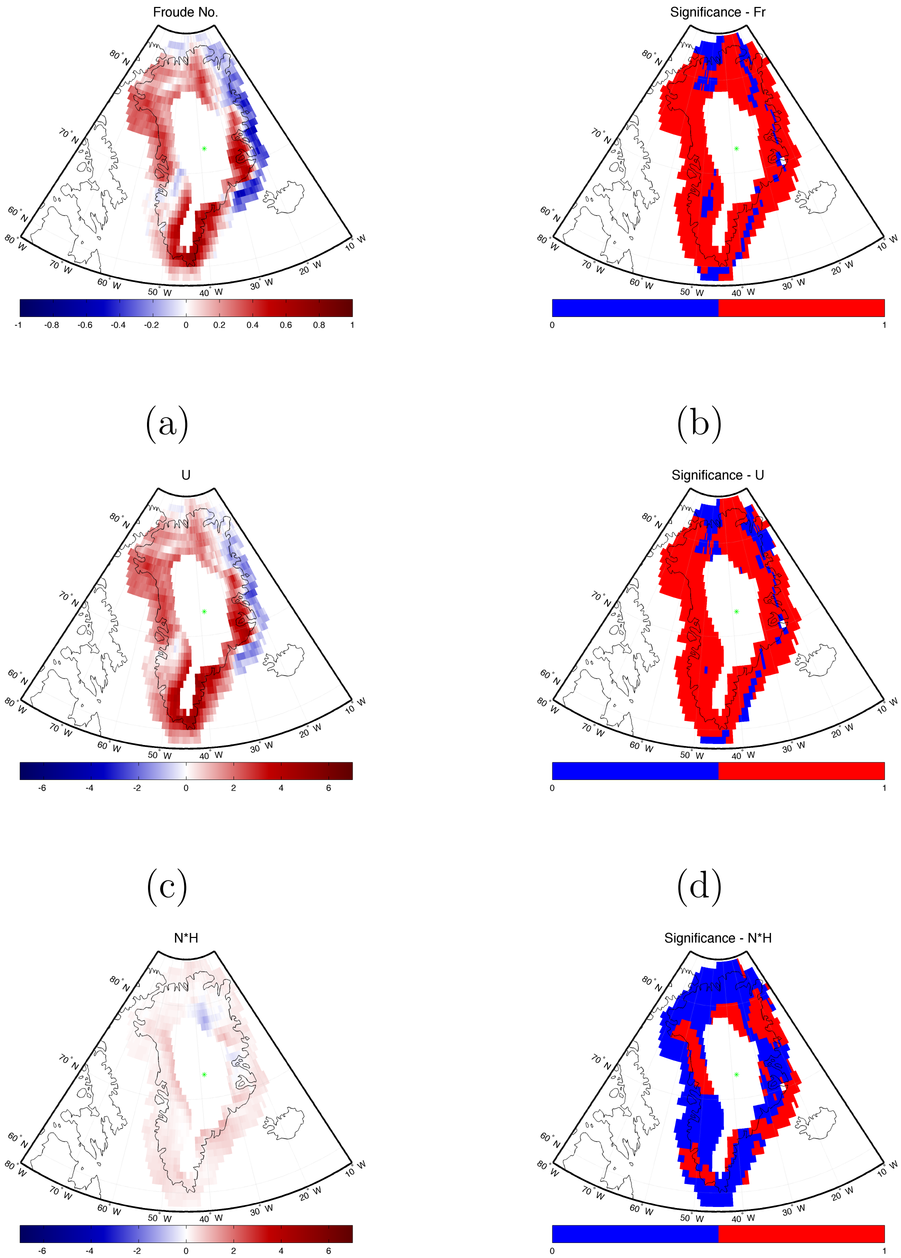

(a) (b)

(c) (d)

(e) (f)

Figure 4.23: Anomalies of (a) Fr (unitless), (c) U ($\frac{m}{s}$), and (e) NH ($\frac{m}{s}$) at the start of LBC events relative to the climatologies in Figure 4.21. Statistical significance of the anomalies shown in panels (b),(d), and (f) where red indicates significance at the 95 percent confidence level.

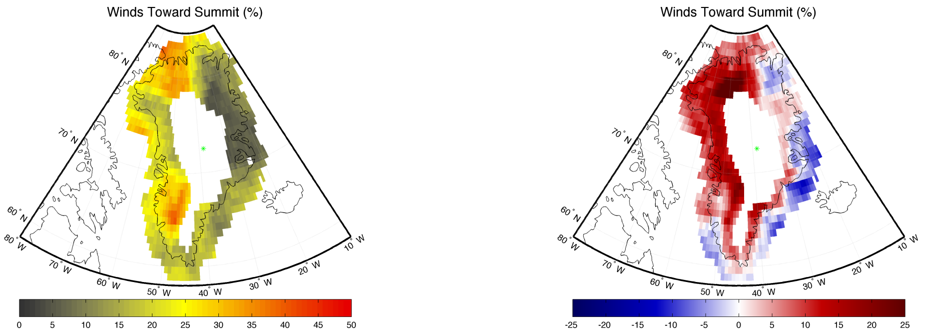

(a) (b)

Figure 4.24: Same as Figure 4.22 except for -NAO events.

For the -NAO events, winds toward Summit are increased primarily on the western side of the ice sheet as expected given the previous results and literature linking the -NAO to enhanced SW flow over the ice sheet (Figure 4.24). Again, the most common region for flow toward Summit is along the southwest coast. This region also experiences statistically significant increases in Fr and U while NH remains relatively close to climatology (Figure 4.25). The results for the -NAO events are very similar to the results for all LBC events due to the disproportionate amount of -NAO events.

The results for the +NAO events are markedly different. There are two regions where the winds are commonly in the direction of Summit: 1) along the southwest coast and 2) along the eastern coast of the ice sheet (Figure 4.26). These two regions are in agreement with the two flow patterns discussed in Section 4.2.1: 1) flow on the western edge of the trough which pushes further onshore during the +NAO and 2) wraparound flow from low pressure systems which track along the southeastern coast of Greenland which appears to be the more important pattern. Both Fr and U experience statistically significant increases in both of these regions (Figure 4.27 (a-d)). As before, there are no significant increases in NH indicating that changes in the dynamical setup are most important (Figure 4.27 (e-f)).

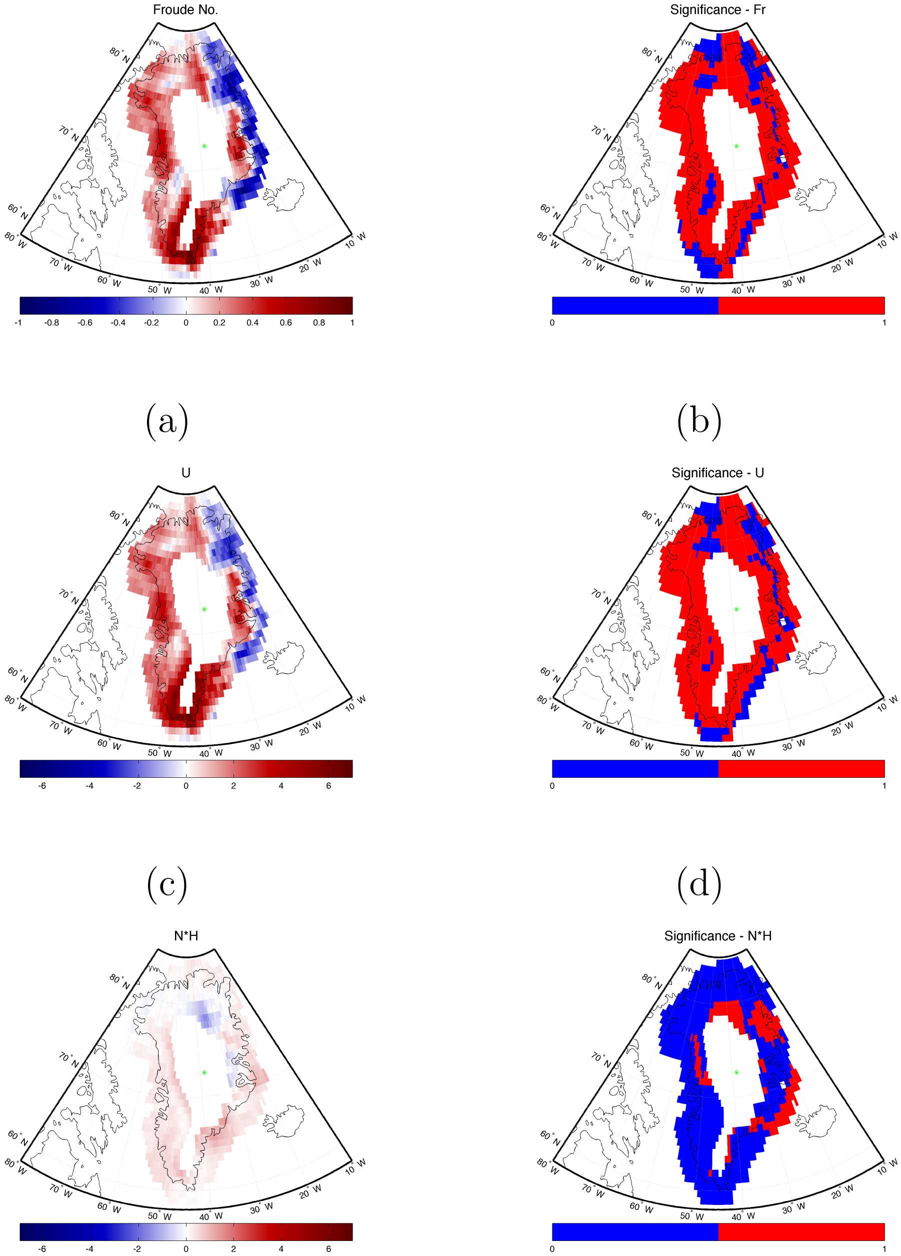

(a) (b)

(c) (d)

(e) (f)

Figure 4.25: Same as Figure 4.23 except for -NAO events.

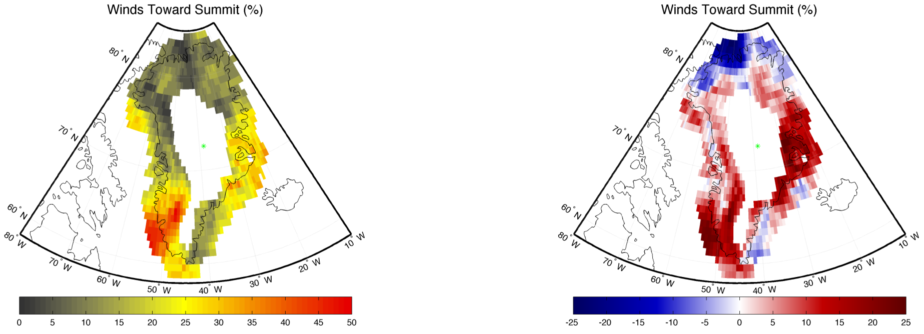

(a) (b)

Figure 4.26: Same as Figure 4.22 except for +NAO events.

HYSPLIT trajectories also indicate that parcels during LBC events are sourced from levels below Summit. The parcel source altitude is defined as the minimum height a parcel reaches between the initialization of the model and the source location of the parcel determined in Section 4.2.1. This is plotted in Figure 4.28 relative to the altitude of Summit in the model. Parcels are most commonly sourced from just less that 1 km below Summit and rarely (less than 10 events) from above the ice sheet (Figure 4.28 (c)). The results are consistent between phases of the NAO (Figure 4.28 (a-b)).

4.4 Summary

LBC events correspond to increases in atmospheric moisture content over the Greenland Ice Sheet. These increases are likely due to transport from off the ice sheet. Transport to the top of the ice sheet takes place via two predominate mechanisms related to the two phases of the NAO. First, southwesterly winds across the ice sheet either due to anomalously high pressure over the eastern coast of the ice sheet during the -NAO or, less frequently, from flow on the eastern side of a trough which pushes onto the western coast of the ice sheet during the +NAO

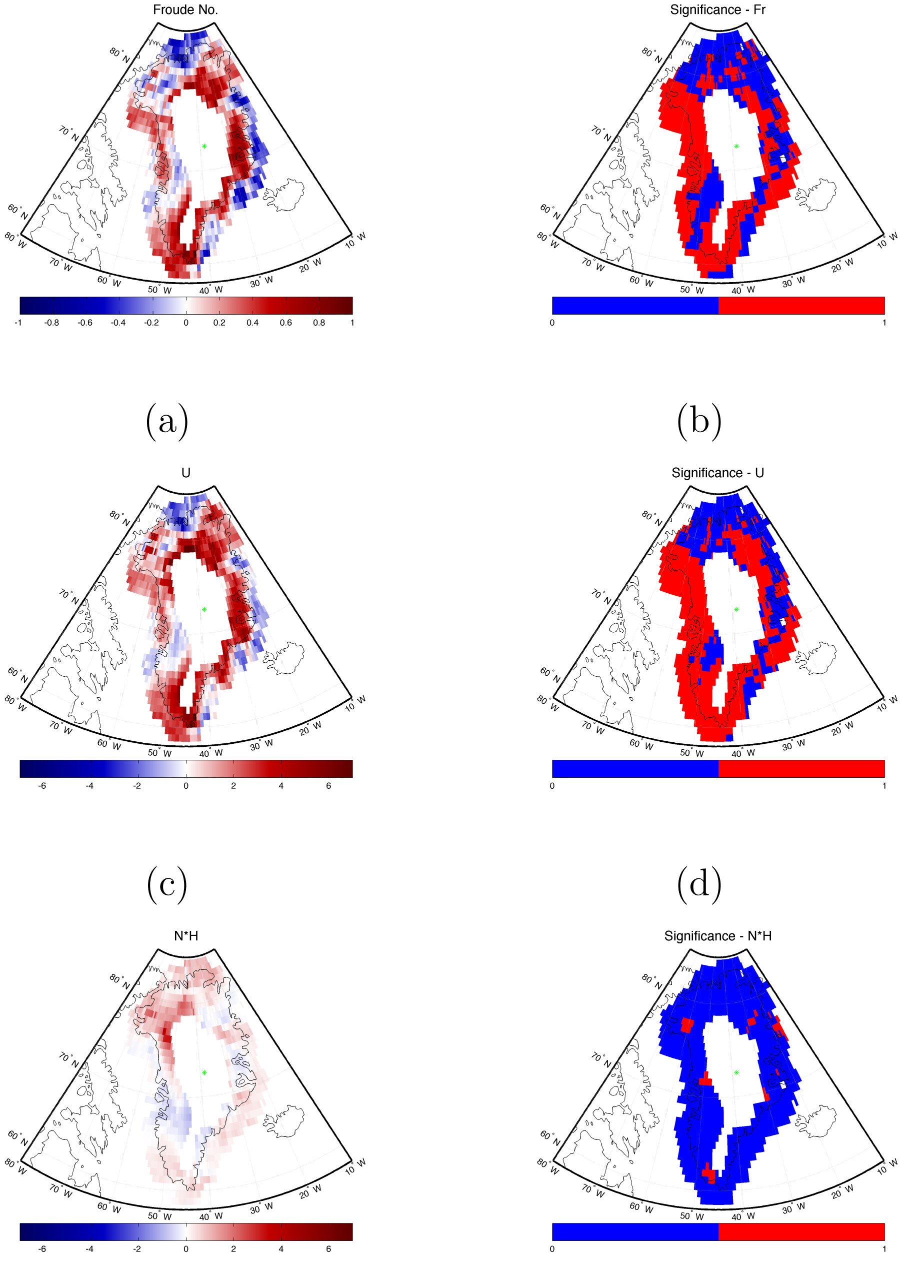

(a) (b)

(c) (d)

(e) (f)

Figure 4.27: Same as Figure 4.23 except for +NAO events.

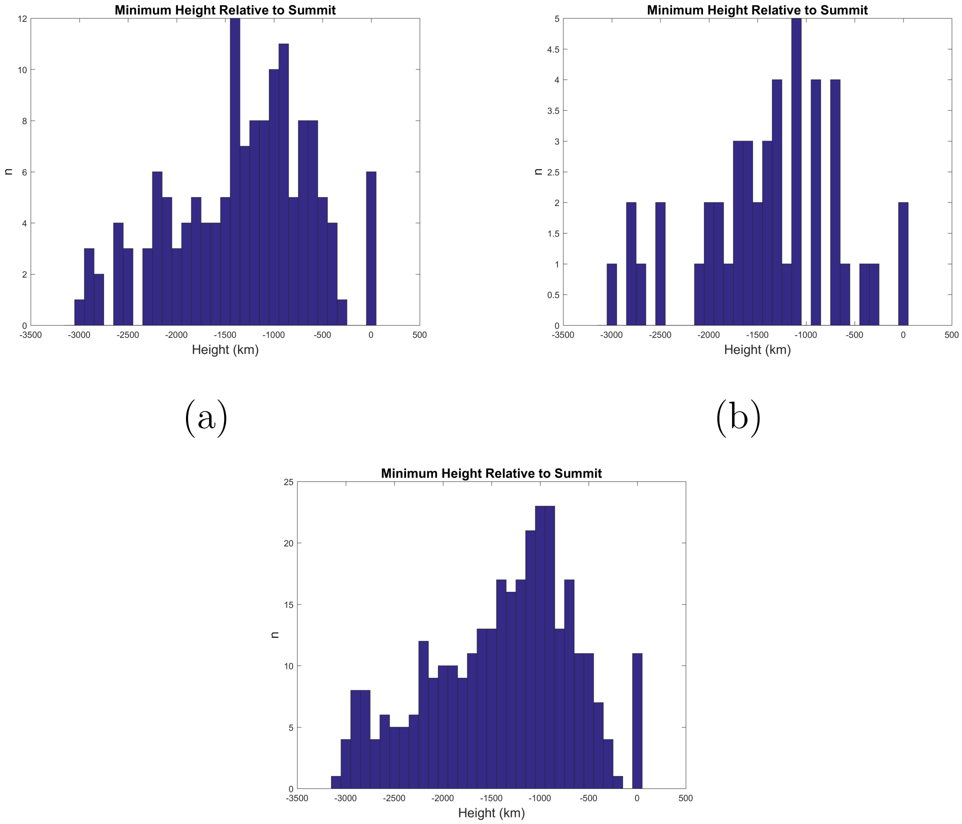

(a)

(b)

(c)

Figure 4.28: Histogram of the minimum height relative to Summit which parcels reach for (a) -NAO events, (b) +NAO events, and (c) all LBC events.

lead to flow over the GIS. Second, easterly wraparound flow associated with low pressure systems which track along the southeastern coast of the ice sheet during the +NAO leads to transport over the GIS. However, moisture transport over the ice sheet is not just related to constant level transport over the ice sheet. Analysis of the Froude number and HYSPLIT backward trajectories indicate that air parcels are more likely to rise from levels below the ice sheet during the occurrence of LBCs due to an increase in wind speed occurring in an environment with relatively close to climatological stability.

Chapter 5

Local Processes and Microphysical Cloud Properties

This chapter focuses on microphysical properties of LBCs and the processes which control their variability. This analysis will first determine how LBCs at Summit are characterized microphysically by analyzing mean precipitation, IWP, and LWP during cloud occurrence. Relationships between microphysical cloud properties and the large scale atmospheric setup will then be investigated to determine if the two predominate flow patters discussed in Chapter 4 are associated with different cloud properties. A summary of data availability relative to the 326 LBC events identified is presented in Table 5.1.

5.1 Precipitation

Precipitation is common during the occurrence of LBCs with only 10% of the events not having measurable precipitation as seen by the POSS (Figure 5.1 (a)). However, during each event precipitation was rarely constant throughout the event; 62% of LBC events experiencing some precipitation have precipitation fractions (defined as the fraction of measurements with a nonzero precipitation rate) less than 0.5 (Figure 5.1 (b)). Precipitation occurrence is also highly seasonal with

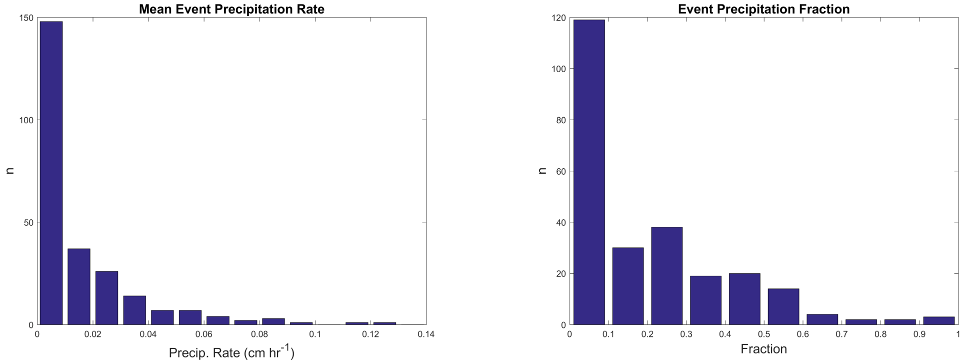

Mean Event Precipitation Rate

Event Precipitation Fraction

(a) (b)

Figure 5.1: Histograms of (a) the mean precipitation rate and (b) the precipitation fraction for each LBC event as measured by the POSS.

mean precipitation rate during LBC events peaking during the summer and reaching a minimum during the spring (Figure 5.2). Castellani et al. (2015) also found a similar seasonal variation in precipitation at Summit using the POSS and a cloud radar.

In order to determine the relative timing of precipitation during LBC events, an asymmetry parameter was computed as follows. An evenly spaced vector ranging from -1 to 1 was defined such that each precipitation observation corresponded to one value in the vector. The mean value of the vector was then computed only including points when the precipitation rate was greater than 0. So a value close to 1 (-1) indicates precipitation is occurring preferably at the end (start) of an event. For most LBC events, the asymmetry parameter is close to 0 (Figure 5.3). This indicates that precipitation is either occurring only during the middle of the event or approximately evenly throughout the event.

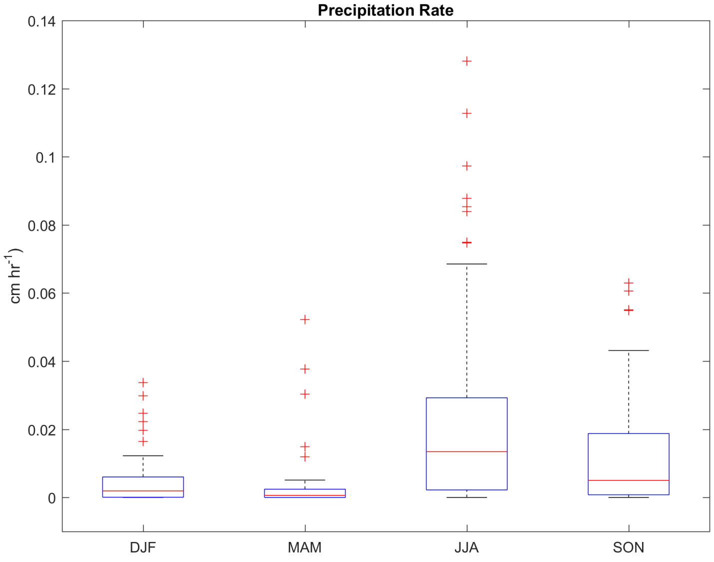

Figure 5.2: Box and whisker plot of seasonal mean precipitation rate during LBC events. The red line is the median, the box edges are the 25th and 75th percentiles, the whiskers are the most extreme values not considered outliers, and the red pluses are outliers.

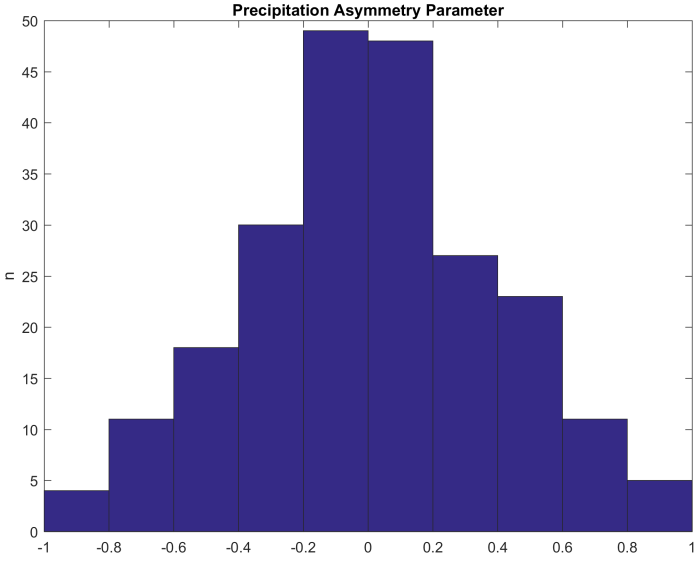

Figure 5.3: Histogram of the precipitation asymmetry parameter for LBC events.

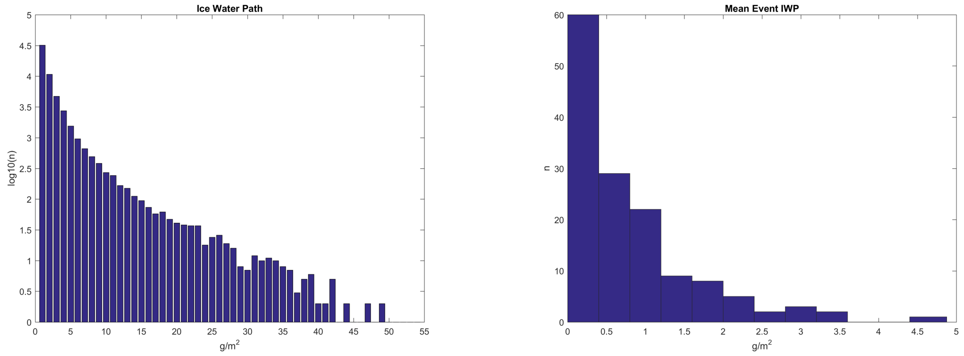

(a) (b)

Figure 5.4: Histograms of (a) all IWP observations during LBC events and (b) the mean IWP for each LBC event. Panel (a) is plotted using a log scale on the y-axis.

5.2 Ice Water Path

IWP is retrieved from the algorithm described by Shupe et al. (2015), referred to herein at ST microphysics. IWP is highly variable during the occurrence of LBCs observed at Summit. Mean values are often less than 1 $g\ m^{-2}$ although maximum values of IWP are over 50 $g\ m^{-2}$ (Figure 5.4). The observations of IWP at Summit are very similar to those observed in a field campaign in the Beaufort Sea (Pinto, 1998) although less than those observed during SHEBA (mean of 42 $g\ m^{-2}$ ranging from 0.1 to 200 $g\ m^{-2}$ (Shupe et al., 2006)). IWP is also highly seasonal at Summit exhibiting a similar seasonal variation in mean value as precipitation (Section 5.1) and LBC cloud occurrence (Section 4.1) with a maximum in the summer and minimum in the spring.

5.3 Liquid Water Path

The mean liquid water path during LBC events is 34 $g\ m^{-2}$, although this field is highly variable at Summit with the middle 50 percent of observations ranging from

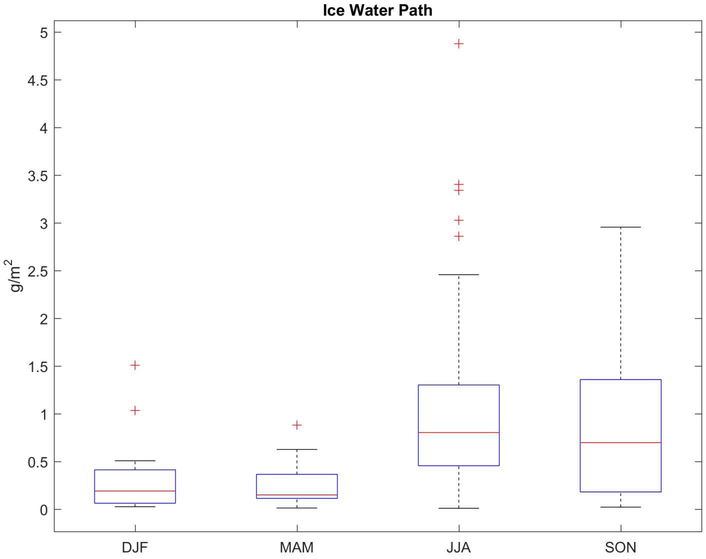

(a)

Figure 5.5: Box and whisker plots of seasonal mean IWP during LBC events. The red line is the median, the box edges are the 25th and 75th percentiles, the whiskers are the most extreme values not considered outliers, and the red pluses are outliers.

9 to 47 $g\ m^{-2}$ and a tail in the distribution peaking at over 800 $g\ m^{-2}$ (Figure 5.6). These results indicate that the LWP of LBCs at Summit is generally less than at Barrow (e.g. means of 106 $g\ m^{-2}$ and 156 $g\ m^{-2}$ found by de Boer et al. (2009) and Shupe et al. (2008)) and oceanic field campaigns (e.g. mean of 61 $g\ m^{-2}$ during SHEBA found by Shupe et al. (2006)). This is likely due to the lack of a local moisture source at Summit (Barrow is located on the northern coast of Alaska). Results from de Boer et al. (2009) at Eureka, however, were very similar with a mean LWP of 38 $g\ m^{-2}$. The largest difference between previous studies and the current results is the tail in the distribution. The maximum values of LWP at Summit are much larger than in the previous studies mentioned in this thesis. This is possibly due to the high temporal resolution of the retrieval at Summit (approximately 2 s) allowing for high frequency variations in LWP to be resolved. The few negative values of LWP (Figure 5.6 (a)) are likely due to errors in the value of the mass absorption coefficient for liquid water at the MWR channel frequencies or possibly errors in calibration of the instrument. When LWP is low, these errors can lead to the retrieval of negative values(Westwater et al., 2001; Gaussiat et al., 2007).

Bennartz et al. (2013) noted that the advection of a warm, moist airmasses coupled with LWP values between 10 $g\ m^{-2}$ and 40 $g\ m^{-2}$ was needed for surface melt at Summit. A cloud with this range of LWP values is optically thin enough to allow some solar radiation to pass through to the surface while simultaneously containing enough liquid water to effectively trap longwave radiation. 41 percent of all LWP observations during the presence of LBCs were within this range and 59 percent of LBC events had a mean LWP value within this range. If the advection of anomalous warm airmasses to the top of the ice sheet becomes more common as the climate warms, melt events could occur more frequently due to the common occurrence of LBCs containing between 10 $g\ m^{-2}$ and 40 $g\ m^{-2}$ of liquid water.

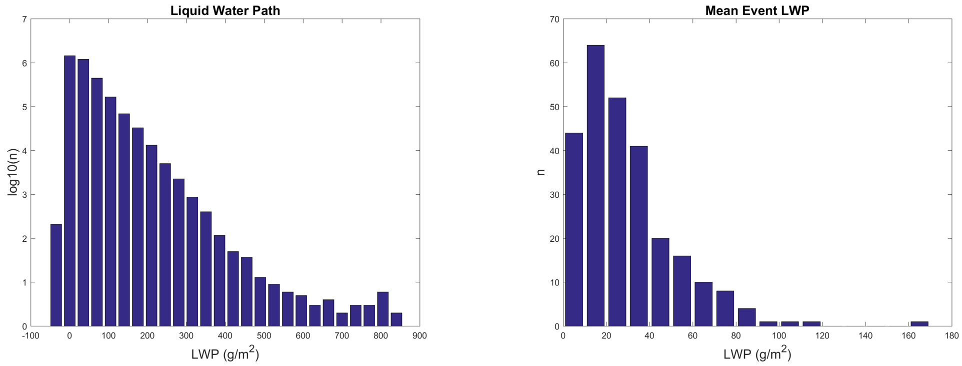

(a) (b)

Figure 5.6: Histograms of (a) all LWP observations during LBC events and (b) the mean LWP for each LBC event. Panel (a) is plotted using a log scale on the y-axis.

However, it should be noted that this could be offset if LWP increases enough to be consistently above 40 $g\ m^{-2}$ due to the higher temperatures.

In order to further investigate the result from Bennartz et al. (2013), data from the surface meteorology station at Summit was used to track near surface temperature changes during LBC events. Temperature change was calculated when the LWP either stayed below 10 $g\ m^{-2}$, within 10 and 40 $g\ m^{-2}$, or above 40 $g\ m^{-2}$ for a minimum of twenty minutes. In order to prevent very short term variations of LWP from affecting this calculation, a 2 minute running mean was applied to the data (Figure 5.7). In addition, since the hypothesis from Bennartz et al. (2013) depends on both longwave and shortwave radiation impinging on the surface, temperature change was only calculated if the minimum solar elevation angle over the period was greater than 0. To show this calculation graphically, a single LBC event is shown below as an example (Figure 5.7). For this event, five periods where the LWP remained within one of the specified ranges for at least twenty minutes were identified (Figure 5.7 (b)). Example calculations for these five periods are shown in Figure 5.8. When this methodology is applied to the

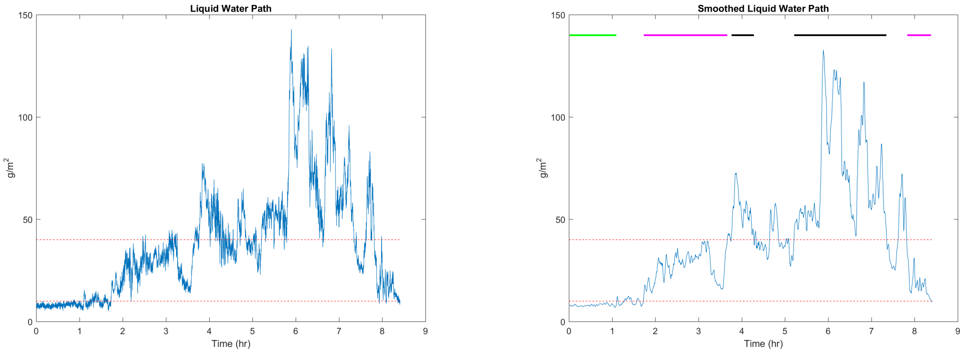

(a) (b)

Figure 5.7: Time series of (a) LWP and (b) LWP smoothed with a two minute running mean. Dashed red lines indicate LWP values of 10 and 40 $g\ m^{-2}$. Solid bars represent time periods where the LWP remained below 10 $g\ m^{-2}$ (green), within 10 and 40 $g\ m^{-2}$ (magenta), and above 40 $g\ m^{-2}$ (black) for at least 20 minutes.

entire dataset, 547 periods where the LWP remained below 10 $g\ m^{-2}$, 944 periods where the LWP remained between 10 and 40 $g\ m^{-2}$, and 586 periods where the LWP remained above 40 $g\ m^{-2}$ were identified. Histograms of the temperature change during these periods yield a large spread with both positive and negative temperature changes found quite frequently for each range of LWP (Figure 5.9). This is likely due to the effects of processes not accounted for in this analysis such as sublimation of precipitation if the surface is not saturated and temperature advection. However, even with this large spread in each distribution, there are still large differences between the three distributions. When LWP remains below 10 $g\ m^{-2}$, negative near surface temperature change is most common (Figure 5.9 (a)) likely due to effective radiative cooling of the surface since there is not enough liquid water to trap outgoing radiation. The opposite is true for periods where the LWP is between 10 and 40 $g\ m^{-2}$ and for periods where LWP remains above 40 $g\ m^{-2}$ (Figure 5.9 (b-c)). However it should be noted that these two

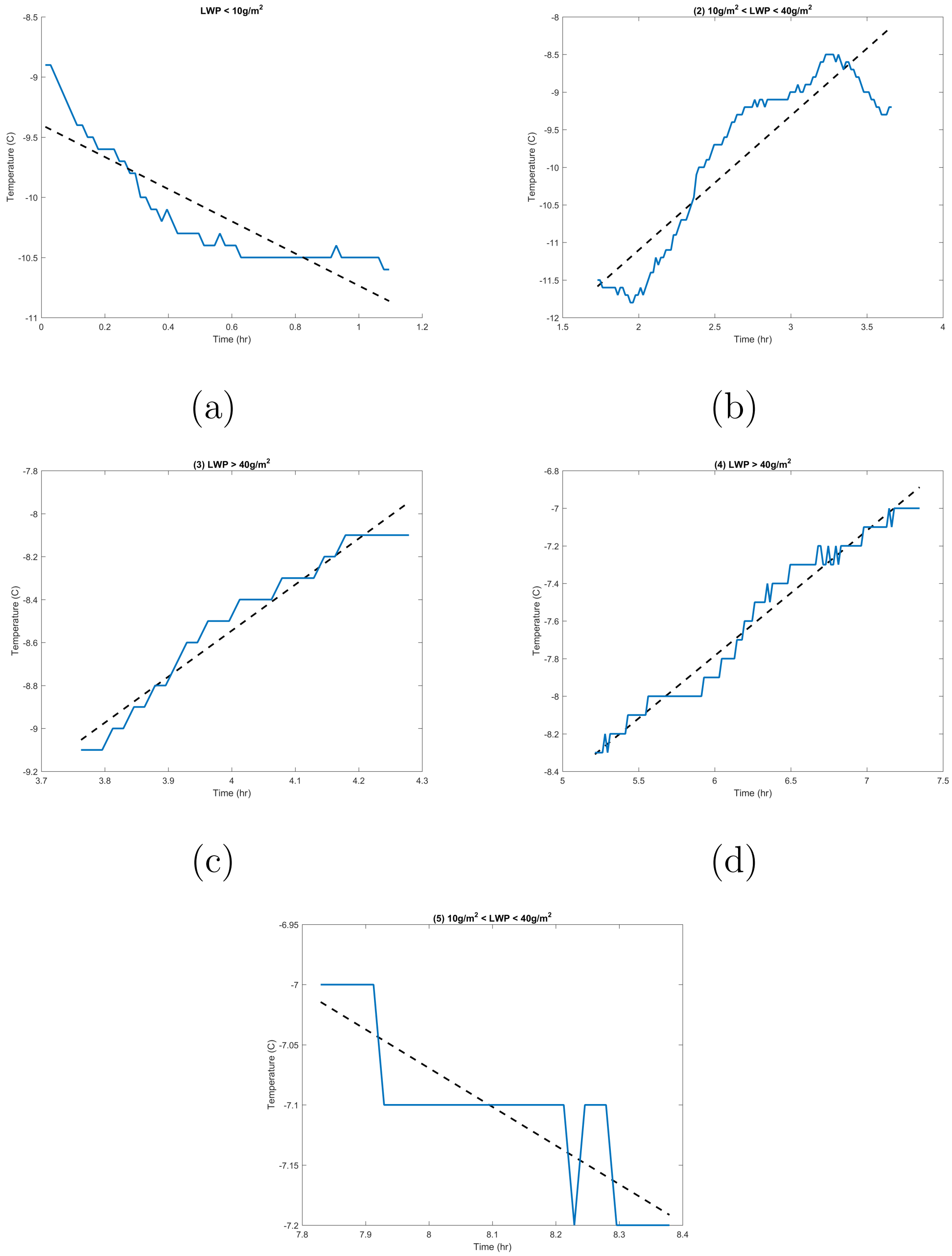

(a)

(b)

(c)

(d)

(e)

Figure 5.8: Time series of 2 m air temperature (blue) during the periods identified in Figure 5.7. Black dashed lines are linear fits to the 2 m temperature where the slope represents temperature change in degrees per hour. Slopes are (from a-e): -1.34, 1.79, 2.14, 0.67, and -0.32 degrees C per hour.

distributions have a large difference - when the LWP is between 10 and 40 $g\ m^{-2}$ the tail towards more positive values of temperature change is larger while the distribution for LWP remaining greater than 40 $g\ m^{-2}$ is more strongly peaked around 0. Temperature changes of greater than 1°C per hour are found nearly twice as frequently when the LWP remains within 10 and 40 $g\ m^{-2}$ (19.7 percent as opposed to 10.4 percent when LWP is above 40 $g\ m^{-2}$ and 8.4 percent when LWP is below 10 $g\ m^{-2}$). While not occurring a majority of the time, positive near surface temperature changes are most common when the LWP remains in the bounds found by Bennartz et al. (2013). Conversely, temperature trends of less than -1°C are observed in 2.2 percent of periods where LWP is greater than 40 $g\ m^{-2}$, 7.2 percent of the periods where LWP remains between 10 and 40 $g\ m^{-2}$, and 34.9 percent of the periods where the LWP remained below 10 $g\ m^{-2}$.

Given the importance of the effects that LBCs have on the surface as well as the analysis above and results found by Bennartz et al. (2013), it is of interest to explore what factors control the variability of LWP both during individual LBC events and between separate events. Similarly to precipitation and IWP, LWP exhibits strong seasonal dependence with a maximum in both occurring during the summer and a minimum during the spring (Figure 5.10). This is likely due, in part, to a greater amount of evaporation occurring over the oceans due to warmer temperatures during the summer. Retrievals of PWV lend evidence to this, indicating that the air above Summit is more moist during the summer (Figure 5.10 (b)). However, it should be noted that this is not the only factor playing a role in the seasonal cycle of LWP since the minimum in PWV occurs during the winter while the minimum in LWP occurs during the spring.

Another factor which potentially affects LWP is the solar elevation angle, which can change significantly over the course of a LBC event (depending on the length of the event), as long as it does not occur in winter when the sun does not rise

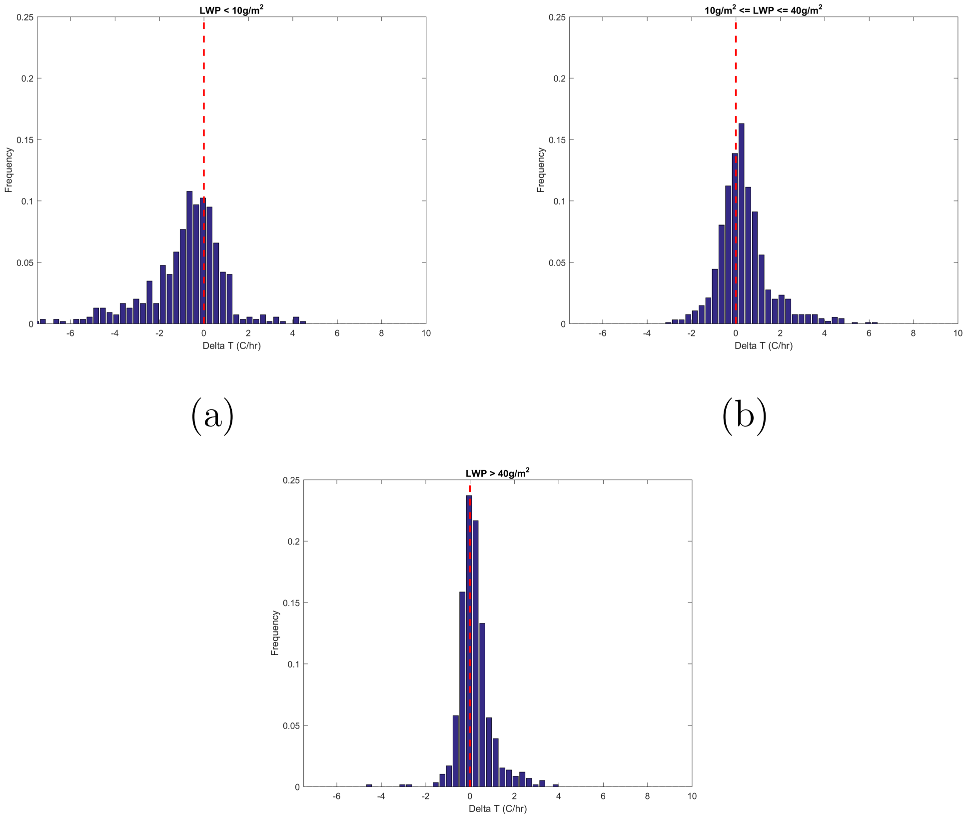

(a)

(b)

(c)

Figure 5.9: Histograms of 2m temperature change when the LWP (a) remains below 10 $g\ m^{-2}$, (b) remains between 10 and 40 $g\ m^{-2}$, and (c) remains above 40 $g\ m^{-2}$ for a minimum of 20 minutes. The red dashed line indicates a temperature change of 0.

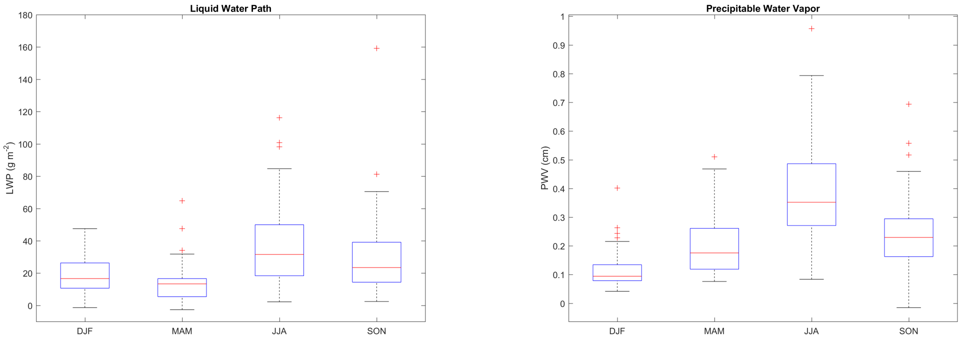

(a) (b)

Figure 5.10: Box and whisker plots of seasonal mean (a) LWP and (b) PWV during LWP events. The red line is the median, the box edges are the 25th and 75th percentiles, the whiskers are the most extreme values not considered outliers, and the red pluses are outliers.

at Summit (Figure 5.11). Since liquid layers in Arctic clouds are likely, in part, maintained by turbulence generated by cloud top radiative cooling (Morrison et al., 2012), heating from solar radiation absorbed by the clouds could potentially mitigate the effect of this radiative cooling thus decreasing the intensity of the turbulence leading to less condensation. This absorption could also lead to evaporation of already existing liquid droplets. In order to remove variability between events, which is likely dominated by the amount of atmospheric moisture available, LWP for each event was normalized by subtracting the mean and dividing by the standard devation of LWP for that event. The mean standardized LWP was then computed for different solar elevation angles (Figure 5.12 (a)). For solar elevation angles less than 10 degrees the mean was positive, while for angles greater than 10 the mean was negative. This indicates that as the solar elevation angle increases during a LBC event the amount of liquid in the cloud is more likely to decrease. This makes physical sense when considering the path which radiation takes relative to the cloud. Consider the following two examples of radiation being scattered

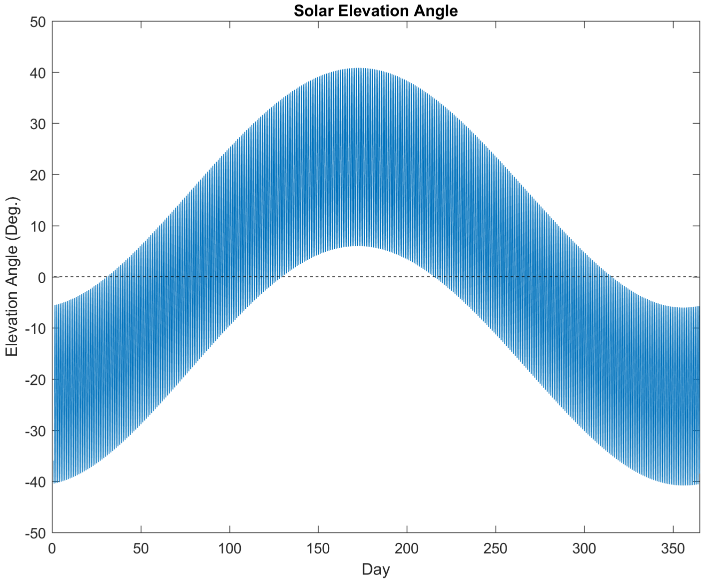

Figure 5.11: Annual cycle of the solar elevation angle at Summit, Greenland.

within a cloud. First, if the elevation angle is very steep (near 0) and radiation is scattered after traveling a distance, s, through the cloud there is a high likelihood that the radiation is scattered away from the cloud since the beam did not have a chance to penetrate deep into the cloud and the scattering of solar radiation in a liquid cloud will be primarily in the forward direction (the beam is essentially skimming along the cloud top). However, if the elevation angle is increased and, as before, the radiation travels a path length of s before being scattered, the scattered beam is now relatively deep within the cloud and thus has a greater chance to be absorbed within the cloud at a later time. It is much more difficult for the beam to scatter back up to the top of the cloud since, as stated before, scattering will be primarily in the forward direction. Thus, absorption is more effective at relatively high solar elevation angles and the LWP is decreased. It should be noted that, while physically valid, this process does not appear to be a dominant driver of LWP variability. The variability of LWP is high while the difference in LWP for varying solar elevation angles is quite low.

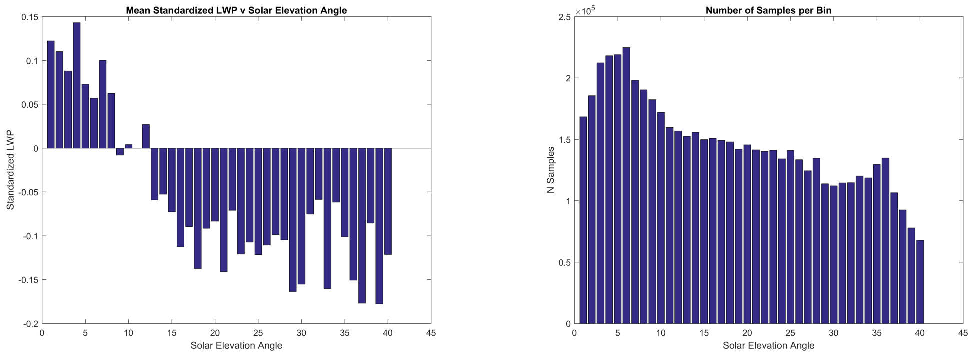

(a) (b)

Figure 5.12: Mean standardized LWP for solar elevation angles ranging from 1 to 40 degrees (a) and the number of samples in each solar elevation angle bin (b).

5.4 Connections to the Large Scale Atmosphere

Given the relationship between the occurrence of LBCs and the differing large scale atmospheric setups corresponding to the two phases of the NAO discussed in Chapter 4, it of interest to explore potential links between the microphysical properties of LBCs and the large-scale atmospheric setup. The prevailing large scale flow pattern has been shown to influence precipitation over the exterior of the ice sheet (recall Section 2.4.3). Specifically, orographic lift from onshore flow over the southeastern coast of the ice sheet causes heavier precipitation than onshore flow over the southwestern coast due to the steeper slope of the eastern ice sheet (Schuenemann and Cassano, 2009). The analysis from Schuenemann and Cassano (2009) focused on the exterior of the ice sheet since this is where most of Greenland's precipitation occurs. Thus, it is of interest to explore the relationship between precipitation (as well as other microphysical properties of LBCs) and the prevailing flow pattern to determine whether the effect of the steeper rise of the ice sheet to the east has any effects further inland.

In order to determine if there are relationships between the large-scale flow and cloud microphysical properties, correlations were performed between different mean microphysical properties and the NAO index and source latitude and longitude from HYSPLIT trajectories (Table 5.2). Statistically significant negative correlations were found between both the HYSPLIT source longitude and NAO index with mean event LWP and PWV. This indicates that LWP and PWV are lower during the positive phase of the NAO and when the source longitude from HYSPLIT is higher (i.e. parcels sourced from further east). This is consistent with the results of Schuenemann et al. (2009), which indicated that when cyclones cause orographic lift along the steep southeastern coast of Greenland precipitation is heavier than when the flow is over the less steep southwestern coast. The correlations indicate that the atmosphere is losing more of its moisture as air parcels move toward Summit if they are sourced from over the steepest portion of the ice sheet. However it should be noted that this correlation, while statistically significant, is small, so the large-scale setup is not a dominant factor contributing to the variability LWP during LBC events. More atmospheric moisture would also intuitively lead to higher values of IWP as well, however, that is not the case for this analysis. This could possibly be due to the lower sample size of the IWP dataset (Table 5.1). No relationship was found between the large scale atmospheric setup and precipitation rate indicating that the variations in Greenland precipitation discussed by Schuenemann et al. (2009) are confined to the edge of the ice sheet as parcels are lifted over the steep terrain. This is consistent with the results of Castellani et al. (2015) indicating that while precipitation at Summit is more common when winds have southerly component, there is no preference for an easterly or westerly component.

Instrument/Dataset	Number of Cases	Percent
MWRs	265	81%
ST Microphysics	141	43%
POSS	251	77%
Surface Met.	301	92%

Table 5.1: Number of cases for which each instrument/dataset is available.

Large-scale Property	Microphysical Property	Correlation (p-value)
HYSPLIT Source Latitude	LWP	-0.0366 (0.5533)
HYSPLIT Source Longitude	LWP	**-0.1222 (0.0468)**
NAO Index	LWP	**-0.2079 (.0007)**
HYSPLIT Source Latitude	IWP	-0.1015 (0.2308)
HYSPLIT Source Longitude	IWP	-0.1014 (0.2313)
NAO Index	IWP	-0.0667 (0.4321)
HYSPLIT Source Latitude	PWV	-0.0514 (0.4044)
HYSPLIT Source Longitude	PWV	**-0.1606 (0.0088)**
NAO Index	PWV	**-0.2596 (.00002)**
HYSPLIT Source Latitude	POSS Precip. Rate	-0.0202 (0.7505)
HYSPLIT Source Longitude	POSS Precip. Rate	-0.0280 (0.6594)
NAO Index	POSS Precip. Rate	-0.1097 (0.0830)

Table 5.2: Summary of correlations (using Pearson's linear correlation coefficients) between microphysical cloud properties and large-scale atmospheric patterns. Statistically significant ($p < 0.05$) correlations are in bold.

Chapter 6

Conclusions

6.1 Summary

Arctic LBCs have been observed at multiple locations and can have a large impact on the Arctic surface and boundary layer (e.g. Bennartz et al., 2013; Curry et al., 1996; Shupe, 2011). Thus, understanding their occurrence and properties across the Arctic is important. The motivation behind the work presented herein is to better understand the occurrence and properties of LBCs over Summit, Greenland. Clouds at Summit have received relatively little study thus far in part due to the remote location.

Through the ICECAPS project, over 6 years of observations of tropospheric and cloud properties at Summit, Greenland are now available. A cloud phase detection algorithm was applied to these data yielding 326 cloud events containing liquid water for at least six hours. Both their occurrence and microphysical properties are highly seasonal with the maximum (minimum) number of events, event mean LWP, IWP, and precipitation rate occurring in the summer (spring). This seasonal cycle of occurrence is similar to that found in previous studies, although the maximum in occurrence at other Arctic locations can vary from summer to fall (Shupe, 2011). The seasonal cycle of precipitation rate is consistent with that found by Castellani et al. (2015). The occurrence of LBCs over Summit corresponds to increases in atmospheric temperature and moisture over the ice sheet. The positive moisture anomalies are strongest over the central portion of the ice sheet leading to positive relative humidity anomalies restricted to the central GIS. The LL subset of events are characterized by more persistent moisture anomalies over the ice sheet.

Cloud base heights below 1 km are common, consistent with previous research (e.g. de Boer et al., 2009; Shupe, 2011). Mean LWP and IWP values observed during the occurrence of LBCs at Summit are smaller than those observed at coastal locations and over the ocean during field campaigns (Shupe et al., 2006; de Boer et al., 2009; Shupe et al., 2008). Precipitation is found to be common, but often sporadic, during LBC events.

Summit is located at approximately 72°N, 3.2 km in elevation above sea level, and at the center of the GIS and, thus, does not have any local sources of atmospheric moisture. The moisture anomalies present during the occurrence of LBCs are related to two predominate flow patterns which correspond to the two phases of the NAO. During LBCs occurring in the negative phase, strong ridging centered over the GIS leads to southwesterly flow over the ice sheet extending from the southwest coast toward Summit. This southwesterly flow during the negative phase has been well documented (e.g. Mosley-Thompson et al., 2005). During LBCs occurring in the positive phase, cyclones in the North Atlantic pass close to the GIS. Specifically, those cyclones passing between Greenland and Iceland correspond to the occurrence of LBCs during the positive phase. During these events, flow wrapping around the cyclones leads to southeasterly winds extending from the east/southeast to Summit. Cyclones in this region have previously been linked to precipitation along the southeast coast of the ice sheet (Schuenemann and Cassano, 2009; Schuenemann et al., 2009). These two flow patterns not only exist at elevations above that of Summit, but lower in the troposphere as well. This leads to interactions with the steep terrain at the edge of the ice sheet. The variability of Greenland's climate has been shown to be strongly influenced by topography (Steffen and Box, 2001; Ohmura and Reeh, 1991). Orographic lift generated by flow directed into this terrain allows air parcels from below the elevation of Summit to rise to the top of the ice sheet. This process has been linked to precipitation occurrence along the edge of the ice sheet (Schuenemann et al., 2009). Orographic lift from lower levels is more favored during the occurrence of LBCs due to increases in wind speed coupled with negligible variations in atmospheric stability. This analysis indicates air parcels reaching Summit during the occurrence of LBCs originate from over the Atlantic Ocean, predominately south of Summit, and from lower elevations than Summit which are all more moist environments.

Microphysical properties of LBCs do not strongly relate to the large-scale atmospheric setup. LWP and PWV are higher when the NAO index is negative (flow is from the southwest), but this is not a strong relationship. IWP, precipitation rate, and precipitation timing were found to have no relationship with the large-scale atmospheric pattern during cloud occurrence.

Analysis of LWP during LBC events indicates that values between 10 and 40 $g\ m^{-2}$ are common. Bennartz et al. (2013) showed that this range of LWP is a key condition for surface melt at Summit. The analysis in this thesis showed that positive 2 meter temperature changes are more common during LBCs when the LWP is within this range. In addition to the seasonal variations and relationship with the large-scale atmospheric flow, LWP is found to vary weakly with solar elevation angle with larger values occurring when the solar elevation angle is smaller.

6.2 Future Work

The analysis presented here could be expanded to an inter-comparison with other Arctic sites, such as Barrow and Eureka, as well as to datasets obtained from relatively short term field campaigns such as SHEBA. There has been a lot of research consisting of analysis of Arctic clouds at single locations, but a relative lack of studies comparing different locations. The potential future research directions discussed below could all be considered in the context of an inter-comparison.

Given the importance of LBCs on the surface at Summit discussed here and by Bennartz et al. (2013), further analysis of their effect on the Arctic surface and boundary layer is warranted. Is there a difference between clouds containing pure liquid layer(s) and those consisting of mixed phase layer(s)? Does the relationship between LBCs and the lower atmosphere change when considering single layer events only? How do LBCs with varying microphysical properties affect the lower atmosphere in other Arctic locations? A more complete picture of how Arctic clouds affect the lower atmosphere and surface is necessary in order to understand how large of a role they might play in surface melting.

A further analysis of cloud microphysical properties and their relation to the occurrence and longevity of LBCs over Summit is also needed. This thesis focused primarily on the large-scale atmospheric patterns corresponding to the occurrence of LBCs and the mean microphysical properties of these clouds. Since microphysical properties were not found to strongly relate to the large-scale setup, it is of interest to further explore what factors drive the variations of microphysical cloud properties at Summit. In particular, the factors controlling precipitation variability need to be further explored since this field is highly variable and important when considering GIS mass balance.

Using numerical modeling in addition to observations would likely be useful in answering the above questions due to the ability to control and change different atmospheric and cloud properties in order to explicitly investigate the above questions in a more controlled environment. This would be a particularly useful addition for studying the effects of LBCs on the surface. One complicating factor to the analysis of near surface temperature change presented in Chapter 5 was the many (potentially competing) processes which were affecting the surface. Using numerical modeling would allow for simulation of the Arctic near surface and boundary layer environments under a variety of cloud properties (e.g. with/without precipitation, mixed-phase and liquid clouds, different values of cloud LWP and height) and background conditions (e.g. with/without temperature advection, different seasons).

Bibliography

Arrehnius, S., 1896: On the influence of carbonic acid in the air upon the temperature of the ground. *Philosophical Magazine and Journal of Science*, **41**, 237–277.

Barnston, A. G., and R. E. Livezey, 1987: Classification, seasonality and persistence of low-frequency atmospheric circulation patterns. *Monthly weather review*, **115 (6)**, 1083–1126.

Belleflamme, A., X. Fettweis, and M. Erpicum, 2015: Recent summer arctic atmospheric circulation anomalies in a historical perspective. *Cryosphere (The)*, **9**, 53–64.

Bennartz, R., and Coauthors, 2013: July 2012 greenland melt extent enhanced by low-level liquid clouds. *Nature*, **496 (7443)**, 83–86.

Bintanja, R., E. van der Linden, and W. Hazeleger, 2012: Boundary layer stability and arctic climate change: a feedback study using ec-earth. *Climate dynamics*, **39 (11)**, 2659–2673.

Boisvert, L., and J. Stroeve, 2015: The arctic is becoming warmer and wetter as revealed by the atmospheric infrared sounder. *Geophysical Research Letters*, **42 (11)**, 4439–4446.

Boisvert, L., D. Wu, and C.-L. Shie, 2015: Increasing evaporation amounts seen in the arctic between 2003 and 2013 from airs data. *Journal of Geophysical Research: Atmospheres*, **120 (14)**, 6865–6881.

Box, J. E., and K. Steffen, 2001: Sublimation on the greenland ice sheet from automated weather station observations. *Journal of Geophysical Research: Atmospheres*, **106 (D24)**, 33 965–33 981.

Bromwich, D. H., Q.-s. Chen, Y. Li, and R. I. Cullather, 1999: Precipitation over greenland and its relation to the north atlantic oscillation. *Journal of Geophysical Research: Atmospheres*, **104 (D18)**, 22 103–22 115.

Brown, S. T., S. Desai, W. Lu, and A. Tanner, 2007: On the long-term stability of microwave radiometers using noise diodes for calibration. *IEEE transactions on geoscience and remote sensing*, **45 (7)**, 1908–1920.

Buis, A., and S. Cole, 2012: Satellites see unprecedented greenland ice sheet melt. NASA - JPL.

Cadeddu, M., J. Liljegren, and D. Turner, 2013: The atmospheric radiation measurement (arm) program network of microwave radiometers: Instrumentation, data, and retrievals. *Atmospheric Measurement Techniques*, **6 (9)**, 2359–2372.

Calder, C. A., P. F. Craigmile, and E. Mosley-Thompson, 2008: Spatial variation in the influence of the north atlantic oscillation on precipitation across greenland. *Journal of Geophysical Research: Atmospheres*, **113 (D6)**.

Campbell, J. R., D. L. Hlavka, E. J. Welton, C. J. Flynn, D. D. Turner, J. D. Spinhirne, V. S. Scott III, and I. Hwang, 2002: Full-time, eye-safe cloud and aerosol lidar observation at atmospheric radiation measurement program sites: Instruments and data processing. *Journal of Atmospheric and Oceanic Technology*, **19 (4)**, 431–442.

Castellani, B. B., M. D. Shupe, D. R. Hudak, and B. E. Sheppard, 2015: The annual cycle of snowfall at summit, greenland. *Journal of Geophysical Research: Atmospheres*, **120 (13)**, 6654–6668.

Curry, J., 1983: On the formation of continental polar air. *Journal of the Atmospheric Sciences*, **40 (9)**, 2278–2292.

Curry, J., and G. Herman, 1985a: Relationships between large-scale heat and moisture budgets and the occurrence of arctic stratus clouds. *Monthly weather review*, **113 (9)**, 1441–1457.

Curry, J., J. Pinto, T. Benner, and M. Tschudi, 1997: Evolution of the cloudy boundary layer during the autumnal freezing of the beaufort sea. *JOURNAL OF GEOPHYSICAL RESEARCH-ALL SERIES-*, **102**, 13–851.

Curry, J., J. Schramm, M. Serreze, and E. Ebert, 1995: Water vapor feedback over the arctic ocean. *Journal of Geophysical Research: Atmospheres*, **100 (D7)**, 14 223–14 229.

Curry, J. A., 1986: Interactions among turbulence, radiation and microphysics in arctic stratus clouds. *Journal of the atmospheric sciences*, **43 (1)**, 90–106.

Curry, J. A., E. Ebert, and G. Herman, 1988: Mean and turbulence structure of the summertime arctic cloudy boundary layer. *Quarterly journal of the royal meteorological society*, **114 (481)**, 715–746.

Curry, J. A., and E. E. Ebert, 1992: Annual cycle of radiation fluxes over the arctic ocean: Sensitivity to cloud optical properties. *Journal of Climate*, **5 (11)**, 1267–1280.

Curry, J. A., and G. Herman, 1985b: Infrared radiative properties of summertime arctic stratus clouds. *Journal of climate and applied meteorology*, **24 (6)**, 525–538.

Curry, J. A., J. L. Schramm, W. B. Rossow, and D. Randall, 1996: Overview of arctic cloud and radiation characteristics. *Journal of Climate*, **9 (8)**, 1731–1764.

de Boer, G., E. W. Eloranta, and M. D. Shupe, 2009: Arctic mixed-phase stratiform cloud properties from multiple years of surface-based measurements at two high-latitude locations. *Journal of the Atmospheric Sciences*, **66 (9)**, 2874–2887.

Dee, D., and Coauthors, 2011: The era-interim reanalysis: Configuration and performance of the data assimilation system. *Quarterly Journal of the Royal Meteorological Society*, **137 (656)**, 553–597.

Doyle, S. H., and Coauthors, 2015: Amplified melt and flow of the greenland ice sheet driven by late-summer cyclonic rainfall. *Nature Geoscience*, **8 (8)**, 647–653.

Draxler, R. R., and G. Hess, 1998: An overview of the hysplit_4 modelling system for trajectories. *Australian meteorological magazine*, **47 (4)**, 295–308.

Epstein, H., and Coauthors, 2015: Tundra greenness [in arctic report card 2015]. National Oceanic and Atmospheric Administration.

Fettweis, X., E. Hanna, C. Lang, A. Belleflamme, M. Erpicum, and H. Gallée, 2013: Important role of the mid-tropospheric atmospheric circulation in the recent surface melt increase over the greenland ice sheet. *Cryosphere (The)*, **7**, 241–248.

Flynn, C. J., A. Mendoza, Y. Zheng, and S. Mathur, 2007: Novel polarization-sensitive micropulse lidar measurement technique. *Optics express*, **15 (6)**, 2785–2790.

Fossheim, M., R. Primicerio, E. Johannesen, R. Ingvaldsen, M. Aschan, and A. Dolgov, 2015: Climate change is pushing boreal fish northwards to the arctic: the case of the barents sea [in arctic report card 2015]. National Oceanic and Atmospheric Administration.

Frey, K., J. Comiso, L. Cooper, R. Gradinger, J. Grebmeier, and J. Tremblay, 2015: Arctic ocean primary productivity [in arctic report card 2015]. National Oceanic and Atmospheric Administration.

Fridlind, A. M., B. Van Diedenhoven, A. S. Ackerman, A. Avramov, A. Mrowiec, H. Morrison, P. Zuidema, and M. D. Shupe, 2012: A fire-ace/sheba case study of mixed-phase arctic boundary layer clouds: Entrainment rate limitations on rapid primary ice nucleation processes. *Journal of the Atmospheric Sciences*, **69 (1)**, 365–389.

Gaussiat, N., R. J. Hogan, and A. J. Illingworth, 2007: Accurate liquid water path retrieval from low-cost microwave radiometers using additional information from a lidar ceilometer and operational forecast models. *Journal of Atmospheric and Oceanic Technology*, **24 (9)**, 1562–1575.

Graversen, R. G., and M. Wang, 2009: Polar amplification in a coupled climate model with locked albedo. *Climate Dynamics*, **33 (5)**, 629–643.

Hall, A., 2004: The role of surface albedo feedback in climate. *Journal of Climate*, **17 (7)**, 1550–1568.

Han, Y., and E. R. Westwater, 2000: Analysis and improvement of tipping calibration for ground-based microwave radiometers. *IEEE Transactions on Geoscience and Remote Sensing*, **38 (3)**, 1260–1276.

Hanna, E., T. E. Cropper, P. D. Jones, A. A. Scaife, and R. Allan, 2015: Recent seasonal asymmetric changes in the nao (a marked summer decline and increased winter variability) and associated changes in the ao and greenland blocking index. *International Journal of Climatology*, **35 (9)**, 2540–2554.

Hanna, E., J. M. Jones, J. Cappelen, S. H. Mernild, L. Wood, K. Steffen, and P. Huybrechts, 2013: The influence of north atlantic atmospheric and oceanic forcing effects on 1900–2010 greenland summer climate and ice melt/runoff. *International Journal of Climatology*, **33 (4)**, 862–880.

Hayman, M., and J. P. Thayer, 2009: Explicit description of polarization coupling in lidar applications. *Optics letters*, **34 (5)**, 611–613.

Helm, V., A. Humbert, and H. Miller, 2014: Elevation and elevation change of greenland and antarctica derived from cryosat-2. *The Cryosphere*, **8 (4)**, 1539–1559, doi:10.5194/tc-8-1539-2014, URL http://www.the-cryosphere.net/8/1539/2014/.

Hurrell, J. W., Y. Kushnir, and M. Visbeck, 2001: The north atlantic oscillation. *Science*, **291 (5504)**, 603–605.

Intrieri, J. M., and M. D. Shupe, 2004: Characteristics and radiative effects of diamond dust over the western arctic ocean region. *Journal of climate*, **17 (15)**, 2953–2960.

Jacob, T., J. Wahr, W. T. Pfeffer, and S. Swenson, 2012: Recent contributions of glaciers and ice caps to sea level rise. *Nature*, **482 (7386)**, 514–518.

Jeffries, M., J. Richter-Menge, and J. Overland, 2015: Arctic report card 2015. National Oceanic and Atmospheric Administration.

Jiang, H., W. R. Cotton, J. O. Pinto, J. A. Curry, and M. J. Weissbluth, 2000: Cloud resolving simulations of mixed-phase arctic stratus observed during base: Sensitivity to concentration of ice crystals and large-scale heat and moisture advection. *Journal of the atmospheric sciences*, **57 (13)**, 2105–2117.

Jung, T., M. A. Kasper, T. Semmler, and S. Serrar, 2014: Arctic influence on subseasonal midlatitude prediction. *Geophysical Research Letters*, **41 (10)**, 3676–3680.

Kalnay, E., and Coauthors, 1996: The ncep/ncar 40-year reanalysis project. *Bulletin of the American meteorological Society*, **77 (3)**, 437–471.

Kanamitsu, M., 1989: Description of the nmc global data assimilation and forecast system. *Weather and Forecasting*, **4 (3)**, 335–342.

Klein, S. A., and Coauthors, 2009: Intercomparison of model simulations of mixed-phase clouds observed during the arm mixed-phase arctic cloud experiment. i: Single-layer cloud. *Quarterly Journal of the Royal Meteorological Society*, **135 (641)**, 979–1002.

Korolev, A., 2007: Limitations of the wegener-bergeron-findeisen mechanism in the evolution of mixed-phase clouds. *Journal of the Atmospheric Sciences*, **64 (9)**, 3372–3375.

Kovacs, K., P. Lemons, J. MacCracken, and C. Lydersen, 2015: Walruses in a time of climate change [in arctic report card 2015]. National Oceanic and Atmospheric Administration.

Manabe, S., and R. J. Stouffer, 1980: Sensitivity of a global climate model to an increase of co2 concentration in the atmosphere. *Journal of Geophysical Research: Oceans*, **85 (C10)**, 5529–5554.

Manabe, S., and R. T. Wetherald, 1975: The effect of doubling the co 2 concentration on the climate of a general circulation model.

Markowski, P., and Y. Richardson, 2011: *Mesoscale meteorology in midlatitudes*, Vol. 2. John Wiley & Sons.

Maschwitz, G., U. Löhnert, S. Crewell, T. Rose, and D. Turner, 2013: Investigation of ground-based microwave radiometer calibration techniques at 530 hpa. *Atmospheric Measurement Techniques*, **6 (10)**, 2641–2658.

McLeod, J. T., and T. L. Mote, 2015: Assessing the role of precursor cyclones on the formation of extreme greenland blocking episodes and their impact on summer melting across the greenland ice sheet. *Journal of Geophysical Research: Atmospheres*, **120 (24)**, 12 357–12 377.

Miller, N., D. Turner, R. Bennartz, M. Shupe, M. Kulie, M. Cadeddu, and V. P. Walden, 2013: Surface-based inversions above central greenland. *Journal of Geophysical Research: Atmospheres*, **118 (2)**, 495–506.

Miller, N. B., M. D. Shupe, C. J. Cox, V. P. Walden, D. D. Turner, and K. Steffen, 2015: Cloud radiative forcing at summit, greenland. *Journal of Climate*, **28 (15)**, 6267–6280.

Morrison, H., G. de Boer, G. Feingold, J. Harrington, M. D. Shupe, and K. Sulia, 2012: Resilience of persistent arctic mixed-phase clouds. *Nature Geoscience*, **5 (1)**, 11–17.

Mosley-Thompson, E., C. Readinger, P. Craigmile, L. Thompson, and C. Calder, 2005: Regional sensitivity of greenland precipitation to nao variability. *Geophysical Research Letters*, **32 (24)**.

Mouginot, J., E. Rignot, B. Scheuchl, I. Fenty, A. Khazendar, M. Morlighem, A. Buzzi, and J. Paden, 2015: Fast retreat of zachariæ isstrøm, northeast greenland. *Science*, aac7111.

Neff, W., G. P. Compo, F. Martin Ralph, and M. D. Shupe, 2014: Continental heat anomalies and the extreme melting of the greenland ice surface in 2012 and 1889. *Journal of Geophysical Research: Atmospheres*, **119 (11)**, 6520–6536.

Ohmura, A., and N. Reeh, 1991: New precipitation and accumulation maps for greenland. *Journal of Glaciology*, **37 (125)**, 140–148.

Pal, S., 2014: Monitoring depth of shallow atmospheric boundary layer to complement lidar measurements affected by partial overlap. *Remote Sensing*, **6 (9)**, 8468–8493.

Pinto, J. O., 1998: Autumnal mixed-phase cloudy boundary layers in the arctic. *Journal of the atmospheric sciences*, **55 (11)**, 2016–2038.

Pithan, F., and T. Mauritsen, 2014: Arctic amplification dominated by temperature feedbacks in contemporary climate models. *Nature Geoscience*, **7 (3)**, 181–184.

Pithan, F., B. Medeiros, and T. Mauritsen, 2014: Mixed-phase clouds cause climate model biases in arctic wintertime temperature inversions. *Climate dynamics*, **43 (1-2)**, 289–303.

Qiu, S., X. Dong, B. Xi, and J.-L. Li, 2015: Characterizing arctic mixed-phase cloud structure and its relationship with humidity and temperature inversion using arm nsa observations. *Journal of Geophysical Research: Atmospheres*, **120 (15)**, 7737–7746.

Robock, A., 1983: Ice and snow feedbacks and the latitudinal and seasonal distribution of climate sensitivity. *Journal of the Atmospheric Sciences*, **40 (4)**, 986–997.

Rogers, J. C., and H. Van Loon, 1979: The seesaw in winter temperatures between greenland and northern europe. part ii: Some oceanic and atmospheric effects in middle and high latitudes. *Monthly Weather Review*, **107 (5)**, 509–519.

Rose, T., S. Crewell, U. Löhnert, and C. Simmer, 2005: A network suitable microwave radiometer for operational monitoring of the cloudy atmosphere. *Atmospheric Research*, **75 (3)**, 183–200.

Sassen, K., 1991: The polarization lidar technique for cloud research: A review and current assessment. *Bulletin of the American Meteorological Society*, **72 (12)**, 1848–1866.

Schuenemann, K. C., and J. J. Cassano, 2009: Changes in synoptic weather patterns and greenland precipitation in the 20th and 21st centuries: 1. evaluation of late 20th century simulations from ipcc models. *Journal of Geophysical Research: Atmospheres*, **114 (D20)**.

Schuenemann, K. C., and J. J. Cassano, 2010: Changes in synoptic weather patterns and greenland precipitation in the 20th and 21st centuries: 2. analysis of 21st century atmospheric changes using self-organizing maps. *Journal of Geophysical Research: Atmospheres*, **115 (D5)**.

Schuenemann, K. C., J. J. Cassano, and J. Finnis, 2009: Synoptic forcing of precipitation over greenland: Climatology for 1961-99. *Journal of Hydrometeorology*, **10 (1)**, 60–78.

Seo, K.-W., D. E. Waliser, C.-K. Lee, B. Tian, T. Scambos, B.-M. Kim, J. H. van Angelen, and M. R. van den Broeke, 2015: Accelerated mass loss from greenland ice sheet: Links to atmospheric circulation in the north atlantic. *Global and Planetary Change*, **128**, 61–71.

Serreze, M. C., and R. G. Barry, 2011: Processes and impacts of arctic amplification: A research synthesis. *Global and Planetary Change*, **77 (1)**, 85–96.

Shepherd, A., and Coauthors, 2012: A reconciled estimate of ice-sheet mass balance. *Science*, **338 (6111)**, 1183–1189.

Sheppard, B., 2007: Sampling errors in the measurement of rainfall parameters using the precipitation occurrence sensor system (poss). *Journal of Atmospheric and Oceanic Technology*, **24 (2)**, 125–140.

Sheppard, B., and P. Joe, 2008: Performance of the precipitation occurrence sensor system as a precipitation gauge. *Journal of atmospheric and Oceanic technology*, **25 (2)**, 196–212.

Shuman, C. A., K. Steffen, J. E. Box, and C. R. Stearns, 2001: A dozen years of temperature observations at the summit: Central greenland automatic weather stations 1987-99. *Journal of Applied Meteorology*, **40 (4)**, 741–752.

Shupe, M. D., 2011: Clouds at arctic atmospheric observatories. part ii: Thermodynamic phase characteristics. *Journal of Applied Meteorology and Climatology*, **50 (3)**, 645–661.

Shupe, M. D., and J. M. Intrieri, 2004: Cloud radiative forcing of the arctic surface: The influence of cloud properties, surface albedo, and solar zenith angle. *Journal of Climate*, **17 (3)**, 616–628.

Shupe, M. D., P. Kollias, P. O. G. Persson, and G. M. McFarquhar, 2008: Vertical motions in arctic mixed-phase stratiform clouds. *Journal of the Atmospheric Sciences*, **65 (4)**, 1304–1322.

Shupe, M. D., S. Y. Matrosov, and T. Uttal, 2006: Arctic mixed-phase cloud properties derived from surface-based sensors at sheba. *Journal of the atmospheric sciences*, **63 (2)**, 697–711.

Shupe, M. D., D. D. Turner, A. Zwink, M. M. Thieman, E. J. Mlawer, and T. Shippert, 2015: Deriving arctic cloud microphysics at barrow, alaska: algorithms, results, and radiative closure. *Journal of Applied Meteorology and Climatology*, **54 (7)**, 1675–1689.

Shupe, M. D., and Coauthors, 2013: High and dry: New observations of tropospheric and cloud properties above the greenland ice sheet. *Bulletin of the American Meteorological Society*, **94 (2)**, 169–186.

Solomon, A., M. Shupe, P. Persson, and H. Morrison, 2011: Moisture and dynamical interactions maintaining decoupled arctic mixed-phase stratocumulus in the presence of a humidity inversion. *Atmospheric Chemistry and Physics*, **11 (19)**, 10 127–10 148.

Solomon, A., M. D. Shupe, O. Persson, H. Morrison, T. Yamaguchi, P. M. Caldwell, and G. de Boer, 2014: The sensitivity of springtime arctic mixed-phase stratocumulus clouds to surface-layer and cloud-top inversion-layer moisture sources. *Journal of the Atmospheric Sciences*, **71 (2)**, 574–595.

Steffen, K., and J. Box, 2001: Surface climatology of the greenland ice sheet: Greenland climate network 1995–1999. *Journal of Geophysical Research: Atmospheres*, **106 (D24)**, 33 951–33 964.

Stein, A., R. Draxler, G. Rolph, B. Stunder, M. Cohen, and F. Ngan, 2015: Noaa's hysplit atmospheric transport and dispersion modeling system. *Bulletin of the American Meteorological Society*, **96 (12)**, 2059–2077.

Stephens, G. L., 1994: *Remote sensing of the lower atmosphere*, Vol. 1994. Oxford University Press New York.

Stramler, K., A. D. Del Genio, and W. B. Rossow, 2011: Synoptically driven arctic winter states. *Journal of Climate*, **24 (6)**, 1747–1762.

Tedesco, M., X. Fettweis, T. Mote, J. Wahr, P. Alexander, J. Box, and B. Wouters, 2013: Evidence and analysis of 2012 greenland records from spaceborne observations, a regional climate model and reanalysis data. *Cryosphere (The)*, **7**, 615–630.

Tjernström, M., and Coauthors, 2012: Meteorological conditions in the central arctic summer during the arctic summer cloud ocean study (ascos). *Atmospheric Chemistry and Physics*, **12 (15)**, 6863–6889.

Turner, D., S. Kneifel, and M. Cadeddu, 2016: An improved liquid water absorption model at microwave frequencies for supercooled liquid water clouds. *Journal of Atmospheric and Oceanic Technology*, **33 (1)**, 33–44.

Turner, D. D., S. A. Clough, J. C. Liljegren, E. E. Clothiaux, K. E. Cady-Pereira, and K. L. Gaustad, 2007: Retrieving liquid wat0er path and precipitable water vapor from the atmospheric radiation measurement (arm) microwave radiometers. *Geoscience and Remote Sensing, IEEE Transactions on*, **45 (11)**, 3680–3690.

Van Tricht, K., and Coauthors, 2016: Clouds enhance greenland ice sheet meltwater runoff. *Nature communications*, **7**.

Verlinde, J., J. Y. Harrington, G. McFarquhar, V. Yannuzzi, and Coauthors, 2007: The mixed-phase arctic cloud experiment. *Bulletin of the American Meteorological Society*, **88 (2)**, 205.

Vizcaino, M., U. Mikolajewicz, F. Ziemen, C. B. Rodehacke, R. Greve, and M. R. Broeke, 2015: Coupled simulations of greenland ice sheet and climate change up to ad 2300. *Geophysical Research Letters*, **42 (10)**, 3927–3935.

Warren, S. G., C. J. Hahn, J. London, R. M. Chervin, and R. L. Jenne, 1988: Global distribution of total cloud cover and cloud type amounts over the ocean. Tech. rep., USDOE Office of Energy Research, Washington, DC (USA). Carbon Dioxide Research Div.; National Center for Atmospheric Research, Boulder, CO (USA).

Weitkamp, C., 2006: *Lidar: range-resolved optical remote sensing of the atmosphere*, Vol. 102. Springer Science & Business.

Westwater, E. R., Y. Han, M. D. Shupe, and S. Y. Matrosov, 2001: Analysis of integrated cloud liquid and precipitable water vapor retrievals from microwave radiometers during the surface heat budget of the arctic ocean project. *Journal of Geophysical Research: Atmospheres*, **106 (D23)**, 32 019–32 030.

Wexler, H., 1936: Cooling in the lower atmosphere and the structure of polar continental air. *Mon. Wea. Rev*, **64 (4)**, 122–136.

Wexler, H., 1937: Formation of polar anticyclones. *Monthly Weather Review*, **65 (6)**, 229–236.

Woods, C., R. Caballero, and G. Svensson, 2013: Large-scale circulation associated with moisture intrusions into the arctic during winter. *Geophysical Research Letters*, **40 (17)**, 4717–4721.

Xie, S., X. Liu, C. Zhao, and Y. Zhang, 2013: Sensitivity of cam5-simulated arctic clouds and radiation to ice nucleation parameterization. *Journal of Climate*, **26 (16)**, 5981–5999.

Appendix A

Polarization Correction Method for the MPL

There have been three separate MPL's in place at Summit over the ICECAPS period. As indicated in Section 3.1.3, the MPL's polarization measurements have been sub-standard (although the most recent instrument has been performing well thus far). The MPL's liquid crystal retarder (LCR) is the likely cause of this problem. The LCR switches between two states which determine the polarization of the outgoing laser beam. The MPL's receiver then only measures returns which have an orthogonal polarization to the outgoing pulse. The effect of the malfunction on the backscatter measured by the MPL is shown in the measured returns in both MPL channels as well as the mean δ_{linear} in clear sky regions between 2 and 3 km (Figures A.1 and A.2). δ_{linear} is expected to be constant at a few percent, due to the fact that backscatter observed by the MPL is due to molecular (i.e. Rayleigh) scattering in clear sky regions (Weitkamp, 2006). However, it is clear from Figure A.1 that this is not the case for much of the ICECAPS period. The LCR is not switching between its two states correctly which results in polarization cross talk between the two channels, therefore making the calculations of δ_{linear} inaccurate. δ_{linear} is variable over time with apparent periodicity due to the malfunction. The first two instruments that have been in operation at Summit have the same issue (although with different periodicity). Given the necessity of δ_{linear} for determination of cloud phase it is necessary to implement a correction algorithm in order for much of this data to be usable.

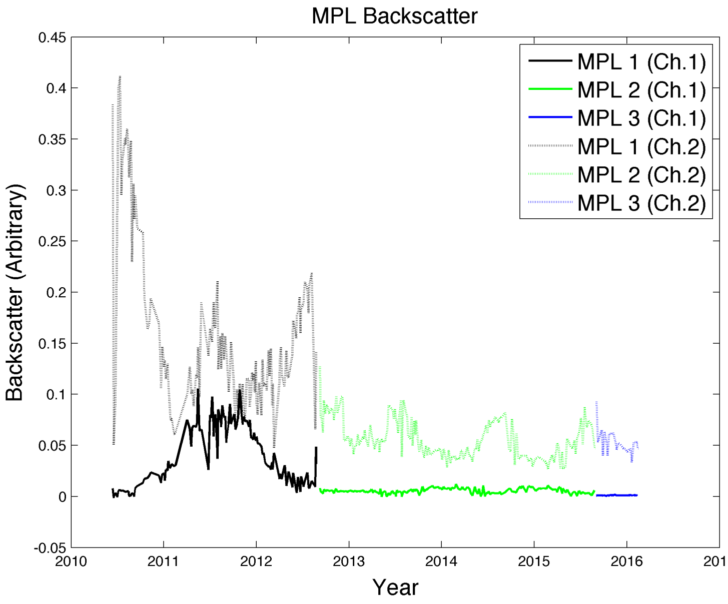

Figure A.1: Backscatter from Channels 1 (solid lines) and 2 (dotted lines) from the first (black), second (green), and third (blue) MPL in operation at Summit. All data are from clear sky cases between 2 and 3 km in altitude.

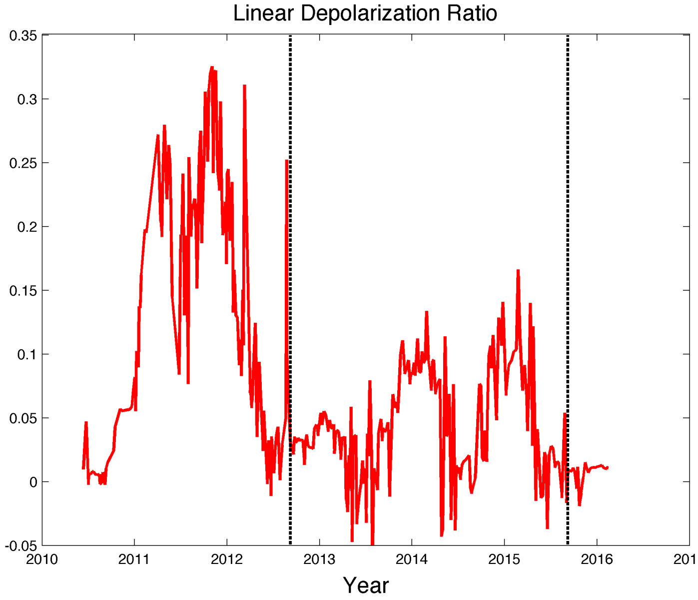

Figure A.2: δ_{linear} during clear sky periods at Summit. The black dashed lines indicate times when the MPL was replaced. Data is the same as from Figure A.1

The correction algorithm follows the methodology in Hayman and Thayer (2009). The process is designed to correct for a flawed assumption in polarization lidar, namely that the two orthogonal linearly polarized signals received by the lidar are completely independent.

$$d_m(z) = \frac{2P_\perp(0)}{P_\perp(0) + P_\parallel(0)} = \frac{2P_\perp(0)}{2P_\perp(0) + P_\perp(\frac{\pi}{2})} \tag{A.1}$$

$$\epsilon = \frac{1 - d_m(z)}{1 - d_a(z)} \tag{A.2}$$

A correction factor for the MPL's polarization measurements is calculated using Equations A.1 and A.2 (Hayman and Thayer, 2009) where the measured returns are used to calculate the measured depolarization, $d_m(z)$, which is in turn used to calculate the correction factor, ϵ. $d_a(z)$ is the expected value of depolarization. Data from clear sky periods from 2 to 3 km in altitude are averaged over approximately one hour and used to calculate $d_m(z)$ since the depolarization is theoretically known for clear skies; 0.02 is chosen for the expected value of depolarization, $d_a(z)$, in clear skies due to Rayleigh scattering (Weitkamp, 2006). The two to three kilometer altitude range is chosen for consistency (although the correction from Hayman and Thayer (2009) should be altitude independent) while the one hour temporal range is chosen to ensure enough data was averaged to remove potential noise from the calculation.

Once ϵ has been calculated for each clear sky case, a three point running mean of ϵ is computed in order to smooth out shorter term variability. Linear interpolation of ϵ in time is used to obtain the correction for each day in the dataset.

$$d(z) = 1 - \frac{1 - d_m(z)}{\epsilon} \tag{A.3}$$

$$\delta_{linear} = \frac{d}{2 - d} \tag{A.4}$$

Once the value of ϵ is known for each day, the corrected depolarization can be calculated using Equation A.3 and then used to obtain δ_{linear} using Equation A.4

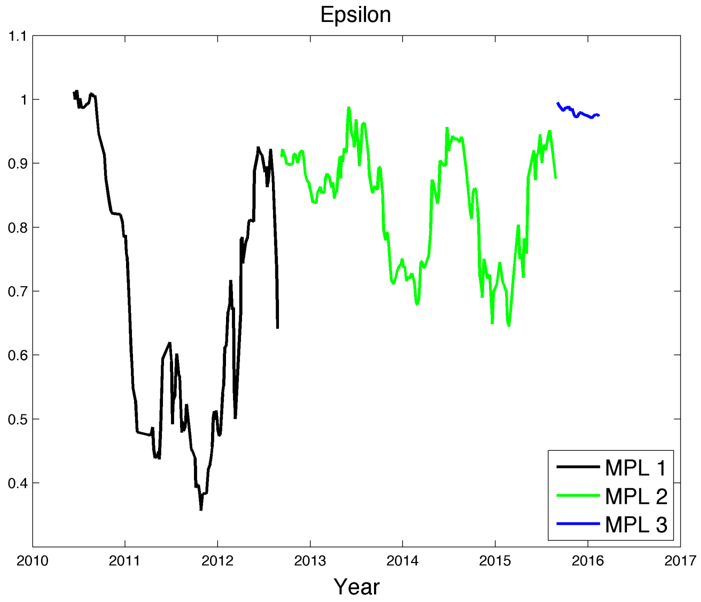

Figure A.3: ϵ for MPL's 1 (black), 2 (green), and 3 (blue)

(Flynn et al., 2007). Figure A.3 shows the value of ϵ for all three MPL's. There is periodicity in the MPL malfunction for the first two instruments. The first MPL experienced one long period of malfunction where ϵ changes from 1 to below 0.4 before rebounding to nearly 1 again (there could be another decrease in ϵ after this but it is not possible to determine due to the lack of data points since the MPL was soon replaced). The second MPL experienced the same general pattern but with a shorter period and smaller amplitude. There is a wave like change in ϵ with time, but also a superimposed linear decrease in system health. There are three troughs in the value of ϵ for the second MPL where the minimum values reach approximately 0.8, 0.7, and 0.6. Overall, the second MPL appeared to perform better than the first instrument, but also seemed to be getting progressively worse with time until it was also replaced. Thus far, the third MPL appears to be performing very well with no significant decrease in system health. The ICECAPS principal investigators believe that a buildup of static electricity, which was caused by winds in the very dry Summit environment, was the cause of the malfunctions in the LCR. They modified the third MPL to include better grounding of the instrument; we believe this has solved the problem and this seems to be confirmed by the constant value of epsilon with time for this instrument.

Figure A.4 shows three examples of MPL data both before and after the correction has been applied. On 28 September 2012 (Figure A.4 a-b), $\epsilon = 0.90$ and analysis of δ_{linear} and the cloud mask shows no discernible difference between the corrected and uncorrected data. It should be noted that the cloud mask seems to be performing as expected for the case before the correction has been applied. There is a clear layer of high backscatter and low δ_{linear} at cloud top as is expected for an Arctic liquid bearing cloud. This pattern, where the correction has essentially no impact on cloud phase classification, is consistently observed for times where $\epsilon >\sim 0.85$.

The second case (Figure A.4 c-d; 01 January 2014), is markedly different. The lidar backscatter indicates what appears to be the expected structure of a liquid layer sporadically during the first few hours and consistently for the remainder of the period. However, before the correction is applied δ_{linear} is much higher than expected for liquid. However, the correction reduces this to more expected values and the cloud mask then classifies these locations as liquid.

Similarly, the final case (Figure A.4 e-f; 17 November 2011) again has what appears to be a liquid layer during the second half of the day, but δ_{linear} is too high in the uncorrected data. Once the correction factor of $\epsilon = 0.42$ is applied this layer is identified as liquid by the cloud mask. However, the correction significantly decreases δ_{linear} everywhere leading to the identification of liquid in what is likely an ice cloud earlier in the period. In order to show the extent of the overcorrection, the temperature mask created from sounding data was also removed for this case. If included, there would be sharp cutoff between liquid and ice at approximately 4 km in the cloud occurring early in the period due to the -40°C isotherm. This

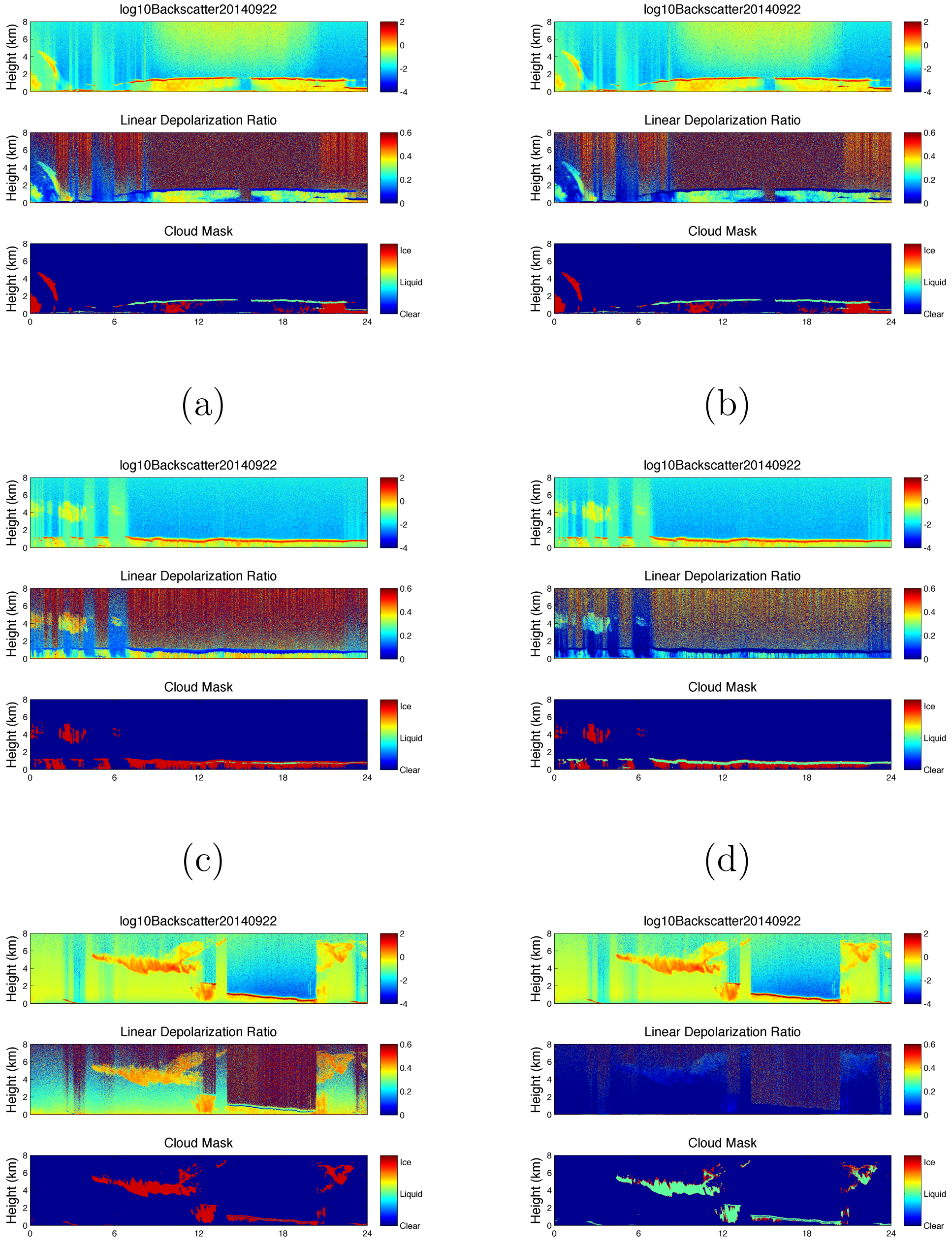

(a) (b)

(c) (d)

(e) (f)

Figure A.4: Comparison between uncorrected (left) and corrected (right) MPL data for three cases: 28 September 2012 (top; $\epsilon = 0.90$), 01 January 2014 (middle; $\epsilon = 0.72$), and 17 November 2011 (bottom; $\epsilon = 0.42$).

apparent overcorrection of the depolarization data is consistently observed when $\epsilon <\sim 0.50$.

In order to assess the validity of some of the assumptions in the calculation of ϵ, two tests were performed. First, the height of the calculation of ϵ was decreased from between 2 and 3 km to between 1 and 2 km. Second, the assumed value of clear sky depolarization ($d_a(z)$) was changed from 0.02 to 0.01. The mean of the difference between the 1-2 km and 2-3 km calculations is ϵ=0.02 with a standard deviation of 0.02. This is an order of magnitude lower than the actual value of ϵ so it's unlikely that changing the altitude would significantly change the results. The average difference between assuming clear sky depolarization of 0.01 instead of 0.02 is even lower (ϵ=0.01 with a standard deviation of .002), so again errors in this assumption should not have an impact of the results presented previously.

Analysis of the MPL dataset both before and after the Hayman and Thayer (2009) correction is applied, indicates that the application of the correction allows successful differentiation between ice and liquid when ϵ is between 0.5 and 0.85. Without the correction, only the portion of the dataset with $\epsilon > 0.85$ would be usable. Figure A.3 indicates that the implementation of the Hayman and Thayer (2009) correction has significantly increased the portion of the dataset which can be used for cloud phase detection.